[redacted]

UNCLASSIFIED

THE KAMAN AIRCRAFT CORPORATION

BLOOMFIELD, CONNECTICUT

000381

67:3

| SANDIA SYSTEMATIC DECLASSIFICATION REVIEW DOWNGRADING OR DECLASSIFICATION STAMP | |
|---|---|
| CLASSIFICATION CHANGED TO: U | AUTHORITY: W C Layne |
| Emilda Selph 12/08/97 PERSON CHANGING MARKING & DATE | RECORD ID: 98SN0830 |
| William Layne 12/15/97 PERSON VERIFYING MARKING & DATE | DATED: 11/21/97 |

Report No. R-177
7 March 1957

# FINAL REPORT OF THE SANDIA ROTOCHUTE PROGRAM - PHASE I

## AERODYNAMIC ANALYSIS

SC-DC-3295X

[redacted]

Prepared by
J. E. Fitzpatrick
H. H. McIntyre
C. V. Miale
D. C. Pasko

Checked by
R. E. Collins

Approved by
C. W. Ellis
D. W. Robinson
J. O. Emmerson

| | |
|---|---|
| 1st Review Date: 10/21/97 | Classification Retained |
| Authority: ADD | Classification Changed to: UNCL |
| Name: W C Layne | Contains No DOE Classified Information |
| 2nd Review Date: 11-21-97 | Contains UCNI |
| Authority: ADD | Contains UCAI |
| Name: W C Layne | Contains: |
| | OK FOR OPENNET |

UNCLASSIFIED

[redacted]

6-135-1

UNCLASSIFIED

# FOREWORD

An aerodynamic retarding device in which the rate of retardation can be controlled, is a necessity in many weapons systems applications. The governed rotochute is such a device. The retarding force which is generated by rotor blades in autorotation, is regulated by a blade pitch change mechanism called a governor. This report contains an analysis of all phases of governed rotochute operation and in particular in its application to the trajectory specifications furnished by the Sandia Corporation. The report is written in partial fulfillment of the Sandia Corporation Purchase Order No. 51-2120 to Kaman Aircraft Corporation of May 3, 1956

UNCLASSIFIED

TABLE OF CONTENTS

| | PAGE |
|---|---|
| FOREWORD | i |
| LIST OF ILLUSTRATIONS | iii |
| LIST OF SYMBOLS | vi |
| ABSTRACT | 1 |
| INTRODUCTION | 2 |
| PERFORMANCE ANALYSIS | 3 |
| A. LOW SPEED PERFORMANCE | 3 |
| B. HIGH SPEED PERFORMANCE | 14 |
| C. OPENING CYCLE ANALYSIS | 29 |
| D. ROTATIONAL SPEED GOVERNING | 46 |
| E. TRAJECTORY ANALYSIS | 61 |
| F. STABILITY ANALYSIS | 73 |
| G. EXPERIMENTAL PROGRAM | 101 |
| H. ROTOCHUTE DESIGN PROCEDURE | 107 |
| Appendix I Development of the Low Speed Performance Equations | 111 |
| Appendix II Opening Cycle Equations of Motion | 121 |
| Appendix III Feathering Equilibrium Equations | 124 |
| Appendix IV Rotor Rigidity Factor | 129 |
| List of References | 135 |

LIST OF ILLUSTRATIONS


| FIGURE NO. | TITLE | PAGE |
|---|---|---|
| A-1 | Glauert - Lock Empirical Curve | 137 |
| A-2 | Variation of Profile Drag Coefficient along the Blade. Equilibrium Autorotation | 138 |
| A-3 | Average Profile Drag Coefficients for Constant and Varied Inflow Comparison | 139 |
| A-4 | Average and Varied Inflow Performance Comparison | 140 |
| A-5 | Full-Scale Rotochute Through Flow Velocity Distribution | 141 |
| A-6 | Calculated Rotor Drag Coefficient Accounting for Stall, Idealized Prototype | 142 |
| A-7 | Comparison of Calculated and Experimental Rotor Drag Coefficients | 143 |
| A-8 | Variation of Torque Balanced Pitch Angle with Advance Ratio | 144 |
| B-2 | Kaman Rotochute Performance | 145 |
| B-3 | Kaman Rotochute Performance, Prototype Calculations | 146 |
| C-1 | Variation of Starting Torque with Dynamic Pressure | 147 |
| C-2 | Effect of Blade Twist and Bending on Starting Torque | 148 |
| C-3 | Rotor Speed at which Rotochute will start to Open at Various Values of $\beta_o$ and $\Lambda_o$ | 149 |
| C-4 | Rotor Speed and Time Required to Start Rotochute Opening at Various Values of $\beta_o$ and $\Lambda_o$ | 150 |
| C-5 | Variation of Starting Torque with Initial Values of Cone and Sweep Angles | 151 |
| C-6 | Rotochute Opening - Test Results, Rotational Speed | 152 |
| C-7 | Rotochute Opening - Test Results, Thrust | 153 |

## LIST OF ILLUSTRATIONS


| FIGURE NO. | TITLE | PAGE |
|---|---|---|
| C-8 | Rotorhute Opening-Test Results, Cone Angle | 154 |
| C-9 | Rotochute Opening-Calculated, Rotational Speed | 155 |
| C-10 | Rotochute Opening-Calculated, Cone Angle | 156 |
| D-1 | Schematic Diagram of Governor Linkage Geometry | 157 |
| D-2 | Calculated Centrifugal Feathering Moment | 158 |
| D-3 | Comparison of Calculated and Experimental Pitch Angle | 159 |
| D-4 | Comparison of Calculated and Experimental Coning Angle | 160 |
| D-5 | Comparison of Calculated and Experimental Aerodynamic Feathering Moment | 161 |
| E-1 | Prototype Rotochute Performance | 162 |
| E-2 | Rotor Tip Speed Variation With Velocity | 163 |
| E-3 | Limit Tip Speed and Terminal Velocity Variation With Rotor Drag Coefficient in Terminal Descent | 164 |
| E-4 | Rotochute Trajectory - Case I | 165 |
| E-5 | Rotochute Trajectory - Case II | 166 |
| E-6 | Rotochute Trajectory - Case III | 167 |
| E-7 | Rotochute Trajectory - Case IA | 168 |
| E-8 | Rotochute Trajectory - Case IB | 169 |
| E-9 | Variation of Rotochute Attitude Angle and Drop Distance from Release Altitude with Design Limit Tip Speed | 170 |
| E-10 | Prototype Rotochute Gross Weight Variation With Design Limit Tip Speed | 171 |
| F-1 | Example of Stability Results Determined by Electrical Analogy | 172 |

## LIST OF ILLUSTRATIONS


| FIGURE NO. | TITLE | PAGE |
|---|---|---|
| F-2 | Spiral Oscillation Damping | 173 |
| F-3 | Influence of Rotor Inertia on Spiral Oscillation Damping | 174 |
| F-4 | Influence of Specific Derivatives on Spiral Oscillation Damping | 175 |
| F-5 | Spiral Oscillation Period | 180 |
| F-6 | Influence of Rotor Speed on Rotor Rigidity Factor | 181 |
| G-1 | Schematic Diagram of Wind Tunnel Model Installation | 182 |

## LIST OF SYMBOLS

| | |
|---|---|
| $a$ | lift curve slope, per rad |
| $A$ | rotor disc area, $ft^2$ |
| $A_E$ | aspect ratio of exposed fins, $(\bar{B} - \bar{B})/ S_E$ |
| $A_R$ | blade area, $ft^2$ |
| $b$ | number of blades |
| $B$ | fraction of blade span over which lift integration is performed |
| $\bar{B}$ | effective fin span, ft |
| $c$ | blade chord, ft |
| $\bar{c}$ | mean aerodynamic chord of exposed fin, ft |
| $c_1$ | inboard chord in stepped planform, ft |
| $c_2$ | outboard chord in stepped planform, ft |
| $C_a$ | force coefficient |
| $C_c$ | blade section chordwise force coefficient |
| $C_d$ | blade section drag force coefficient |
| $C_{D_R}$ | rotor drag coefficient |
| $C_{d_o}$ | blade section profile drag coefficient |
| $C_f$ | blade section chordwise force, lb |
| $C_l$ | blade section lift force coefficient |
| $C_n$ | blade section normal force coefficient |
| $C_Q$ | rotor torque coefficient |
| $C_T$ | rotor thrust coefficient |
| $C_{l_\alpha}$ | $dC_l / d\alpha$ |
| $C_{d_\alpha}$ | $dC_d / d\alpha$ |

| | |
|---|---|
| $\bar{C}_{1,2,3,4}$ | aerodynamic unit span coefficients used in rotor derivatives |
| d | flapping hinge link when flapping hinge lies in plane of rotation, ft |
| D | blade drag force, lb |
| $\bar{D}$ | maximum body diameter, ft |
| e | blade flapping hinge offset, ft |
| f | feathering axis lead, ft |
| $f_{x,y}$ | forces acting at rotochute c.g. due to body and fins, lb |
| $F_{1,2}$ | forces acting on governor crank link, lb |
| $F_s$ | spring force, lb |
| $F_{x,y}$ | forces acting at rotochute c.g. due to rotor, lb |
| g | acceleration of gravity, ft/sec$^2$ |
| h | blade underslung from flapping axis, ft |
| H | distance from rotochute c.g. to blade flapping hinge, ft |
| i | $\sqrt{-1}$ |
| I | mass moment of inertia of rotochute, slug ft$^2$ |
| $I_b$ | mass moment of inertia of one rotor blade about its flapping hinge, slug ft$^2$ |
| $I_\theta$ | mass moment of inertia of one rotor blade about the spanwise axis, which is the projection of the feathering axis at zero coning angle, slug ft$^2$ |
| $I_\beta$ | mass moment of inertia of one rotor blade about the inboard chord line, slug ft$^2$ |
| $I_p$ | mass product of inertia of one rotor blade about the spanwise and chordwise axis, slug ft$^2$ |

| | |
|---|---|
| $I_x$ | $I_s - Mh^2$, slug ft$^2$ |
| $I_s$ | polar moment of inertia of rotor about rotation axis, slug ft$^2$ |
| $j$ | length of normal line from c.g. of blade to the feathering axis, ft |
| $k$ | rotor rigidity factor |
| $K$ | governor spring constant, lb/in |
| $K_1$ | longitudinal apparent mass coefficient of body |
| $K_2$ | transverse apparent mass coefficient of body |
| $K_3$ | ratio of induced body lift to lift of fins in presence of body |
| $l$ | effective body length, ft |
| $l_s$ | governor spring deflection under load, in |
| $L$ | blade lift force, lb |
| $L_B$ | body lift force, lb |
| $L_f$ | free length of spring, in |
| $L_w$ | lift of fins in presence of rotochute body, lb |
| $\Delta L_1$ | spring deflection due to centrifugal forces, in |
| $\Delta L_2$ | spring deflection due to preload collar position, in |
| $m$ | length of governor crank spring collar arm, in |
| $m_R$ | total mass of rotochute, slugs |
| $m_{x,y}$ | moment about rotochute c.g. due to body and fin forces, ft-lb |
| $M$ | Mach number |
| $M_B$ | moment about rotochute c.g. due to body forces, ft-lb |
| $M_f$ | blade aerodynamic flapping moment, ft-lb |
| $M_o$ | Mach number of rotochute flight |

| | |
|---|---|
| $M_v$ | moment of body volume about its bow |
| $M_W$ | moment about rotochute c.g. due to fin forces, ft-lb |
| $M_{C_B}$ | centrifugal bending moment about flapping hinge, ft-lb |
| $M_{C_T}$ | centrifugal feathering moment about feathering axis, ft-lb |
| $M_{spr}$ | spring feathering moment, ft-lb |
| $M_{\gamma\gamma}$ | moment about rotochute c.g. due to rotor forces, ft-lb |
| n | length of governor-collar link, in |
| N | rotor speed, rev/min |
| $N_r$ | blade section normal force, lb |
| p | complex roots of characteristic equation |
| P | mass of rotor blade outboard of flapping hinge, slugs |
| q | dynamic pressure, psf |
| Q | torque, ft-lb |
| Q' | blade net quasi-steady force tangent to rotation path and normal to span axis, lb |
| $r_o$ | radius from center of rotation to any span station, ft |
| r | radius to any span station at $\beta = 0$, ft |
| $r_1$ | span length from inboard end to step in stepped planform, ft |
| R | radius of rotor disc at zero cone angle, ft |
| $R_g$ | gas constant, lb-ft/slug deg |
| $R_N$ | Reynolds number |
| R' | radius to representative station, ft |
| R | length of blade, ft |
| s | distance of governor-collar link-pin from governor-crank pin, measured in a plane perpendicular to the plane of rotation, ft |

| | |
|---|---|
| $S$ | cross-sectional area of body at any station s from bow, $ft^2$ |
| $S_B$ | effective cross-sectional area of the base of the body, $ft^2$ |
| $S_c$ | blade chordwise center of gravity mass moment, slug ft |
| $S_f$ | exposed fin area, $ft^2$ |
| $S_s$ | blade spanwise center of gravity mass moment, slug ft |
| $S_T$ | scale factor |
| $t$ | time, sec |
| $T$ | rotochute quasi-steady thrust, lb |
| $T_a$ | air temperature, deg F |
| $U$ | velocity through rotor disc, ft/sec |
| $U_F$ | velocity normal to blade station, ft/sec |
| $U_T$ | velocity due to rotor speed, ft/sec |
| $v$ | induced air speed at rotor disc, ft/sec |
| $V$ | resultant velocity acting over blade section, ft/sec |
| $V_v$ | rotochute forward flight velocity, ft/sec |
| $w$ | governor-crank flapping-hinge arm, ft |
| $W$ | gross weight of rotochute, lb |
| $W_B$ | blade weight, lb |
| $x, y, z,$ $x_1, y_1, z_1$ | coordinate systems |
| $x_I$ | blade chord distance from leading edge in percent of total radius |
| $x_F$ | length of line from blade section center of pressure normal to the projection of the feathering axis on the blade, fraction of radius |

| | |
|---|---|
| $x_I$ | blade span distance from inboard end as fraction of total radius |
| $x_H$ | distance to rotochute c.g. from bow, ft |
| $x_p$ | distance to fin center of pressure from bow, ft |
| $\alpha$ | generalized angle of attack, deg |
| $\alpha_r$ | blade section angle of attack, deg |
| $\alpha_g$ | minimum value of $\gamma$, deg |
| $\alpha_R$ | blade root angle of attack, deg |
| $\alpha_t$ | blade tip angle of attack, deg |
| $\beta$ | blade flapping angle from plane of rotation, deg |
| $\beta_0$ | initial blade cone angle from vertical, deg |
| $\gamma$ | governor-crank arm angle, deg |
| $\gamma_0$ | ratio of spiral oscillation damping to critical damping |
| $\bar{\gamma}$ | modified Lock number |
| $\delta$ | angle in the plane of rotation through which the flapping hinge link moves from the plane perpendicular to the plane of rotation and parallel to the reference axis, deg |
| $\Delta$ | maximum value of $\delta$, deg |
| $\epsilon$ | maximum value of $\gamma$, deg |
| $\eta$ | H/R |
| $\eta_M$ | minimum angle of governor-crank collar-link arm, deg |
| $\theta$ | blade pitch angle, deg |
| $\theta_h$ | angle between flapping hinge link and plane of rotation, deg |
| $\theta_0$ | initial blade pitch angle, deg |
| $\lambda$ | net inflow ratio, $\lambda_d - \lambda_i$ |
| $\lambda_d$ | advance velocity ratio, $\frac{V_v}{\Omega R}$ |

| | |
|---|---|
| $\lambda_i$ | induced inflow velocity ratio, $\frac{v}{\Omega R}$ |
| $\Lambda$ | blade sweep angle, deg |
| $\Lambda_o$ | initial blade sweep angle, deg |
| $\mu$ | angle between flapping hinge link at negative stop and flapping hinge link in plane parallel to reference axes measured in plane of rotation, deg |
| $\bar{\mu}$ | mass of blade per unit length, slugs/ft |
| $\nu$ | kinematic viscosity, sec/ft$^2$ |
| $\Xi$ | ratio of prototype tip speed to model tip speed |
| $\xi$ | e/R |
| $\rho$ | mass density of air, slug/ft$^2$ |
| $\sigma$ | solidity ratio, be/$\pi$ R |
| $\tau$ | angle between a tangent to the flight path and the horizontal, deg |
| $\phi$ | inflow angle of attack, $\tan^{-1} U_T/U_P$ , deg |
| $\psi$ | azimuth position of blade, $\Omega t$, deg |
| $\omega$ | rotor flute oscillation frequency, rad/sec |
| $\Omega$ | rotor angular speed, rad/sec |

Subscript x indicates force in x-direction, moment about x-axis, or rotation about x-axis.

Subscript y indicates force in y-direction, moment about y-axis, or rotation about y-axis.

Dots over displacement indicate differentiation with respect to time.

In general $(F_x)_{\dot{x}} = \dfrac{\partial F_x}{\partial \dot{x}}$ etc.

A bar over a derivative indicates the combined rotor and body derivative.

A B S T R A C T

A governed rotochute utilizes the aerodynamic autorotation of a set of rotor blades to generate a force opposite to the direction of motion of an airborne vehicle. The retarding force is regulated by a blade pitch change mechanism called a governor. The operation of the governed rotochute throughout the flight range from release to touchdown is described herein. The manner in which a governed rotochute is designed for a specific subsonic mission is also outlined. Finally the effect of the rotochute on the stability of the airborne vehicle at terminal descent velocity is determined.

## INTRODUCTION

Controlled aerodynamic retardation of many airborne vehicles is required for their maximum effectiveness. One device for providing the required retardation is the "Rotochute". It is a multibladed aerodynamic device which utilizes the principles of autorotation to sustain a rotational motion of the blades. An aerodynamic thrust force is then developed opposite to the direction of vehicular motion as a result of the blade rotation. Autorotation is a result of an equilibrium between an accelerating torque due to blade lift and a decelerating torque due to blade drag. The blade lift and drag and consequently the thrust force depend on the inflow and pitch angles. In the Kaman rotochute the blade pitch angle is controlled by means of a spring governor. The rotor thrust cannot be raised indefinitely, however, but is limited by the aerodynamic characteristics of the rotor blades. There is nevertheless an optimum pitch angle for any particular operating condition. The achievement of the maximum rotor thrust consistent with the aerodynamic characteristics of the blades, therefore, requires a continual adjustment of the blade pitch throughout the flight range. If the blade pitch were fixed, for instance, the rotor blades would be operating at their maximum attainable thrust coefficient at only one point in the trajectory and in order to attain a higher thrust coefficient, operation at excessive rotational speeds following deployment would be necessary. It is the purpose of this report therefore, to set forth the principles by which the optimum variation of blade pitch with velocity can be achieved for a specific rotochute mission, to show experimental verification for the methods developed based on these principles, and to examine the effect of the design parameters on the Rotochute stability.

## PERFORMANCE ANALYSIS

The performance of a rotochute is herein defined as the establishment of the variation of rotor thrust (or drag) coefficient with velocity-tip speed ratio throughout the trajectory from the point at which the maximum rotational speed is attained after deployment to terminal descent. This is an aerodynamic requirement and is a function of the aerodynamic characteristics of the blade under conditions of torque equilibrium. It is desireable, of course, to obtain this torque balance at the maximum possible rotor thrust coefficient throughout the trajectory.

It was found convenient to divide the performance analysis into two parts, namely high speed performance and low speed performance. Low speed performance considers that part of the operating range from the point at which a major portion of the blade becomes unstalled, to the minimum velocity-tip speed ratio. High speed performance considers that part of the operating range following the completion of the opening cycle after deployment to the point at which the average induced velocity is half the approach velocity. It is in this region (called the windmill brake state in helicopter notation) that the use of the momentum theory is valid in determining the induced velocity. The following is a detailed discussion of these regimes.

### A. LOW SPEED PERFORMANCE

The low speed performance analysis applies to the portion of the flight range near terminal descent where only the inboard portion of the rotor blades are stalled. In the usual helicopter notation this region of operation borders the windmill brake and the vortex ring states. The induced velocity in this regime is greater than or equal to half the descent velocity.

The coventional axial momentum theory no longer applies and therefore an empirical correction must be applied. This region has been investigated by Glauert (ref. 1) and Locke (ref. 2) and the experimental results presented in a manner which illustrates the smooth transition from one state to another. In deducing the empirical curve Glauert suggested the assumption that the through flow velocity ( $V - v$ ) is constant over the disc because of complications which were presented in analyzing the experimental results. However, the empirical curve can be applied to annular elements when the assumption is made that the blade elements are independent of radial position. Glauert introduced two new thrust coefficients based on different velocities. In one case, it is related to the approach velocity:

$$f = \frac{T}{2\pi R^2 \rho V_1^2}$$

In the other case, it is related to the through flow velocity:

$$F = \frac{T}{2\pi R^2 \rho (V_1 - v)^2}$$

A plot of the reciprocals of these coefficients is given in Figure A-1. This relation was used in calculating the performance of the model Rotochute on the assumption that the same relation between $\frac{1}{f}$ and $\frac{1}{F}$ exists when considering the elements of the disc as when considering the disc in its entirety. This would be exactly true if both $F$ and $f$ were independent of the radial station when the elements were assumed independent. In the regions where the momentum theory applies (the windmill brake state for instance) this relationship, letting $U = (V_1 - v)$, is;

$$T = 2\pi R^2 \rho U (U - V_1)$$

and

$$T = 2\pi R^2 \rho U^2 F$$

therefore

$$2\rho\pi R^2 U^2 F = 2\rho\pi R^2 U(U - V_i)$$

and

$$V_i = U(1-F)$$

since

$$F/f = \frac{V_i^2}{U^2} = (1-F)^2$$

$$f = \frac{F}{(1-F)^2}$$

This relation applies in the higher inflow region of the windmill brake state where a definite slipstream exists (Figure A-1).

A stripwise analysis had to be made for realistic results inasmuch as the method was applied to conditions where blade stall was encountered over part of the blade radius. In order to demonstrate the necessity for a strip analysis more graphically, some calculations were made of rotor drag coefficient assuming an average inflow velocity ratio. The average through flow velocity ratios were based on the simple blade element equation for an ideal rotor:

$$\lambda_{av} = -\frac{\theta}{3} + \sqrt{\frac{\theta^2}{9} + \frac{C_{d_{0av}}}{2a}} \qquad \text{(A-1)}$$

The average inflow velocity ratio depends heavily on an average profile drag coefficient. Using the previously calculated $C_{d_0}$ distributions which were based on strip analyses (Figure A-2), the average torque weighted profile drag coefficients were obtained as follows:

$$C_{d_{o_{av}}} = \frac{\int_0^1 C_{d_o} y_I^3 \, dy_I}{\int_0^1 y_I^3 \, dy_I} = 4\int_0^1 C_{d_o} y_I^3 \, dy_I$$

Using these values of $C_{d_o}$ (figure A-3), the rotor drag coefficient and the torque balanced pitch angles were calculated as a function of the advance ratio. A comparison between these values and those computed with distributed inflow shows little difference. It must be remembered however that the "right" $C_{d_{o\,av}}$ must have been used in the average inflow calculation to obtain a valid result, thus requiring a strip analysis in either case. Judging from the $C_{d_o}$ distributions (Figure A-2) a choice of the correct average $C_{d_o}$ would be strictly fortuitous. In addition, equation A-1 is good only when the correct average lift curve slope is known. Such an expression would be grossly in error when part of the blade was stalled. These deficiencies in the uniform inflow representation dictated the necessity for a strip analysis solution for accurate prediction of the maximum rotor drag coefficient.

Numerical Procedure

The procedure for determing the low speed performance at each advance ratio is divided into three parts: First, the determination of the distribution of the through flow velocity ratio, $\lambda$, secondly, the determination of the blade pitch angle required for torque balance, and thirdly, the determination of the thrust and/or rotor drag coefficient for the torque equilibrium pitch angle. The equations for the above three parts are developed in Appendix I. The equation for the through flow velocity ratio is:

$$\frac{\sigma}{8\lambda_u^2}\left[\left(y_I\cos\beta + e/R\right)^2 + \lambda_u^2\frac{f}{F}\cos^2\beta\right]^{1/2}\left(C_l + C_d\tan\phi\right) - f\cos\beta = 0 \qquad \text{(A-2)}$$

where

$$\tan\phi = \frac{\lambda_u\sqrt{\frac{f}{F}}\cos\beta}{y_I\cos\beta + e/R} \quad \text{and} \quad \lambda_u - \lambda_i = \lambda_u\sqrt{\frac{f}{F}} \qquad \text{(A-3)}$$

The lift and drag coefficients used in the solution of equation A-2 are obtained from airfoil data plotted as functions of angle of attack at the required Mach number and Reynolds number. The local angle of attack is:

$$\alpha_r = \theta + \tan^{-1}\left(\frac{\lambda_u\sqrt{\frac{f}{F}}\cos\beta}{y_I\cos\beta + e/R}\right) \qquad \text{(A-4)}$$

For the first approximation the $\cos\beta$ was considered to be unity. After the aerodynamic loading is obtained, the equilibrium flapping angle $\beta$ can be calculated and the process repeated. Because $\beta$ is normally small in this regime only one recycling is necessary.

One computational procedure will now be described. At each value of advance ratio an arbitrary value of $\theta$ and radial station is assumed and equation A-2 is solved by iterating on F. Similarly, it is solved for other radial stations until the radial through flow distribution is obtained for the assumed pitch angle. These values of $\lambda_u^2\frac{f}{F}$ are substituted into the torque equation and the value of the torque coefficient is then determined. The torque equation is derived in Appendix I and is as follows:

$$C_Q = \frac{\sigma}{2}\sum_0^1\left(C_d - C_l\tan\phi\right)\left[\left(y_I\cos\beta + e/R\right)^2 + \lambda_u^2\frac{f}{F}\cos^2\beta\right]^{1/2}\left(y_I\cos\beta + e/R\right)^2\Delta y_I \qquad \text{(A-5)}$$

where, the $C_l$ and $C_d$ are obtained from airfoil data as functions of the local angle of attack. The aforementioned calculations are repeated for various values of pitch angle until the one which yields zero torque at the particular value of advance ratio is determined. The thrust coefficient is then computed using the final through flow velocity distribution. The equation for the thrust coefficient as developed in Appendix I is:

$$C_T = \frac{\sigma}{2}\cos\phi\left\{\sum_{x_{i-1}}^{x_i} C_l\left(x\cos\beta + \frac{\sigma_x}{x}\right)\left[\left(x\cos\beta + \frac{\sigma_x}{x}\right)^2 + \lambda_d^2\frac{c}{r}\cos^2\beta\right]^{1/2}\Delta x_I + \sum_{0} C_d\sin\phi\left(x\cos\beta + \frac{\sigma_x}{x}\right)\left[\left(x\cos\beta + \frac{\sigma_x}{x}\right)^2 + \lambda_d^2\frac{c}{r}\cos^2\beta\right]^{1/2}\Delta x_I\right\} \quad (A\text{-}6)$$

and the rotor drag coefficient is obtained by the relationship:

$$C_{D_R} = 2C_T/\lambda_d^2$$

The equation for the equilibrium coning angle, $\beta$ is derived in Appendix I. Since the final through flow velocity distribution for torque equilibrium has been obtained, it can be substituted into the coning angle equation and the coning angle determined. Should the value of the coning angle significantly affect the value obtained for the rotor drag coefficient, it can be introduced into the equations and a more accurate value of $C_{D_R}$ obtained.

Calculations were made by the above mentioned procedure at a full scale Reynolds number for a rotochute with a solidity of 0.1075 and with NACA 0012 airfoil sections. The results are presented in Figures A-5 and A-6. The effect of partial blade stall is quite pronounced. The continued rise in the torque equilibrium pitch angle with advance ratio, $\lambda_d$ after the peak rotor drag coefficient has been reached is also evident.

Figure A-1 infers that ideal autorotation is obtained when the average through flow is zero. The results of this analysis (Figure A-5) definitely indicates that a positive average through flow velocity is obtained for equilibrium autorotation. The reason can be understood from a consideration of equation A-1. In order for the average through flow to be zero, the average profile drag coefficient must be zero. This would then yield a $C_{D_R}$ of 2. The lower the value of blade profile drag coefficient attained, therefore, the closer will the maximum rotor drag coefficient approach 2.0.

Effect of Mach Number, Reynolds Number and Surface Condition

The use of full scale Reynolds numbers and airfoil data for the smooth condition, resulted in the optimistic value of the maximum rotor drag coefficient shown in Figure A-6.

Inasmuch as complete airfoil data for the NACA 0012 was not available, the data used was a composite of information obtained from references 3 to 12. From this information charts of lift and drag coefficients were prepared for one tenth increments in Mach number for the relationship between Reynolds number and Mach Number corresponding to the condition under investigation. The ratio of Reynolds number to Mach number can be expressed as:

$$R_N/M = \frac{\rho V}{\mu/c}\frac{\sqrt{1.4 \rho p_0}}{\rho V} = \frac{\sqrt{1.4 \rho p_0}}{\mu/c}$$

which equals a constant times the chord for any particular condition. The Mach number is then related to rotor tip speed, advance ratio and radial station as follows:

$$M = \frac{V}{a} = \frac{V}{\sqrt{1.4 R_g T_t}} = \Omega R \sqrt{\frac{\bar{\mu}^2 + \bar{\lambda}^2}{1.4 R_g T_t}}$$

where $T_t = T_T / 1 + 2M^2$

Substituting the above value for temperature, the Mach number equation becomes:

$$M = \Omega R \sqrt{\frac{\lambda_i^2 + \mu_I^2}{1.4 R_g T_T - .2 (\Omega R)^2 [\lambda_i^2 + \mu_I^2]}}$$

For any particular tip speed, therefore, the Mach number and Reynolds number is obtained for any radial station and consequently the appropriate two dimensional data for these stations can be used.

Inasmuch as the model tests were conducted at lower section Reynolds numbers than were used in the calculation of Figure A-6, calculations were made using section data appropriate to these lower Reynolds numbers. A reduction in Reynolds number has the effect of reducing the maximum lift and increasing the section drag coefficient. As a result, the torque balance occurs at a lower blade pitch angle and the rotor thrust is reduced. In addition, the section profile drag coefficient is affected by surface condition and airfoil shape. Consequently, the blade pitch angle for torque balance is dependent upon these factors as well. For any particular advance ratio, a reduction in pitch increases the accelerating torque. A higher section drag therefore, requires a lower pitch angle for torque balance. On the model rotochute, the hub and blade grip section of the blade was very blunt and therefore contributed a high drag increment to that section. A reasonable estimate was made of the drag of this region. It was then incorporated, together with the low Reynolds number airfoil data, into the calculations. The results are presented and compared with wind tunnel results in Figures A-7 and A-8. At low advance ratios, changes

in the profile drag coefficient of even the inboard station significantly affects the pitch angle for torque balance and consequently the maximum rotor drag coefficient. At higher advance ratios this effect is not quite so pronounced since a larger portion of the blade is stalled and the effect of one station has a smaller influence. Reasonable correlation with the wind tunnel results was obtained therefore, when the effects of blade stall, appropriate Reynolds numbers and grip drag were accounted for. These results in turn indicate the improvement that may be obtained at full scale with grip drag reduced to a minimum.

Calculations for the maximum value of rotor drag coefficient for the prototype were made using reasonable estimates of blade surface conditions and the appropriate Reynolds numbers. A value of 1.53 was obtained. This value is less than that obtained for the idealized prototype (Fig. A-6) The difference is due to the increase in drag resulting from the modifications to the inboard section of the blade necessitated by the telescoping provision. The airfoil section was modified by increasing the trailing-edge radius. The minimum drag would be increased as a consequence. In addition, the drag of the internal type blade grip, although considerably less than that of the models, required a drag increment on that section of the blade. The value of blade pitch angle for torque equilibrium is shown on Figure A-8 for comparison with the model results.

Limitations of the Method

Theoretically the aforementioned method should be applicable throughout the rotochute operating range since in the high speed regime the relationship between the thrust coefficients F and f follows the momentum theory. As the advance ratio increases, however, the assumption that adjacent blade elements are independent becomes questionable because

of the spanwise pressure gradient and three dimensional flow considerations. For example, calculations were made at advance ratios of 0.25 and 0.5. At the advance ratio of 0.25, the calculated rotor drag coefficient was 31 percent below the experimental value and at an advance ratio of 0.5 it was 38% below the experimental value. The spanwise pressure gradient is produced by the rotation, and has the effect of sweeping the boundary layer outboard toward the tip. It thus postpones the stall at more inboard stations. According to reference 13, the maximum lift at the 80% radius station on a propeller was increased by approximately thirty percent as a result of this boundary layer thinning. In addition when blade stall proceeds toward the tip, a tip vortex sheet is produced which increases blade lift and drag. This phenomenon is described by Kuchemann in reference 14 as follows: "When a two dimensional airfoil is completely stalled a vortex sheet springs from the leading edge and another from the trailing edge. The vorticity vector on these sheets is directed along the span. On a finite span wing, these two vortex sheets must join together near the end. The vertical part of the vortex sheet may be called the 'tip vortex sheet'. It's existence signifies that the flow not only separates from the leading edge but also along the tip chord. The tip vortex sheet will exist above a certain incidence at which the flow is attached along the tip chord. The value of this angle of attack will depend on the load distribution, the tip shape and the Reynolds number". An additional induced drag increment is produced by the interaction of the vortices. Inasmuch as the thrust is proportional to $C_l + C_d \tan\phi$, the thrust would increase when both the $C_l$ and the $C_d$ of the tip section increase. No method was found for relating the strength of these vortex sheets to the tip angle of attack and load distribution, therefore, they could not be

accounted for in the two-dimensional strip analysis. The performance method could be used throughout the rotochute operating range, however, if a method could be devised that takes these two effects into account.

The limitations of this method at higher speeds do not prevent the calculation of performance in this range inasmuch as the method presented in the following section was developed to cover this region of operation.

## B. HIGH SPEED PERFORMANCE

In contrast to the difficulty encountered in calculating the low speed rotochute performance which requires the consideration of the induced velocity distribution and the variation of the normal force coefficient $C_n$ with blade angle of attack, some simplifications were possible in the prediction of the high speed rotochute performance. Since with increasing speed the induced velocity of the rotochute becomes proportionately less significant, it was apparent that during much of the high speed flight regime the induced effects could be neglected. In the high speed condition of flight, the rotor blades are completely stalled such that at the minimum value of the advance ratio considered ($\lambda_d = 0.4$) the tip angle of attack is approximately 20 degrees while at an advance ratio, $\lambda_d$ of 1.6 or nearly the maximum, it exceeds 50 degrees. However, it was realized that some provision should be made for considering the effect of the induced velocity at the lower advance ratios for which this method could be expected to apply. Therefore, the equations were developed permitting the inclusion of the induced velocity on an average basis as derived from momentum principles.

Within the limits of the blade angle of attack encountered under these conditions ($20^\circ < \alpha_r < 90^\circ$) the slope of the curve of normal force coefficient versus angle of attack is fairly shallow compared with the unstalled range. Hence, the spanwise variation of $C_n$ is necessarily smaller for the blade operating at the higher advance ratios. The assumption of an average or constant $C_n$ therefore, while not exact may be employed.

UNCLASSIFIED

A rapid estimation of an average normal force coefficient may be

made from the fact that the tangent of the inflow angle $\phi$, at any radial station is approximately equal to the advance ratio divided by the non-dimensional radial station. For the high speed performance range ($\lambda_d = 0.4 \rightarrow 2.0$), it can be shown that the blade pitch angle $\theta$, for torque equilibrium, is very close to zero. Consequently its effect on the blade section of attack can be neglected considering the large inflow angles associated with this regime. Therefore, to a close approximation, the section angle of attack at each of several span stations can be obtained from the advance angle whose tangent is equal to the ratio of the descent velocity to the rotational velocity at that station. This independency of angle of attack to blade pitch angle obviates the solution for torque equilibrium. With the blade angle of attack distribution determined, it is only necessary to select the appropriate airfoil section data for the angle of attack range defined and the normal force coefficient distribution can be readily obtained. A simple numerical integration of this distribution will yield a satisfactory average normal force coefficient for use in the solution of the performance equations. Slight changes in the angle of attack distribution due to the inclusion of the actual blade pitch angle for torque equilibrium will have a negligible effect on this average normal force coefficient.

The utilization of an average normal force coefficient led to a simple closed form integration of the elemental lift for the solution for the rotor drag coefficient.

The rotochute coning angle increases proportionally with advance ratio inasmuch as the blade aerodynamic flapping moment changes

with relation to the centrifugal flapping moment. The method of determining the thrust under these conditions requires first the solution for the equilibrium cone angle. Equilibrium in the flapping degree of freedom is obtained by equating the aerodynamic moment about the flapping hinge to the centrifugal moment about the same hinge.

The development of the equations for equilibrium coning angle is presented below for the case of a rotor system with an offset flapping hinge and with blade underslung.

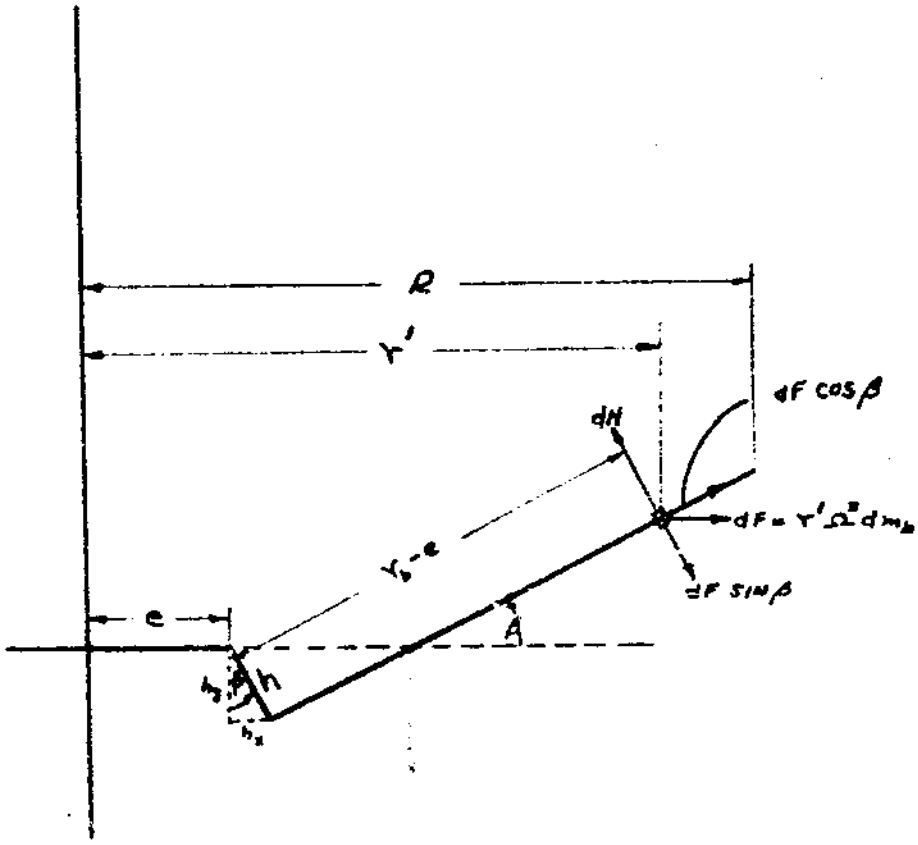


FIGURE B-1

UNCLASSIFIED

From the geometry of the system

$$h_x = h \sin\beta$$

thus $$r' = e + (r_b - e)\cos\beta + h \sin\beta \tag{B-1}$$

and the forces acting on the element become:

$$dF = C.F. = r'\Omega^2 dm_b \tag{B-2}$$

$$dF \sin\beta = \Omega^2 [e + (r_b - e)\cos\beta + h \sin\beta] \sin\beta \, dm_b \tag{B-3}$$

$$dF \cos\beta = \Omega^2 [e + (r_b - e)\cos\beta + h \sin\beta] \cos\beta \, dm_b \tag{B-4}$$

$$dN = C_N \rho/2 \, V^2 c \, dr \tag{B-5}$$

When the velocity component normal to the plane of rotation includes the induced velocity v, the normal and tangential components of the velocity are:

$$U_P = (V_v - v)\cos\beta \tag{B-6}$$

and

$$U_T = \Omega[e + (r_b - e)\cos\beta + h \sin\beta] \tag{B-7}$$

and the resultant velocity is

$$V^2 = U_P^2 + U_T^2$$

then

$$V^2 = V_v^2\cos^2\beta - 2V_v v\cos^2\beta + v^2\cos^2\beta + \Omega^2[e^2 + 2e(r_b - e)\cos\beta + 2eh\sin\beta + (r_b^2 - 2r_b e + e^2)\cos^2\beta + 2h\sin\beta(r_b - e)\cos\beta + h^2\sin^2\beta] \tag{B-8}$$

The sum of the moments about the offset flapping hinge can be

REVISED

UNCLASSIFIED

equated in integral form as:

$$\int_e^R (r_b - e)\, dN = \int_e^R (r_b - e)\, dF \sin\beta - \int_e^R h\, dF \cos\beta \tag{B-9}$$

where

$$\begin{aligned}\int_e^R (r_b - e)\, dN &= C_N \rho/2\, c \int_e^R (r_b - e)\, V^2 dr \\ &= C_N \rho/2\, c\, \Omega^2 \Big\{ \Big( [R-e]^2 \frac{(V_R - v)^2}{2\Omega^2} + \frac{1}{4}[R-e]^4 \Big) \cos^2\beta \\ &+ \Big\langle \frac{1}{3}[R-e]^3 (2e + 2h \sin\beta) \Big\rangle \cos\beta \\ &+ \frac{1}{2}[R-e]^2 (e^2 + 2eh \sin\beta + h^2 \sin^2\beta) \Big\}\end{aligned} \tag{B-10}$$

and

$$\begin{aligned}\int_e^R dF \sin\beta\, [r_b - e] &= \int_e^R (r_b - e)\, \Omega^2 [e + (r_b - e)\cos\beta + h \sin\beta] \sin\beta\, dm_b \\ &= \Omega^2 \sin\beta \int_e^R [e(r_b - e) + (r_b - e)^2 \cos\beta + (r_b - e) h \sin\beta]\, dm_b\end{aligned} \tag{B-11}$$

also

$$\begin{aligned}\int_e^R h\, dF \cos\beta &= \int_e^R h\, \Omega^2 [e + (r_b - e)\cos\beta + h \sin\beta] \cos\beta\, dm_b \\ &= \Omega^2 \cos\beta\, h \int_e^R [e + (r_b - e)\cos\beta + h \sin\beta]\, dm_b\end{aligned} \tag{B-12}$$

Substituting the following integral expression

$$\int_e^R (r_b - e)^2\, dm_b = I_s \tag{B-13}$$

$$\int_e^R (r_b - e)\, dm_b = S_s \tag{B-14}$$

$$\int_e^R dm_b = P \tag{B-15}$$

into the right hand side of the equilibrium expression yields the following flapping equilibrium equation:

$$\begin{aligned}&C_N \rho c \Omega^2 [R-e]^4 \Big\{ \Big[ \frac{1}{4}\Big(\frac{V_R - v}{\Omega R}\Big)^2 \Big(\frac{R}{R-e}\Big)^2 + \frac{1}{8} \Big] \cos^2\beta + \frac{(e + h\sin\beta)}{3(R-e)} \cos\beta \\ &+ \frac{(e^2 + 2eh \sin\beta + h^2 \sin^2\beta)}{4(R-e)^2} \Big\} = \sin\beta \Big\{ [e S_s + I_s \cos\beta + h S_s \sin\beta] \Big\} \\ &- h \cos\beta \Big\{ S_s \cos\beta + P(e + h \sin\beta) \Big\}\end{aligned} \tag{B-16}$$

REVISED

Dividing through the above equation by the quantity $h\,S_s \cos^2\beta$, letting $e/\cos\beta = e$ and neglecting the higher order terms, results in the following quadratic equation in terms of the $\tan\beta$:

$$\tan^2\beta + \frac{(e+I_x)}{h\,S_s}\tan\beta - 1 - \frac{eP}{S_s} - \frac{C_N \rho C [R-e]^4}{h\,S_s}\left\{\frac{1}{4}\left(\frac{V_v - v}{\Omega R}\right)^2\left(\frac{R}{R-e}\right)^2 + \frac{1}{8} + \frac{1}{3}\left(\frac{e}{R-e}\right)\right\} = 0 \qquad \text{(B-17)}$$

where the quantity, $I_x = I_s - Ph^2$

then

$$\tan\beta = -\frac{eS_s + I_x}{2hS_s} + \sqrt{\left(\frac{eS_s + I_x}{2hS_s}\right)^2 + 1 + \frac{eP}{S_s} + \frac{C_N \rho C [R-e]^4}{h\,S_s}\left\{\frac{1}{4}\left(\frac{V_v - v}{\Omega R}\right)^2\left(\frac{R}{R-e}\right)^2 + \frac{1}{8} + \frac{1}{3}\left(\frac{e}{R-e}\right)\right\}} \qquad \text{(B-18)}$$

The thrust expression is subsequently determined from Figure 1, where the element of thrust is the cosine component of the normal force.

$$dT = dN \cos\beta$$

and hence,

$$\text{Thrust} = \frac{b}{2\pi}\int_0^{2\pi}\left\{\int_e^R dT\right\} d\psi \qquad \text{(B-19)}$$

which is the general expression for the rotochute average thrust force as a function of asimuth. However, for the rotochute it can be assumed that the normal force is constant around the asimuth and thus the thrust expression will simplify to

$$T = b\int_e^R dT \qquad \text{(B-20)}$$

Since

$$dN = C_N \rho/2\, V^2 C\, dr_b$$

assuming a constant normal force coefficient gives

$$T = b\, C_N \rho/2\, c \int_e^R V^2 \cos\beta\, dr_b \qquad \text{(B-21)}$$

where as before

$$V^2 = V_v^2 \cos^2\beta - 2 V_v v \cos^2\beta + v^2 \cos^2\beta + \Omega^2 [e^2 + 2e(r_b - e)\cos\beta + 2eh \sin\beta + (r_b^2 - 2r_b e + e^2)\cos^2\beta + 2h \sin\beta (r_b - e)\cos\beta + h^2 \sin^2\beta]$$

Substituting for $V^2$ and performing the integration gives

$$T = b C_N \tfrac{1}{2} C \Omega^2 R^2 [R-e] \left\{ \left(\frac{V_v - v}{\Omega R}\right)^2 \cos^3\beta + \left(\frac{e}{R}\right)^2 \cos\beta + [R-e]\frac{e}{R^2}\cos^2\beta + \frac{2eh}{R^2}\sin\beta\cos\beta + \frac{[R-e]^2}{3R^2}\cos^3\beta \right\}$$

(B-22)

Having obtained the thrust expression, the rotochute drag coefficient may be evaluated from the relationship

$$C_{D_R} = \frac{T}{\tfrac{1}{2}\rho V_v^2 \pi R^2}$$

which gives

$$C_{D_R} = \sigma C_N \left(\frac{R-e}{R}\right)\left(\frac{\Omega R}{V_v}\right)^2 \left\{ \left[\left(\frac{V_v - v}{\Omega R}\right)^2 + \left(\frac{R-e}{R}\right)^2\right]\cos^3\beta + \left(\frac{R-e}{R}\right)\left(\frac{e}{R}\right)\cos^2\beta + \left(\frac{e}{R}\right)^2\cos\beta + 2\left(\frac{h}{R}\right)\left(\frac{e}{R}\right)\sin\beta\cos\beta \right\}$$

(B-23)

where $\sigma = be/\pi R$

A specific case of this general rotochute configuration was also investigated experimentally and therefore these performance equations were revised accordingly. This was the zero blade undersling configuration which leads to the most compact system in the stored condition. Thus for the case of h = 0, the equations for blade cone angle and rotor drag coefficient are respectively,

$$\tan\beta = \frac{\rho C_N C [R-e]}{e S_s + I_s}\left\{\frac{1}{4}\left(\frac{V_v - v}{\Omega R}\right)^2\left(\frac{R}{R-e}\right)^2 + \frac{1}{8} + \frac{1}{3}\left(\frac{e}{R-e}\right)\right\}$$

(B-24)

REVISED

and

$$C_{D_R} = \sigma C_w \left(\frac{\Omega R}{V_v}\right)^2 \left\{ \left\langle \left(\frac{V_v - v}{\Omega R}\right)^2 \left(1 - \frac{e}{R}\right) + \frac{1}{3}\left(1 - \frac{e^3}{R^3}\right) - \frac{e}{R}\left(1 - \frac{e^2}{R^2}\right) + \left(\frac{e}{R}\right)^2 \left(1 - \frac{e}{R}\right) \right\rangle \cos^2\beta + \frac{a}{R}\left(\frac{R-e}{R}\right)^2 \cos^2\beta + \left(\frac{e}{R}\right)^2 \left(1 - \frac{e}{R}\right) \cos\beta \right\}$$

(B-25)

The collection of terms outside the brackets in the coning expression is actually a modified similarity parameter

$$\left[ \frac{\rho C_w C [R-e]^4}{I + e S_s} \right]$$

equivalent to the more familar Lock's number used in rotary wing theory. The term herein designated as $\overline{\gamma}$ for convenience, becomes an important design parameter in that the effect of a variation in blade mass characteristics may be readily determined for a particular rotochute configuration.

Additional expressions were developed for consideration of the prototype rotochute system which for the case of telescoping blades results in a stepped blade planform. Since an average chord would not adequately represent the effective aerodynamic chord, the solution was made using a two part integration over inner and outer portions of the blade. This is simply a specific case of the general solution with zero underslung.

Again from Figure 1, allowing for h = 0 and a stepped chord with $C_1$ and $C_2$ referring to the inboard and outboard chords respectively, the equilibrium expression is:

$$\int_e^R dN (r_b - e) = \int_e^R dF (r_b - e) \sin\beta \qquad \text{(B-26)}$$

where

UNCLASSIFIED

$$\int_e^R (r_b - e)\, dF \sin\beta = \Omega^2 \sin\beta \left[ e S_s + I_s \cos\beta \right] \qquad \text{(B-27)}$$

REVISED

and

$$\int_e^R (r_b - e)\, dN = \tfrac{1}{2}\rho C_N C \int_e^R (r_b - e)\, V^2\, dr_b$$

$$= \tfrac{1}{2}\rho C_N \left\{ \int_e^{r_1} C_1 (r_b - e) V^2 dr_b + \int_{r_1}^R C_2 (r_b - e) V^2 dr_b \right\} \qquad \text{(B-28)}$$

where, upon substitution, integrating, and then following the procedure used in the previous development the equations for blade cone angle and rotor drag coefficient can be respectively expressed as,

$$\tan\beta = \frac{\rho C_N}{2[e\xi_1 + \xi_2]} \Bigg\langle C_1 \left\{ \tfrac{1}{2}(r_1 - e)^2 \left(\frac{V_v - v}{\Omega R}\right)^2 R^2 + \tfrac{1}{4}(r_1 - e)^4 + \tfrac{2}{3} e (r_1 - e)^3 + (r_1 - e)^2 \left(\frac{e^2}{2}\right) \right\}$$

$$+ C_2 \left\{ \left(\frac{R^2 - r_1^2}{2} - eR + er_1\right)\left(\frac{V_v - v}{\Omega R}\right)^2 R^2 + \frac{R^4 - r_1^4}{4} - \frac{R^3 e}{3} + \frac{r_1^3 e}{3} - \frac{R^3 e}{3} + \frac{2 r_1^3 e}{3} \right.$$

$$+ R^2 e^2 - r_1^2 e^2 + \frac{e^2 R^2}{2} - \frac{e^2 r_1^2}{2} - e^3 R + e^3 r_1 + \frac{2eR^3}{3} - \frac{2er_1^3}{3} - 2R^2 e^2 + 2r_1^2 e^2$$

$$\left. + 2Re^3 - 2r_1 e^3 + \frac{R^2 e^2}{2} - \frac{r_1^2 e^2}{2} - Re^3 + r_1 e^3 \right\} \Bigg\rangle \qquad \text{(B-29)}$$

$$C_{D_R} = \frac{C_N b}{\pi R^4}\left(\frac{\Omega R}{V_v}\right)^2 \Bigg\langle C_1 \left\{ \left[\left(\frac{V_v - v}{\Omega R}\right)^2 R^2 (r_1 - e) + \frac{r_1^3 - e^3}{3} - e(r_1^2 - e^2) + e^2 (r_1 - e)\right] \cos^3\beta \right.$$

$$\left. + e(r_1 - e)^2 \cos^2\beta + [(r_1 - e)e^2] \cos\beta \right\} + C_2 \left\{ \left[\left(\frac{V_v - v}{\Omega R}\right)^2 R^2 (R - r_1) + \frac{(R^3 - r_1^3)}{3} \right.\right.$$

$$\left.\left. - e(R^2 - r_1^2) + e^2 (R - r_1)\right] \cos^3\beta + e[R^2 - r_1^2 - 2eR + 2er_1] \cos^2\beta + [e^2 (R - r_1)] \cos\beta \right\} \Bigg\rangle \qquad \text{(B-30)}$$

As previously mentioned the induced velocity $v_i$ was incorporated in the performance expressions in order to extend further their applicability into the low advance ratio regime. From reference 15, based on momentum theory in the windmill brake state, a simple expression may be derived that permits an iterative evaluation of the average induced velocity. This relationship is applicable to the point where the drag coefficient equals unity.

From the above reference the induced velocity ratio becomes:

$$v/V_v = 1/2\left[1-\sqrt{1-C_{D_R}}\right]$$

when corrected for the sign convention used herein, that is, that the induced velocity is positive when it is opposite in sense to the rotochute inflow velocity.

Comparison with Wind Tunnel Results

Numerical solutions of the foregoing equations were made for the various rotochute parameters investigated in the wind tunnel program. For ease of solution the inflow velocity was at first neglected in the calculation of rotochute drag coefficient. Subsequent calculations were made including the induced velocity on an average basis as determined from the initial uncorrected rotor drag coefficient. The results of these solutions for various rotor solidities are compared with the experimental findings in Figure B-2. The importance of the induced velocity correction can be seen at an advance ratio of 0.4 where the corrected analytical results are shown to conform with the experimental datum. At a solidity of .318 an induced velocity correction would also have to be applied at advance ratios greater than 0.4 since the rotochute drag coefficient at these advance ratios is still large. When the corrected rotochute drag coefficient values are less than unity, successive iterations are possible and it becomes a simple matter to analytically predict the slope of the retardation curve. This is noted for the corrected values presented in Figure B-2 for the two advance ratios, $\lambda_d = .5$ & $\sigma = .318$ and $\lambda_d = .4$ & $\sigma = .215$, where the calculated points closely approximate the experimental findings. The uncorrected drag coefficient value of 1.09 at $\lambda_d = .4$ for the rotochute solidity of

.215 was corrected to a value of $C_{D_R}$ = .85 by consideration of the induced velocity. This clearly illustrates the cusp-like rapid divergence from the experimental curve that would otherwise occur from neglect of the induced velocity. The lower solidity uncorrected drag coefficient calculations presented in Figure B-2 exhibit a more subdued cusp-like divergence than those at the higher solidities because the rotor drag coefficients are smaller. Since the $C_{D_R}$ values at this solidity are small (less than unity) the induced velocity corrections may be applied further into the lower advance ratio regime. The retardation coefficients therefore, may be predicted with good accuracy for all $C_{D_R}$ values that are corrected for induced velocity.

The rotor drag coefficients calculated using the average normal force coefficient value of 1.6 compares favorably with the experimental findings (Figure B-2). At the lower solidity a slightly larger average $C_n$ value would be required. In order to obtain a complete performance picture it then became desirous to ascertain the effect of $C_n$ variations. Therefore, calculations of the rotor drag coefficient were made with a view towards bracketing the results previously calculated for a value of 1.6. The results are presented in Figure B-2. Upon examination it is observed that at the lower solidity investigated, $\sigma$ = .106 it was found that a 12.5 percentage change in $C_n$ produced a negligible change in the value of $C_{D_R}$. Thus the sensitivity of the results to our exact average $C_n$ is small and for a first approximation an average constant value of $C_n$ = 1.6 was found to give acceptable agreement. It is concluded then from observation of the curves and the

retardation expression that of the three principle parameters of the $C_{D_R}$ equation namely $\sigma$, $\cos^3\beta$ and $C_n$, that reasonable variations in the latter parameter least affects the results. It may be said then that a change in normal force coefficient is only important if it is varied by a significant factor but not merely by 10 percent.

The validity of the use of a constant normal force coefficient is substantiated in Figure B-2 within the described limits for high speed rotochute performance. It becomes evident from the curves and the particular equations that for advance ratios higher than $\lambda_d = .4$ the drag coefficient varies almost directly with rotochute solidity. Some calculations were prepared for the determination of the rotochute equilibrium blade pitch angles in the range of advance ratios pertinent to this section.

Good agreement with experimental results were obtained. The calculation involved a blade strip analysis, wherein an iterative solution produced zero torque and the inflow angle, which is essentially equal to the blade angle of attack, was secured at several blade span stations for the prescribed range of advance ratio. Consistent with prior assumptions, induced velocity corrections were made where necessary. As a result of these calculations it was discovered that at the lower advance ratio of .4 the blade inflow angle varied from a value of 77 degrees at the root to 29 degrees at the tip section. At the advance ratio of 1.6 the blade inflow angle varied from 86 degrees at the root to only 57 degrees at the tip. This points out, for the cases noted and can be generally stated, that more significant changes in blade

angle of attack takes place in the low advance ratio regime where the airfoil characteristics vary appreciably with blade section angle. At the higher advance ratio, the blade angle of attack for the particular example cited changed only half as much. What was more significant is that at the higher advance ratio the blade tip angles of attack are substantially higher than in the low velocity regime. Consequently, from basic airfoil data in the region of blade angles of attack, from 45 to 90 degrees, it was found that the chord force for an NACA 0012 airfoil section is negligible and the slope of the normal force coefficient becomes shallow. These findings are entirely consistant with the simplifying assumption of neglecting the blade pitch angle $\theta$ employed in the analytical high speed rotochute performance calculations.

Effect of Blade Mass Characteristics

The effect of blade mass characteristics on high speed rotochute performance may be studied by means of the modified Lock number $\bar{\gamma}$, a nondimensional coefficient that relates the air forces and mass forces on the blade. For a given blade geometry increasing the mass decreases $\bar{\gamma}$, which in turn modifies the coning angle and consequently $C_{D_R}$. Thus convenient parametric studies can be made of specific rotochute designs with regard to both performance and structural considerations.

The analytical studies embodying the proposed prototype configuration illustrates the significance of $\bar{\gamma}$, as a design parameter. By reference to table B-1, it may be noted that for the initial and final prototypes considered that only the mass characteristics have been changed. In Figure B-3, the effect of the mass change may be observed

from the shape and slope of the representative retardation curves. The results are understood upon examination of the coning angle expression where, for the case of the prototype, the decrease in $\bar{\gamma}$, reduced $\beta$ to a value below that of the initial prototype at each respective advance ratio considered. Then from the rotochute drag coefficient expression (Equation B-23) it is seen that this smaller cone angle yields a higher numerical value in the $\cos^3\beta$ term and consequently serves to increase everywhere the $C_{D_R}$ value of the final prototype. For the coning angle range associated with the operational rotochute the incremental change of $C_{D_R}$ between the initial and final prototype becomes more pronounced because of the effect of this cosine cubed function at the larger angles of attack of the high advance ratio regime. Therefore, in the low velocity region only a small difference of $C_{D_R}$ exists between the curves of Figure B-3. However, the incremental difference becomes quite substantial with increasing advance ratios and is due to the larger difference between the $\cos^3\beta$ terms in the drag coefficient expression.

The high speed performance of a rotochute can be satisfactorily predicted, as has been herein illustrated. It should be noted that the modified Lock's parameter $\bar{\gamma}$, can be employed in probing the capabilities of a preliminary rotochute design.

TABLE B-I

CONFIGURATIONS AND RELATED
QUANTITIES USED IN CALCULATIONS

| SYMBOLS | UNITS | MODEL | MODEL | INITIAL PROTOTYPE | FINAL PROTOTYPE |
|---|---|---|---|---|---|
| $\rho$ | Slugs | .0638 | .0808 | 1.028 | 1.52 |
| $e$ | Ft. | .1302 | .1927 | .5833 | .5833 |
| $S_s$ | Slug Ft. | .0353 | .0495 | 3.7693 | 6.21 |
| $I_s$ | Slug Ft.$^2$ | .0388 | .0562 | 24.0 | 37.2 |
| $I_x$ | Slug Ft.$^2$ | .0374 | .0555 | —— | —— |
| $\bar{Y}$ | —— | —— | —— | 1.142 | .733 |
| $h$ | Ft. | .1457 | .0936 | —— | —— |
| $c$ | Ft. | .333 | .50 | —— | —— |
| $c_1$ | Ft. | —— | —— | 1.0834 | 1.0834 |
| $c_2$ | Ft. | —— | —— | .9167 | .9167 |
| $R$ | Ft. | 2.0 | 2.0 | 10.0 | 10.0 |
| $\rho$ | Slug Ft.$^3$ | .0020 | .00217 | .002378 | .002378 |
| $\sigma$ | —— | .106, .215 | .318 | —— | —— |
| $Y_1$ | Ft. | —— | —— | 5.9167 | 5.9167 |
| $C_N$ | —— | 1.4, 1.6, 1.8 | 1.4, 1.6, 1.8 | 1.6 | 1.6 |
| $b$ | —— | 2 & 4 | 4 | 4 | 4 |

## C. OPENING CYCLE ANALYSIS

In a practical rotochute, the blades are required to fold back along the rotor axis so that the drag of the unit while installed on an airplane is at a minimum. The requirement of opening the blades after separation from the airplane then becomes a consideration. The method used to open the blades in the Kaman rotochute makes use of a governor spring which, when released, pushes the blades out into the airstream to a predetermined position.

An analytical means of predicting the opening cycle time histories of the rotochute with these initial conditions is then necessary. To obtain equations for the rotochute opening cycle, the sequence for the opening was studied in three parts. The first part included the starting torque and covered the cycle up to the time when the blade cone angle started to change. The second part covered the time from the start of coning to the time when the governing action began. The third part covered the time from the start of governing action to the time when complete opening was achieved.

The time required to open the rotochute fully is desired to be a minimum so that the maximum retardation can be reached without unnecessary delay. Blade parameters such as pre-cone angle, sweep angle, and pitch angle were studied to determine their effect on opening time.

UNCLASSIFIED

Starting Torque

Initial sweep and pre-cone angles are given to the rotochute blades by a spring action which is triggered by the separation of the tail

cone from the retochute. Aerodynamic forces resulting from these sweep and cone angles produce a torque about the retochute axis of rotation. It is this torque which starts rotation. The equations for the starting torque are developed as follows:

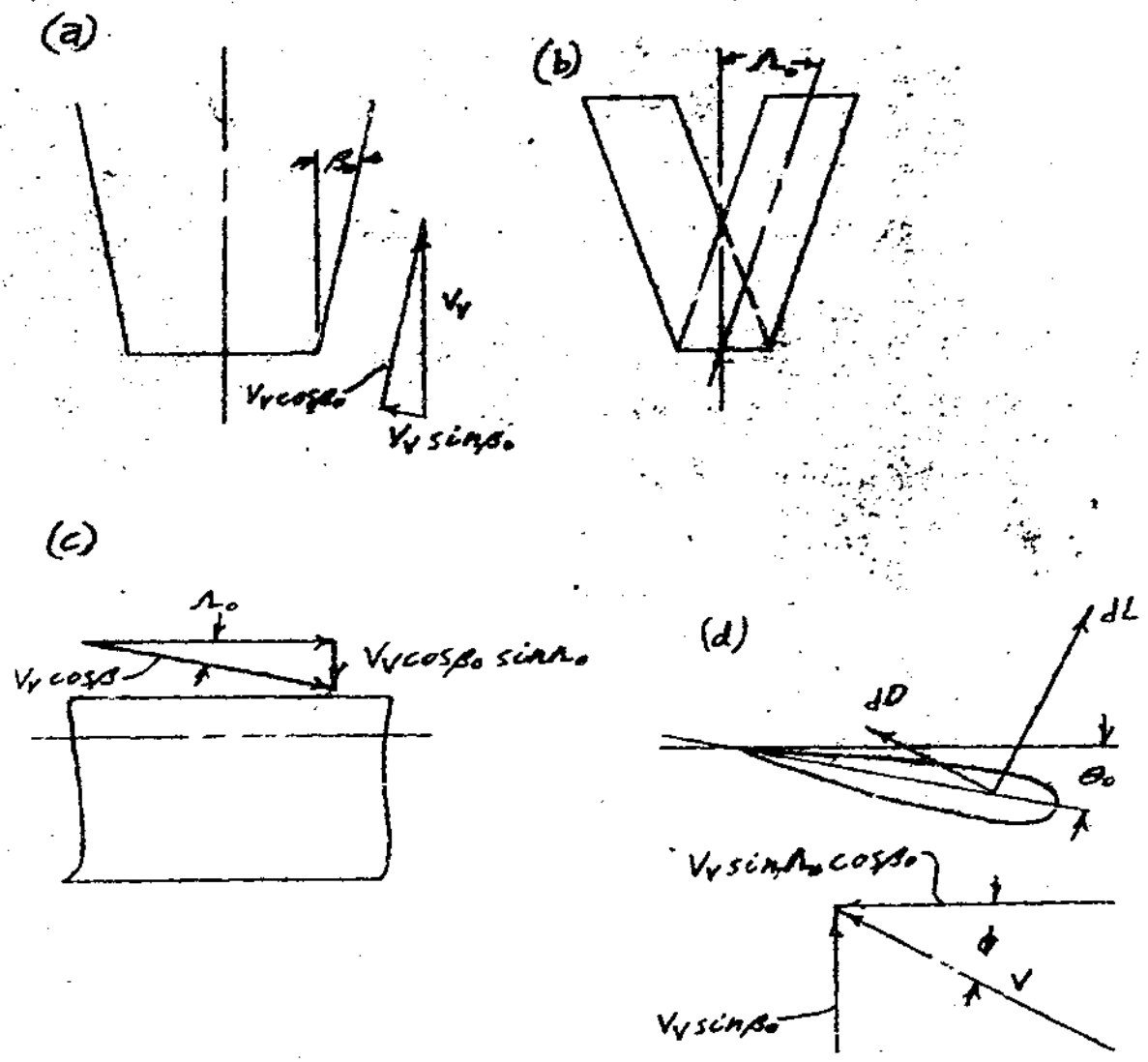

Sketches a, b, c, and d show how the descent velocity was resolved into a resultant velocity acting in the plane parallel to the chord line.

The spanwise air flow over the blade is complicated and there are no practical means of including this effect in the equations. However, its qualitative effect is known and was included when [redacted] the equations. A discussion of the spanwise flow is included as part of the section on Low Speed Performance. The spanwise air flow over a blade results in the formation of vortices which act in a fashion similar to end plates. The exact effect of the spanwise flow on the magnitude of the forces acting on the blade is largely unknown, but as pointed out in the Low Speed Performance section, both the $C_l$ and the $C_d$ of the blade would increase. The net effect of this increase on the starting torque should be small. The action of the tip vortices however, and the constant air flow over the blade results in a spanwise loading distribution which is very nearly uniform. Using this distribution, a representative station was chosen at which all of the aerodynamic forces are considered to be acting. Also because of the uniform spanwise distribution, the velocity and the blade angle of attack are uniform along the blade. With this information and using airfoil section characteristics for a NACA 0012 airfoil obtained from Reference 12 and corrected for Reynolds number, the lift and drag forces acting on the blade can be calculated.

Referring to sketch (d):

$$V = \left[V_v^2\left(\sin^2\beta_o + \sin^2\Lambda_o \cos^2\beta_o\right)\right]^{\frac{1}{2}} \qquad \text{(C-1)}$$

$$\phi = \tan^{-1}\frac{V_v \sin\beta_o}{V_v \sin\Lambda_o \cos\beta_o} = \tan^{-1}\left(\tan\beta_o \csc\Lambda_o\right) \qquad \text{(C-2)}$$

[redacted]

$$L = \frac{1}{2}\rho V^2 C_l A_R \qquad \text{(C-3)}$$

$$D = \frac{1}{2}\rho V^2 C_d A_R \qquad \text{(C-4)}$$

(e)

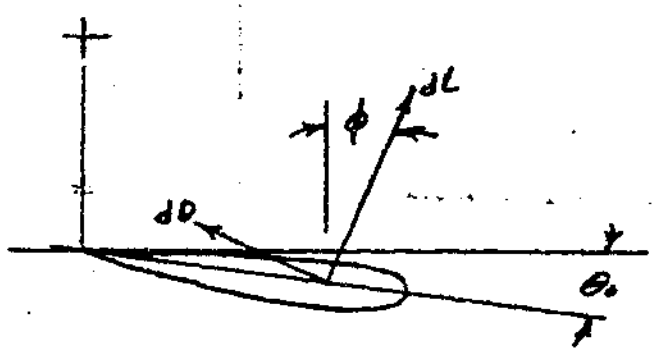


The starting torque is obtained by taking components of the lift and the drag forces and applying them to the representative station. Referring now to sketch (e).

$$Q/\text{blade} = \frac{1}{2}\rho c V_V^2 \left(\sin^2\beta_0 + \sin^2\lambda_0 \cos^2\beta_0\right) \qquad \text{(C-5)}$$

$$\left[(C_l \sin\beta_0 - C_d \sin\lambda_0 \cos\beta_0)(e\bar{R} + R'\bar{R}\cos^2\beta_0) + (C_l \sin\lambda_0 \cos\beta_0 + C_d \sin\beta_0)(\bar{R}R'\sin\lambda_0)\right]$$

The rotational acceleration was found to be constant up to the point where the blades open. The fact that the tip speed was negligible compared to the resultant velocity acting on the blade accounts for the constant torque acting on the rotochute. The centrifugal force resulting from rotational velocity determines the point where the rotochute will start to open. At this point both the flapping velocity and the flapping acceleration are equal to zero. The flapping equation, derived in Appendix II, with $\ddot{\beta} = \dot{\beta} = 0$ is:

$$\ddot{\psi}\left[f S_s \sin\beta \cos\Lambda - e S_s \sin\beta \sin\Lambda\right] + \dot{\psi}^2\left[I_s \sin\beta \cos\beta + e S_s \sin\beta \cos\Lambda + f S_s \sin\beta \sin\Lambda\right] = M_f \qquad \text{(C-6)}$$

With the rotational velocity added to the initial velocity vector diagram, equations (C-1 and (C-2) now become:

$$V = \left[V_V^2 \sin^2\beta_0 + \left(V_V \cos\beta_0 \sin\Lambda_0 + \Lambda(e + r\sin\beta_0)\right)^2\right]^{\frac{1}{2}} \qquad \text{(C-7)}$$

$$\alpha = \theta_0 + \phi = \theta_0 + \tan^{-1}\frac{V_V \sin\beta_0}{V_V \cos\beta_0 \sin\Lambda_0 + \Lambda(e + r\sin\beta_0)} \qquad \text{(C-8)}$$

Using these equations and following the method used in finding the starting torque, the aerodynamic flapping moment is expressed as:

$$M_f = \frac{1}{2}\rho \int_{SPAN} V^2 c \left(C_l \cos\phi + C_d \sin\phi\right) r\, dr \qquad \text{(C-9)}$$

Results obtained with equations (C-6), (C-7), (C-8) and (C-9) are shown in Figures C-3 and C-4. The effect of varying $\beta_0$ and $\Lambda_0$ is also shown on the curves. Figure C-4 shows the linear variation of the rotational speed with time as well as the variation of the time required for opening

with $\beta_0$ and $\Lambda_0$. Because of the rate change of rotational speed with time and the change in rotational speed needed to open the rotochute which occurs with a change in $\beta_0$ and $\Lambda_0$, the time required to start the opening cycle can be reduced appreciably by the proper choice of these angles.

Figure C-4 indicates that the highest rotational speed for the shortest period of time will be obtained with a high value of initial cone and a high value of initial sweep. There is a limit on the size of sweep and cone that can be set because of the difficulty of pushing the blades far out into the airstream by spring action. Figure C-3 shows that the rotational speed required to open the rotochute is greater for the larger sweep angle if the cone angle is kept constant.

Rotochute Opening to the Point where Governing Action Starts

Once the rotochute starts to open, the system must be analyzed in the two degrees of freedom, flapping and rotating. The dynamic equations for these two degrees of freedom are derived in Appendix II and the final equations are presented here.

Rotating:

$$\ddot{\psi}\left[f^2P+e^2P+I_s\cos^2\beta+2eS_s\cos\beta\cos\Lambda+2fS_s\cos\beta\sin\Lambda\right]+\ddot{\beta}\left[fS_s\sin\beta\cos\Lambda-eS_s\sin\beta\sin\Lambda\right]+\dot{\psi}\dot{\beta}\left[-2I_s\sin\beta\cos\beta-2eS_s\sin\beta\cos\Lambda-2fS_s\sin\beta\sin\Lambda\right]+\dot{\beta}^2\left[fS_s\cos\beta\cos\Lambda-eS_s\cos\beta\sin\Lambda\right]=Q \quad \text{(C-10)}$$

UNCLASSIFIED

Flapping:

$$\ddot{\psi}\left[fS_s\sin\beta\cos\Lambda-eS_s\sin\beta\sin\Lambda\right]+\ddot{\beta}\left[I_s\sin^2\beta+I_s\cos^2\beta\cos^2\Lambda\right]+\dot{\psi}^2\left[I_s\sin\beta\cos\beta+eS_s\sin\beta\cos\Lambda+fS_s\sin\beta\sin\Lambda\right]+\dot{\beta}^2\left[I_s\sin\beta\cos\beta\sin^2\Lambda\right]=M_F \quad \text{(C-11)}$$

The rotational acceleration term in the flapping equation is small and can be neglected. Aerodynamic forces were again handled in a manner similar to that used for the starting tempo. The velocity and the angle of attack were both corrected by including the flapping velocity term.

Sketch (f) illustrates the velocities now acting at any blade element and equations C-12 and C-13 express the new resultant velocity and angle of attack.

(f)

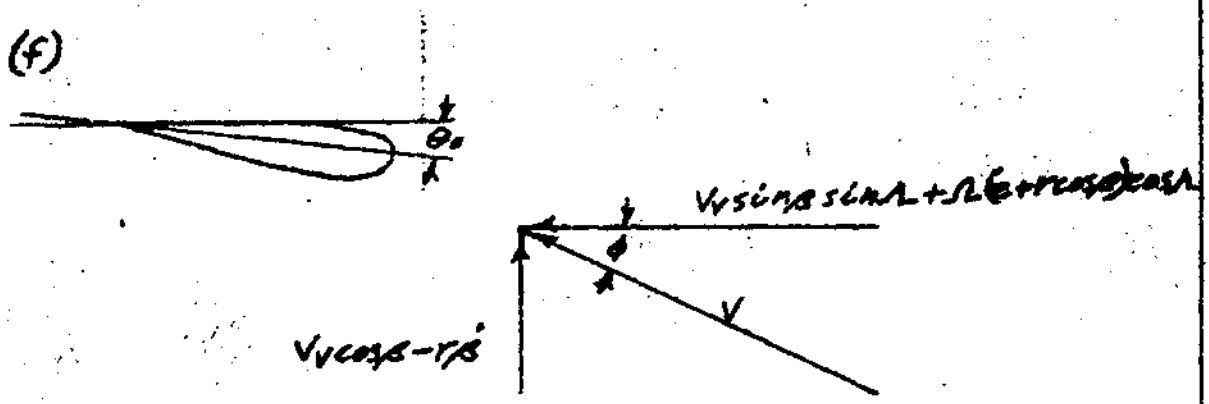


$$V = \left\{[V_V \cos\beta + r\dot{\beta}]^2 + [V_V \sin\beta \sin\Lambda + \Omega(e + r\cos\beta)\cos\Lambda]^2\right\}^{\frac{1}{2}} \qquad \text{(C-12)}$$

$$\alpha = \theta + \phi = \theta + \tan^{-1}\frac{V_V \cos\beta - r\dot{\beta}}{V_V \sin\beta \sin\Lambda + \Omega(e + r\cos\beta)\cos\Lambda} \qquad \text{(C-13)}$$

The aerodynamic forces were written as components which would be normal and chordwise to a plane of zero pitch.

$$dN = \tfrac{1}{2}\rho c\left\{[V_V \cos\beta - r\dot{\beta}]^2 + [V_V \sin\beta \sin\Lambda + \Omega(e + r\cos\beta)\cos\Lambda]^2\right\}^{\frac{1}{2}}\left\{C_l[V_V \sin\beta \sin\Lambda + \Omega(e + r\cos\beta)\cos\Lambda] + C_d[V_V \cos\beta - r\dot{\beta}]\right\}dr \qquad \text{(C-14)}$$

$$dC_f = \frac{1}{2}\rho c\left\{\left[V_V\cos\beta - r\dot{\beta}\right]^2 + \left[V_V\sin\beta\sin\Lambda + \Omega(e + r\cos\beta)\cos\Lambda\right]^2\right\}^{\frac{1}{2}}\left\{C_l\left[V_V\cos\beta - r\dot{\beta}\right] - C_d\left[V_V\sin\beta\sin\Lambda + \Omega(e + r\cos\beta)\cos\Lambda\right]\right\}dr \qquad \text{(C-15)}$$

The flapping moment and the torque acting on the blades at any time can now be expressed as:

$$M_f = \int_{SPAN} r\,dN \qquad \text{(C-16)}$$

$$Q = \int_{SPAN}\left[(e + r\cos\beta)dC_f + r\sin\Lambda\,dN\right] \qquad \text{(C-17)}$$

The torque and flapping moment would be given by integrating equations C-16 and C-17. There would be a great deal of work involved, however, in doing this integration by hand at each time interval chosen. As a simplification, a representative station was chosen on the basis of an integration performed at the beginning of the calculations. This station was checked frequently throughout the opening cycle so that a revision of the representative station could be made if needed. The check was made by comparing the results obtained from a spanwise integration with those from a representative station.

All of the calculations were for a high speed condition for which there were wind tunnel records available. The equations were solved using the Runge-Kutta method from which the accuracy obtained from the integration can be established and the time interval to be used to maintain an acceptable degree of accuracy can be determined. The results are shown in Figures C-9 and C-10. The effect of sweep angle soon vanishes with increasing tip speed and the effect of pitch angle becomes less signi-

ficant as $\phi$ gets larger, therefore, for simplicity of solution, these parameters can be considered constant with little error resulting.

To include the variation of the sweep and the cone angles in the opening cycle is beyond the scope of this analysis which was calculated by hand. However, the equation required for the variation of sweep angle is:

$$\Lambda = \Lambda_0 + \tan^{-1}(\tan\theta_N \sin\beta) - \mu + \delta \qquad \text{(C-18)}$$

where $\mu$ and $\delta$ are defined in Figure D-1 and $\delta$ is equal to zero until the governing action starts.

Start of Governing Action

Governing action starts when the centrifugal and aerodynamic moments exceed the spring moment about the blade pitching axis. To continue beyond this condition, the feathering degree of freedom must be considered in the analysis. The centrifugal feathering moment acting on the blade tending to change its pitch was approximated by the equation:

$$M_{CT} = P\Omega^2 (e + r\cos\beta)\, j \qquad \text{(C-19)}$$

The aerodynamic forces were calculated in the same manner as in the opening cycle, that is from equations C-14 and C-15. The moments were considered in two parts; one tending to sweep the blade forward, thereby pitching it; and the other twisting the blade about the forward bearing.

Thus,

$$M_{AF_1} = N\sin\beta\, \bar{r}_I - C_f\, r\cos\beta \qquad \text{(C-20)}$$

$$M_{AF_2} = N\, \bar{r}_I \cos\beta \qquad \text{(C-21)}$$

These moments were combined with the centrifugal moment and then resolved into forces acting on the governor crank.

Thus,

$$F_1 = [P\Omega^2(e + r\cos\beta)j - N\bar{x}_I \sin\beta + C_f r\cos\beta]/d \qquad \text{(C-22)}$$

$$F_2 = [N\bar{x}_I \cos\beta]/d \qquad \text{(C-23)}$$

(g)

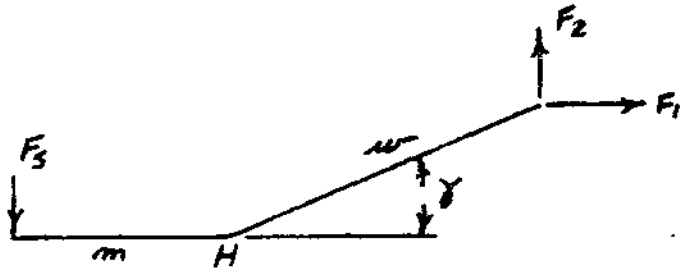


Sketch (g) shows the forces acting on the governor crank. Equilibrium about the fixed point H then requires that:

$$F_s m + F_2 w \cos\gamma - F_1 w \sin\gamma = 0 \qquad \text{(C-24)}$$

Knowing the spring preload, the spring force is determined and the above equation can then be solved for the rotational speed. The point where governing begins is shown in Figures C-6, C-7 and C-8. The point calculated using experimental thrust values is somewhat higher than the point determined by using calculated aerodynamic forces. The reason for this difference is that in the calculations using experimental thrust, there

was no feasible way of determining the chordwise forces acting on the blade and, therefore, these forces were not taken into account.

Opening Cycle with Governing Action

The equation for the third degree of freedom must now be added to the two equations already used in order to continue the calculations. This equation, for the pitching degree of freedom is discussed in the section concerning governor operation.

For a rapid approximation of the opening time, the governor can be ignored completely and the calculations for the opening cycle carried out to the point where the steady state rotational speed determined by torque equilibrium is reached. The error introduced by this approximation is rather small compared to the total opening time and does not prevent a qualitative comparison of effects of the initial opening parameters on the opening time from being obtained.

Prototype Opening Time

A method is presented whereby the opening time of any rotochute can be estimated by a comparison of its characteristics with those of the model. For purposes of preliminary design, this method is quite useful since the opening time for a great variety of designs can be quickly determined. For the final design, however, it would be worthwhile to repeat the calculations outlined in the preceding parts using the proper parameters.

For the purposes of this analysis, a constant acceleration and a constant torque can be applied throughout the opening cycle. This implies that the rotational speed varies linearly with time throughout the opening cycle. The total opening time is the same whether the actual or the linear

variation of rotational speed is considered.

Thus,

$$Q = I_z \ddot{\psi} \tag{C-25}$$

$$\ddot{\psi} = \frac{}{I_z} = \frac{\frac{1}{2}\rho V_V^2 C_D A R'}{I_z} = \frac{q C_D A R'}{I_z} \tag{C-26}$$

where the symbols are defined in the list of symbols.

The design maximum tip speed of the prototype rotochute during the opening cycle following the release of the vehicle at 0.9 Mach number will be essentially that experienced on the model during the opening studies conducted in the wind tunnel at 0.7 Mach number. Therefore, the time required for the prototype to reach full rotational speed can be evaluated with relation to the model results by the following condition:

$$\Omega_M R_M = \Omega_P R_P \tag{C-27}$$

$$\frac{\Omega_P}{\Omega_M} = \frac{R_M}{R_M(SF)} = \frac{1}{SF} \tag{C-28}$$

where the subscripts M and P stand for the model and prototype respectively.

By using equation C-28 and the fact that the acceleration is constant for the whole opening time, one can write the equation:

$$t_P = \frac{\dot{\psi}_P}{\ddot{\psi}_P} = \frac{\dot{\psi}_M / SF}{\ddot{\psi}_P} = \frac{\ddot{\psi}_M t_M / SF}{\ddot{\psi}_P} = \frac{\ddot{\psi}_M t_M}{\ddot{\psi}_P \, SF} \tag{C-29}$$

Now, it is necessary to find a ratio of the acceleration of the model to that of the prototype. The $I_z$ at the initial cone angle and

at the fully open position is as follows:

At the initial opening cone angle $\beta = 85^\circ$

$I_z$ prototype = 5.33 slug-ft$^2$

$I_z$ model = 0.0285 slug-ft$^2$

At the condition of the fully open rotochute $\beta = 0^\circ$

$I_z$ prototype = 163.74 slug-ft$^2$

$I_z$ model = 0.071 slug-ft$^2$

The above values given for the inertia do not follow the scaling of the rotochute. The inertia of the prototype should be the scale factor raised to the fifth power times the inertia of the model if the model is a true replica of the prototype. The principal reason for the discrepancy is the hub inertia. With the model blades at a flat cone, the hub inertia is approximately half of the total rotochute inertia. With the blades folded back, the hub inertia will be an even greater percentage of the complete inertia. The prototype hub inertia is substantially less than that predicted by scaling up the inertia of the model hub. In the flat cone condition for the prototype, the hub inertia is less than one percent of the total rotochute inertia. The inertia of the prototype blades was also not at the value predicted by scaling, although they were much closer to being the model blade inertia scaled up than the prototype hub was to the model hub.

The prototype and the model also differ in some of the aerodynamic terms. This difference occurs because the model was operating at a Mach number of 0.7 in a wind tunnel, whereas the prototype is operating at a Mach number of 0.9 at an altitude of 5,000 feet in free air.

For the prototype

$V_v$ = 1000 ft/sec

$\rho$ = 0.00205 slugs/ft$^3$

For the model opening cycle for which the opening time is available:

$V_v$ = 761 ft/sec

$\rho$ = 0.00188 slugs/ft$^3$

The opening time which was available was for a one-fifth scale model of the prototype. The scale factor (SF) is, therefore, 5. For the prototype with SF = 5 and $\beta = 85^\circ$ one can write from equation C-26.

$$\ddot{\psi}_P = \frac{(1025)(AR')(SF)^3}{5.33} = 26{,}400(AR') \qquad \text{(C-30)}$$

For the model

$$\ddot{\psi}_M = \frac{(525)(AR')}{0.0285} = 18{,}400(AR') \qquad \text{(C-31)}$$

therefore:

$$\left(\frac{\ddot{\psi}_P}{\ddot{\psi}_M}\right)_{\beta = 85^\circ} = 1.435 \qquad \text{(C-32)}$$

For $\beta = 0$, R' = 0.6R, and noting that equation C-27 gives R' = constant = 529 ft/sec one can find V for both the model and the prototype from equation C-7.

$$V_{vM} = (761)^2 + (529)^2 \;^{1/2} = 8.59 \times 10^5 \;^{1/2} \qquad \text{(C-33)}$$

$$V_{vP} = (1000)^2 + (529)^2 \;^{1/2} = 1.28 \times 10^6 \;^{1/2} \qquad \text{(C-34)}$$

Using equation C-26, $\ddot{\psi}$ for both the model and the prototype can now be found.

$$\ddot{\psi}_P = \frac{(1.28 \times 10^6)(0.00205)(AR')(SF)^3}{(163.74)} = 2 \times 10^3 (AR') \quad \text{(C-35)}$$

$$\ddot{\psi}_M = \frac{(8.59 \times 10^5)(0.00188)(AR')}{0.071} = 2.27 \times 10^4 (AR') \quad \text{(C-36)}$$

therefore

$$\left(\frac{\ddot{\psi}_P}{\ddot{\psi}_M}\right)_{\beta = 0^\circ} = 0.088 \quad \text{(C-37)}$$

An average value of $(\ddot{\psi}_P / \ddot{\psi}_M)$ was calculated which can be applied throughout the opening cycle.

$$\left(\frac{\ddot{\psi}_P}{\ddot{\psi}_M}\right)_{AVG.} = \frac{\left(\ddot{\psi}_P/\ddot{\psi}_M\right)_{\beta=85^\circ} + \left(\ddot{\psi}_P/\ddot{\psi}_M\right)_{\beta=0^\circ}}{2} = 0.76 \quad \text{(C-38)}$$

Using equations C-29 and C-38 the opening time for the prototype can now be expressed as a function of the opening time of the model as:

$$t_P = \frac{t_M}{(0.76)(5)} = 0.263\, t_M \quad \text{(C-39)}$$

The opening time of the model for which the curves are presented is 0.8 seconds. Using this value in equation C-39 an estimate of the opening time for the prototype can be obtained and is 0.21 seconds. This value of 0.21 seconds is well within the time specified for opening. If it is required that the tip speed of the prototype be something other than the tip speed of the model, equations C-27 and C-28 must be corrected as follows:

$$\Omega_M R_M = \Omega_P R_P \quad \text{(C-40)}$$

$$\frac{\Omega_P}{\Omega_M} = \frac{R_M}{R_M(SF)} \Xi = \frac{\Xi}{SF}$$

(C-41)

where $\Xi$ is the factor by which the tip speed of the model differs from that of the prototype. The rest of the equations remain unchanged except where this ratio appears.

It should be noted that the opening time can be appreciably affected by the initial values of the cone and sweep angles. The effect of these values has already been discussed, but it should be pointed out that the values of $\beta_0$ and $\Lambda_0$ used for the model opening cycle were those that give the smallest starting torque. With the proper choice of initial values for the sweep and the cone angles, the opening time of the prototype could be made very small.

Wind Tunnel Test Results

The results obtained with equation C-5 are shown in Figure C-1 compared with the wind tunnel test results. The calculated starting torques increase linearly with dynamic pressure, but the test results indicate that the rate at which the starting torques increase becomes less at the higher dynamic pressures. This discrepancy in the shape of the curves can easily be explained by the fact that in the analysis the blades were considered to be rigid for purposes of simplicity whereas in the test, there was a slight amount of bending which increased with velocity. This bending should result in a lower torque due to the decrease in the air loads and in the moment-arms resulting from the smaller cone angles at the outboard sections of the blade. Figure C-1 indicates that for the high sweep angles, good agreement was reached in the comparison of calculated starting torques with experimental starting torques. For the smaller sweep angles the

agreement was also good at the high cone angles but not at the lower sweep angles. For the purpose of calculating the time histories of the remainder of the opening cycle the starting torque measured in the test was used. By using the experimental value rather than the calculated value a quantitative as well as a qualitative check of the method developed for calculating the time histories of the rotational speed and the cone angle could be made.

Wing tunnel results for the opening cycle are shown in Figures C-6, C-7 and C-8. On the experimental curve of rotational velocity versus time (Figure C-6) both the point where opening starts and the point where governing begins are marked. It can be seen that up to the time there opening starts, the curve is linear as was previously determined. From the start of opening to where governing starts, there is a rapid increase in the rotational acceleration, followed by a decrease in the rotational acceleration until an equilibrium value of rotational speed is reached.

In Figure C-7, the curve of thrust versus time, the same boundaries are marked and the thrust is seen to be zero before the rotochute opens. After opening, the thrust follows much the same pattern as the rotational velocity with the rapid increase in thrust up to the point where governing starts and thereafter a lesser rate of increase.

Figure C-8 shows three points. The point where the initial sweep and cone angles are reached, the point where opening begins, and the point where governing begins. Once again, the curve follows the same pattern after opening starts with a rapid coning change up to the point where the governor action starts and a less rapid coning thereafter until a constant value is reached.

## D. ROTATIONAL SPEED GOVERNING

### Purpose of Governing

The rotochute rotational speed can be controlled throughout the speed range by appropriate blade pitch changes. In the Kaman rotochute the pitch changes are brought about by a balance between a centrifugal feathering moment and the feathering moments contributed by a spring and the aerodynamic force. This balance is called governing and is obtained by means of a governor mechanism utilizing the principles of the conventional fly ball governor to maintain a prescribed rotor speed-velocity relationship. That a governor is necessary for optimum performance can be understood from the following considerations.

As described in the previous section, the balance of torque, which autorotation requires, defines a blade pitch angle, $\theta$, at each velocity-tip speed ratio. This is an aerodynamic requirement based on a balance between an accelerating torque due to blade lift and a decelerating torque due to blade drag. The performance equations of the previous sections show that the rotor thrust coefficient increases as the velocity-tip speed ratio is reduced (Figure B-2). This is a result of a reduction in blade section drag coefficient and an increase in blade lift coefficient as the average blade angle of attack is reduced from 90°. At the same time the pitch angle progresses in a positive direction to maintain the balance of torque. A fixed pitch rotochute, for example, would operate at only one value of velocity-tip speed ratio, $\lambda$, with a corresponding constant rotor thrust coefficient. It would therefore be desirable to operate the fixed

pitch rotochute at the peak value of rotor drag coefficient $C_{D_R}$. This peak value occurs at a velocity-tip speed ratio between .10 and .20 depending somewhat on the rotor solidity. If the release velocity were 1000 ft/sec, the tip speed would have to be of the order of 5 to 10 times this value. This, of course, would be impossible to achieve because of compressibility and the stringent structural requirements. Consequently, the only alternative is to operate the fixed pitch rotochute at a higher value of velocity-tip speed ratio and accept the corresponding lower value of rotor drag coefficient. The addition of a governor to the same system permits the pitch and consequently the advance ratio to change in a manner consistent with the aerodynamic torque balance requirement. The maximum rotor drag coefficient aerodynamically attainable can therefore be achieved throughout the flight path. By proper choice of pitch change mechanism and governor characteristics the maximum tip speed consistent with structural limits can be achieved and the tip speed controlled over the complete range of operation.

Operation of the Governor

The operation of the governor can probably be best described by considering its action step by step. After the rotor has opened under the influence of the starting torque (See Section C on The Opening Cycle), the centrifugal force moment increases enough to change the pitch in a positive direction against the spring moment. As the velocity decreases along the flight path, the decelerating component (blade drag) begins to dominate and the rotor tends to lose rotational speed. This decrease in rotational

speed reduces the contribution of centrifugal force to feathering equilibrium and the spring moment changes the blade pitch to a slightly more negative angle. An accelerating torque due to blade lift then dominates and leads to a higher rotational speed than would have been obtained at this lower velocity at the previous pitch angle. At the same time the change in blade pitch reduces the spring moment and a new feathering equilibrium is obtained. Thus, during the conditions of steadily changing velocity along the flight path, the governor adjusts the blade pitch to maintain the balance between centrifugal, aerodynamic and spring moments about the feathering axis. A more nearly constant RPM-velocity relation is therefore attained which results in a decreasing inflow ratio during the descent. The rotor drag coefficient increases as a consequence to the point where the maximum rotor drag coefficient is achieved near terminal descent.

So far only operation in the blade-stalled condition has been considered. In this flight regime, wherein the average blade angle of attack is considerably beyond the stall angle, the chordwise force coefficient approaches zero. The blade pitch angle is therefore near zero since the resultant force must be normal to the plane of rotation for autorotation. However, as the velocity along the flight path is reduced as a result of the time response of the rotochute to the developed thrust (drag force), and the higher level of rotational speed obtained through governing, the outer portion of the blade tends to become unstalled. A considerable amount of accelerating torque is therefore available to speed up the rotor. More of the blade span then becomes unstalled. In this

range the average blade chordwise force changes direction. For example, at high velocities the net chordwise force was decelerating. A slight negative pitch was consequently required to give a balancing component to the normal force. Near terminal descent, however, the predominant chordwise forces are in the accelerating direction which requires a positive blade pitch to supply the balancing component of normal force. Here again the governor plays a significant part. Since the accelerating torque tends to increase the rotational speed, the build up of centrifugal force introduces a more positive pitch which increases the decelerating component of the normal force. The rotor is consequently prevented from overspeeding yet it achieves optimum performance within design limits. The degree to which the rotational speed varies with velocity is a function of the detailed design of the governor. In general, considerable design flexibility is available in any particular governor system and the effectiveness of the centrifugal, aerodynamic and spring moments in providing equilibrium about the feathering axis can be varied. A satisfactory tip speed-velocity relationship can be attained which will give the optimum performance possible consistent with the aerodynamic characteristics of the rotochute with a given solidity and disc area.

Methods of Governing

The previous discussion indicates that in order to obtain optimum performance with reasonable structural limits, some form of governing is necessary. Early investigations of rotochute governing by Kaman Aircraft led to consideration of pitch-cone coupling (Delta 3) as an effective

governor, but it was found that a single delta 3 angle was not sensitive enough throughout the speed range. From an approximation to the actual required variation of pitch with coning angle necessitates at least two delta three angles, one for the partially stalled (low speed) regime and one for the completely stalled (high speed) regime. The design complications inherent in the above approach led to the consideration of spring governing. One possibility was to use a spring on each individual blade to balance the centrifugal moment. This has been a successful governing device on other rotochutes. Another spring, however, is necessary to set the precone and initial sweep angle to initiate a rotation. A single spring whose axis is located on the axis of rotation was used to set the precone angle and sweep angle on all the blades through a suitable linkage system. The use of the hub center spring to do the complete job of setting the precone and sweep angles as well as governing throughout the speed range led to a simpler design and was therefore adopted for the present application. The following sections will deal exclusively with the central spring governor as it is believed to be the simplest for the present application.

Governor Design Principles

The rotochute blades can be considered to be in feathering equilibrium under the influence of the centrifugal, aerodynamic and spring feathering moments. Figure D-1 shows a schematic diagram of the linkage system. The equation of equilibrium is:

UNCLASSIFIED

$$M_{CT}(\beta,\theta) = M_A(\beta,\theta) + M_{spr.}(\beta,\theta) \qquad \text{(D-1)}$$

Each of the moments in Eq. D-1, and the effect on them of various [redacted] and aerodynamic parameters will be discussed individually.

Centrifugal Feathering Moment - The equation for the contribution of centrifugal force moment to feathering equilibrium is derived in Appendix III. Based on the linkage system shown schematically in Figure D-1 this moment is as follows:

$$
\begin{aligned}
M_{CT} = \Omega^2 \Big\{ & f S_c \theta_h - I_c \theta_h - e S_c \theta_h \delta - I_c \theta_h \delta^2 + f S_c \delta \tan\gamma + e S_s \tan\gamma \\
& - [f S_s + I_p \theta_h^2 - I_p - e S_s \delta + I_p \theta_h^2 \delta^2 - I_p \delta^2 - f S_s \theta_h \delta \tan\gamma \\
& - f w P \tan\gamma + e w P \delta \tan\gamma - e S_s \theta_h \tan\gamma] \sin\beta \\
& - [-f h P - h S_c \theta_h^2 + h S_c + e h P \delta - h S_c \theta_h^2 \delta^2 + h S_c \delta^2 \\
& + f h P \theta_h \delta \tan\gamma - f S_s \tan\gamma + e S_s \delta \tan\gamma + e h P \theta_h \tan\gamma] \cos\beta \\
& + [I_c \theta_h + I_p \theta_h \delta^2] \sin^2\beta + [h^2 P \theta_h + h^2 P \theta_h \delta^2] \cos^2\beta \\
& - [2 h S_s \theta_h + 2 h S_s \theta_h \delta^2] \sin\beta \cos\beta \Big\}
\end{aligned}
\tag{D-2}
$$

The angles $\delta$, $\gamma$ and $\theta_h$ can be written as functions of $\theta$ and $\beta$ and the geometric constants of the system. These equations are as follows:

$$\tan\delta = \frac{d}{w} \sec\alpha_g \left( \frac{\tan^2\theta_h}{4} - \left(\frac{\pi}{\alpha_g}\right)^2 \tan\alpha_g \right) \tag{D-3}$$

$$\sin\theta_h \approx -\theta \sec\beta \tag{D-4}$$

$$\sin\gamma = \frac{d}{w} \cos\Delta \sec\delta \tan\theta_h + \sin\alpha_g \tag{D-5}$$

$$\text{or} \quad \cos\gamma = \frac{d}{w} \cos\Delta \tan\delta + \cos\alpha_g \tag{D-5a}$$

The definitions of the above symbols are given in the list of symbols. The values of $\theta$ and $\beta$ required for insertion into the above equations will be found when the aerodynamic feathering moment is discussed.

The above equation shows that the centrifugal feathering moment is directly proportional to the square of the rotational speed. The

effects of the pitch and coning angles on the centrifugal feathering moment however, are not quite so apparent, as they are also functions of the linkage geometry. Refer, for example to Figure D-2. At a pitch angle of zero the moment varies almost directly with the square of the rotational velocity. As soon as some pitch is introduced, however, the blade moves forward as well as outward with coning angle. The blade center of gravity is thus brought nearer to the feathering axis which relieves the reaction at the governor crank. Similarly, a variation of pitch at constant coning angle moves the blade center of gravity fore and aft as the angle $\delta$ changes (Figure D-2). At constant coning angle, the centrifugal feathering moment would be symmetrical about zero if the arc through which the flapping-hinge link moved were symmetrical about the plane of rotation. Care must be observed in designing a particular rotoslute, therefore, to distribute the weight, restrict the angles $\delta$ and $\beta$ and locate the feathering axis such that the blade center of gravity remains aft of a line from the center of rotation through the feathering pin. If in any flight condition the blade c.g. moved forward of this line, the centrifugal force moment would act in the same direction as the spring moment and there would be no governing.

Spring Feathering Moment - The spring moment determines the extent to which the centrifugal force governs the rotational speed. If this moment were zero, the blade would assume full positive pitch and come to a stop. If the spring stiffness were too great, the blade would assume full negative pitch and continue to accelerate, probably to destruction. In the present system, the spring feathering moment is developed as follows:

From Figure D-1,

The distance $\Delta L_1$ is obtained as follows:

$$FH = m - m\cos(\eta_M + \epsilon - \gamma)$$

and $$BD = \sqrt{n^2 - [m - m\cos(\eta_M + \epsilon - \gamma)]^2}$$

$$BF = \sqrt{n^2 - [m - m\cos(\eta_M + \epsilon - \gamma)]^2} + m\sin(\eta_M + \epsilon - \gamma)$$

$$\Delta L_1 = BF - s = n\sqrt{1 - \left(\frac{m}{n}\right)^2 [1 - \cos(\eta_M + \epsilon - \gamma)]^2} + m\sin(\eta_M + \epsilon - \gamma) - s \quad \text{(D-6)}$$

Now $$l_s = L_f - [L' - \Delta L_1 - \Delta L_2] \quad \text{(D-7)}$$

From equilibrium about the fulcrum of the governor crank, the force at the flapping-hinge crank joint:

$$F_{cj} = \frac{K l_s m}{b w \cos\gamma}$$

The feathering moment, therefore is:

$$M_{spr.} = -\frac{K l_s m}{b w \cos\gamma}[d\cos\Delta\sec\delta] \quad \text{(D-8)}$$

Since the angles $\delta$ and $\gamma$ are functions of the pitch and coning angles the spring moment too is a function of the pitch and coning angles.

In the equation for the deflected length of the spring, $l_s$ the term $\Delta L_2$ is the spring preload length. Preloading the spring has the effect of requiring a higher centrifugal moment to force the pitch link from the negative stop. Preload therefore, provides an effective control over the maximum rotational speed. For example, the aerodynamic requirement for optimum performance (the variation of $\beta$ and $\theta$ with advance ratio), together with the link geometry, determines the optimum spring rate. The effect of an increase in preload is an increase in the maximum tip speed and a decrease in the reduction in rotor drag coefficient after the stall.

Aerodynamic Feathering Moment - The aerodynamic moment is rather variable. Its importance to governor operation depends upon the flight regime. In calculating the aerodynamic feathering moment, it is convenient to consider separately the two general flow regimes; the stalled flow case (high speed) where the induced velocity is low but the coning angle is appreciable and the partially stalled case (low speed) where the coning angle is small, but the induced velocity is appreciable. In the low speed case, the effect of the aerodynamic moment on the feathering equilibrium can be considered negligible since the aerodynamic force at terminal velocity is of the order of 3 percent of the same force at high speed. The choice of the aerodynamic force moment arm can somewhat alter this figure but not appreciably.

The derivation of the equation for the aerodynamic feathering moment is presented in Appendix III and the result is as follows:

$$M_{AF} = -\frac{\rho}{2}(\Omega R)^2 c R \cos\beta \left\{ \sum_{y_R \sin\beta}^{1} \left[ C_n y_I \sin\theta_A \cos\delta \tan\gamma + \left(C_n \bar{x}_I + C_c\left[\tfrac{h}{R} - y_I \tan\beta\right]\cos\theta_A\right] \left[\left(y_I \cos\beta + \tfrac{e}{R}\right)^2 + (\lambda_d - \lambda_i)^2 \cos^2\beta\right] \Delta y_I \right\} \qquad \text{(D-9)}$$

In the above equation $C_n$ and $C_c$ are functions of the angle of attack at each station which is:

$$\alpha_T = \theta + \arctan \frac{(\lambda_d - \lambda_i)\cos\beta}{y_I \cos\beta + e/R} \qquad \text{(D-10)}$$

Again the feathering moment is a function of the pitch and cone angles. These angles must be calculated before the feathering equilibrium equation (Eq. D-1) can be solved for the spring constant K. They will be calculated for the high speed case using the following assumptions which appear

reasonable as a first approximation.

1. The angle $\theta$ is negligibly small compared to $\phi$.
2. $\lambda_i$ is constant across the disc.
3. $(e/R)^2$ and higher order terms are negligible.

Assumption 1 is reasonable since at the maximum flight velocity, or inflow ratio, the blade pitch angle approaches zero inasmuch as the blade section angles of attack approach 90° where the chordwise component of the resultant force disappears. For autorotation, therefore, the blade normal force must be normal to the plane of rotation. With these assumptions and utilizing the requirement of torque equilibrium, the blade pitch angle can be calculated for several points in the high speed regime.

$$Q = 0 = \text{Const.}\, R \sum_{r'/R}^{1} \frac{r'}{R} c_c \left(1 + \frac{C_n}{C_c} \tan\phi\right) \tag{D-11}$$

Now $C_n$ and $C_c$ are functions of the local blade angle of attack which, making use of assumptions 1 and 2 is:

$$\cot\phi_r \approx \cot\alpha_r = \frac{r'/R}{(\lambda_d - \lambda_i)\cos\beta}$$

$$\cot\alpha_r = \frac{e/R + h/R \sin\beta}{\lambda_d \cos\beta} + \frac{y_I - e/R}{\lambda_d} \tag{D-12}$$

where $r'/R = e/R + h/R \sin\beta + (y_I - e/R)\cos\beta$

The blade coning angle in this high speed flight regime can be determined separately in terms of the blade mass parameters using the equation derived in the high speed performance section:

$$\tan\beta = -\frac{eS_s + I_x}{2hS_s} + \sqrt{\left(\frac{eS_s + I_x}{2hS_s}\right)^2 + 1 + \frac{Pe}{S_s} + \frac{C_n \rho c (R-e)}{4S_s}\left\{\left(\frac{\lambda_d - \lambda_i}{4}\right)^2 \left(\frac{R}{R-e}\right)^2 + \frac{1}{3} + \frac{1}{3}\left(\frac{e}{R-e}\right)\right\}} \tag{D-13}$$

Substituting the values of $\epsilon$ determined by means of the preceding equation into the torque equilibrium (Eq. D-11) the values of $\theta$ can be calculated by a numerical integration. In the lower speed portion of the high speed regime, the effect of the induced velocity can be accounted for by re-cycling the torque equilibrium calculation using the momentum relation for the average induced velocity ratio derived in the high-speed performance section,

$$\lambda_i = \frac{\lambda_d}{2}\left[1 - \sqrt{1 - C_{oR}}\right]$$

In addition, if the values of $\theta$ are considered appreciable, they may be inserted in the expression for local angle of attack used in determining $C_n$ and $C_c$ and the torque equilibrium expression re-cycled again. Finally, good estimates of the pitch and cone angles are calculated. Although in the low speed regime the aerodynamic feathering moment is negligible, the pitch and coning angles are necessary for the calculation of the centrifugal and spring feathering moments. These angles are calculated as part of the solution for the low speed performance and the calculation has been discussed in that section.

Referring again to the aerodynamic feathering moment equation, (Eq. D-9) all the factors are now determined with the exception of $\bar{x}_I$, which is the distance from the chordwise center of pressure to the projection of the feathering axis measured parallel to the chord line. The values of center of pressure position from the leading edge can be obtained from airfoil data. In general for most airfoils, the center of pressure moves from near the quarter chord point at unstalled angles of attack to

[redacted]

near the 45 percent chord point at angles of attack corresponding to the high speed flight regime. The aerodynamic feathering moment can therefore be controlled by proper location of the feathering axis with respect to the high speed chordwise center of pressure. For example, if the value of $\bar{x}_r$ is relatively large (as was the case with the models) the aerodynamic moment combines with the spring moment to force the pitch angle in a negative direction. The spring must be made softer, therefore, to avoid excessive rotational speed. Then as the aerodynamic moment diminishes with the reduction in forward speed, the rotational speed would be reduced with a corresponding reduction in performance. It, therefore, seems desirable to locate the feathering axis closer to the stalled center of pressure position and govern primarily with a stiffer spring and centrifugal moments. This, incidentally, is the arrangement proposed in the prototype design.

In summarizing the governor design principles, the spring rate K must be the last characteristic determined. From the trajectory and weight specifications the general geometric and mass characteristics can be tentatively determined. A maximum rotational speed is chosen and the performance is calculated as outlined in the previous sections. As part of the performance analyses the coning angle variation along the trajectory can be determined. As part of the low speed performance analysis, the pitch angle $\theta$ required for autorotation is also determined. The required pitch angle in the high speed regime can also be determined by the torque balance, equation (Eq. D-11). Having the values of $\beta$ the required values of $\theta$, and the blade mass and geometric characteristics, the spring force and the rotational speed can be determined for any chosen



[redacted]

feathering axis location at the advance ratio for maximum rotational speed, by means of the feathering moment equilibrium equation. If the spring rate is too large to be practical, the feathering axis can be relocated.

Comparison with Wind Tunnel Tests

According to the feathering equilibrium equation, (Eq. D-1) the centrifugal and spring feathering moments can be determined if the angles $\rho$ and $\theta$ are known. Comparisons of these angles calculated according to the previously given equations with those measured in the wind tunnel tests are presented in Figures D-3 and D-4.

Consider first the variation of coning angle $\beta$, with advance ratio $\lambda_i$. A discrepancy of between 2 and 3 degrees exists throughout the flight range. Even though this discrepancy exists, the difference between the trigonometric functions of angles two or three degrees apart in this range, would have a negligible effect on the feathering equilibrium equation. A possible explanation for part of the discrepancy may be due to the wind tunnel model blade weight distribution. For example, in the wind tunnel model, the non-rigid blade bent under load so as to reduce the coning angle. As a consequence the coning angle near the hub, where the measurement was made, was greater than average. The calculated curve, however, was based on a rigid blade.

Consider now the comparison of pitch angles presented in Figure D-3. In the high speed range the agreement between the calculated and experimental values is fairly good and the trend is fairly well defined. At very high values of advance ratio, the average blade angle of attack

approaches that at which the blade chordwise force is zero. As a consequence the blade angle for autorotation approaches zero. Following the discussion under governor operation, the pitch angle becomes slightly negative then turns positive as the blade average chordwise force changes sign. This trend is shown in the calculated results. The calculations are based on a strip analysis in which two dimensional airfoil data in the high angle of attack range at the required Mach numbers and Reynolds numbers was assembled from References 3 to 12. These data may not represent exactly conditions on the blade. This fact together with the unknown effect of surface condition probably led to the discrepancies observed in the comparison.

In the low speed regime, the comparison also seems fairly good. Although the peak value of rotor drag coefficient $C_{D_R}$ has been calculated, the peak value of pitch angle was not. The peak rotor drag coefficient $C_{D_R}$ and the peak pitch angle do not occur at the same advance ratio. The peak rotor drag coefficient occurs when enough of the blade is stalled to reduce the ratio of thrust to dynamic pressure. The pitch angle, however, continues to increase until the average blade chordwise force changes sign since it depends on torque equilibrium. This occurs in the neighborhood of 24°. It is improbable that the peak value of $\theta$ can be calculated exactly because of the effect of spanwise flow described in the section on low speed performance.

The magnitude of the aerodynamic feathering moment can be obtained from the wind tunnel tests as the difference between the centrifugal and spring feathering moments. These moments were calculated using the

experimental values of pitch and cone angles. The aerodynamic feathering moment was also calculated using the experimental values of pitch and cone angles. A comparison of these two methods gives an indication of the accuracy of the equation. The comparison is shown in Figure D-[illegible]. Again the trend toward a negligible aerodynamic feathering moment as the advance ratio is reduced is apparent. There is good agreement between the calculated and experimental values at the higher advance ratios. The assumption that the induced velocity is uniformly distributed over the disc in this range of advance ratios is evidently valid as well as the assumption that a two-dimensional strip analysis is applicable. In preliminary design the spring rate is determined at the design maximum rotational speed which occurs in the range of high advance ratios. The spring rate so determined should therefore be accurate. At the lower values of advance ratio, however, the calculated and experimental results deviate, which indicates a gradual weakening of the validity of the assumptions. The value of the aerodynamic feathering moment in this range however, approaches zero.

In general, the analytical methods described in this section provide adequate means of determining the design parameters of a rotorcharte governing system for any reasonable set of specifications in the subsonic range of flight speeds.

## E. ROTOCHUTE TRAJECTORY ANALYSIS

The criteria that define a specific rotochute design are the trajectory requirements for the trajectory determines the effectiveness of the rotochute for a particular mission. Frequently a primary trajectory specification is the terminal velocity or the velocity existing at touch-down. The ground impact acceleration to which the system will be subjected is determined by the terminal velocity. Where a minimum terminal velocity is required in order to insure the delivery of the payload intact, it is desirable to operate at the maximum rotor drag coefficient. The analysis of the low speed flight condition, previously discussed, has indicated that a maximum drag coefficient exists when a major portion of the rotor blade is unstalled. The governed rotochute makes operation in this unstalled region possible by providing the necessary pitch angle changes to allow the development of maximum drag coefficient at low descent speeds without causing excessive tip speeds immediately following release at high velocities. As a result, the maximum retardation possible is attained for a particular rotor diameter, solidity, blade mass distribution, and design limit tip speed.

The trajectory requirements specified for the prototype rotochute designed under the Phase I contract were as follows:

a. The release velocity shall be 600 knots.

b. The release attitude shall be horizontal.

c. The release altitude shall be within the limits of from sea level to 5000 feet standard pressure altitude.

d. The velocity along the flight path at a point 200 feet below the release altitude shall be less than 130 ft./sec.

e. The range from the point of release to a point along the trajectory at an altitude of 200 feet below the release altitude shall be within the limits of from 2000 to 3000 feet.

f. The attitude angle to the vertical shall be 40 degrees or less at an altitude 200 feet below the release altitude.

g. The above trajectory specifications shall be met for a gross weight of 3000 pounds.

In addition to these trajectory requirements, it was necessary to meet certain size and fit limitations which would allow external aircraft carriage of the store as discussed in Reference 21. These requirements have defined the maximum blade chord and the maximum rotor diameter of the rotochute. A preliminary design study was made of the overall store in relation to aircraft fit and the blade stowage within an acceptable low drag store contour. As a result of this study a prototype configuration has been established with a maximum blade chord of 13 inches and a rotor diameter of 20 feet utilizing a two section telescoping blade. The remaining variables which govern the trajectory are the variation of rotor speed with flight velocity and the blade mass and mass distribution.

The solution of the rotochute trajectory was developed from the analysis of a mass traveling along a curved path through space having an initial velocity and being acted upon by a gravity force and a retarding force. Because of the expected stability of the rotochute vehicle the

retarding force or rotor thrust was considered to be tangent to the flight path at all times. A system of rectangular coordinates was selected to describe the position of the system at any time along the flight path as shown in the following sketch.

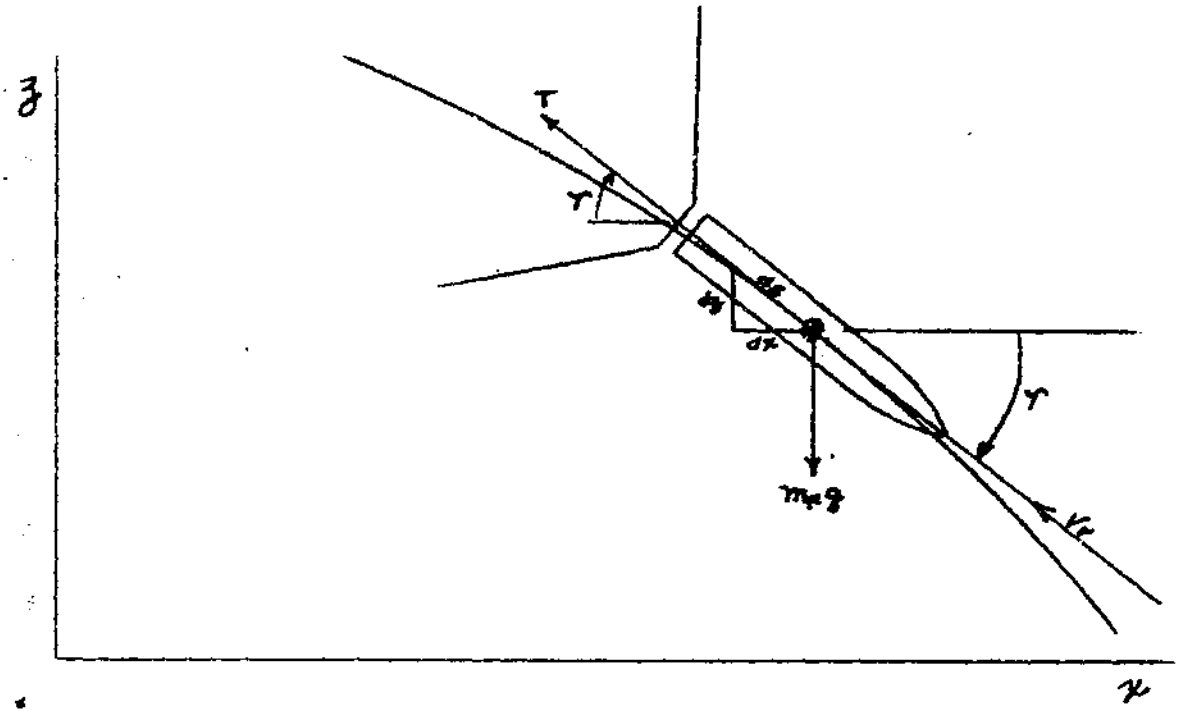


The equations of motion for the system were written in terms of these coordinates. Equating the forces in the $x$ and $z$ directions gives the following expressions:

$$m_R \ddot{x} = -T \cos \gamma$$

and

$$m_R \ddot{z} = -m_R g + T \sin \gamma$$

where $m_R$ = the total mass of the system

$\ddot{x}$ = horizontal acceleration

$\ddot{z}$ = vertical acceleration

$g$ = acceleration due to gravity

$T$ = rotochute thrust

$\gamma$ = tangent to the flight path measured from the horizontal

The elemental distance along the flight path $ds$ can be related to its vertical and horizontal components by the flight path angle $\gamma$ so that

$$ds = \frac{dx}{\cos\gamma} = -\frac{dz}{\sin\gamma}$$

but $ds = V_v\,dt$

where $V_v$ = velocity along the flight path

and therefore

$$\cos\gamma = \frac{dx}{V_v\,dt} = \frac{\dot{x}}{V_v}$$

$$\sin\gamma = -\frac{dz}{V_v\,dt} = -\frac{\dot{z}}{V_v}$$

Substituting these relationships into the initial equations of motion gives

$$m_R\ddot{x} = -\frac{T\dot{x}}{V_v}$$

and

$$m_R\ddot{z} = -m_R g - \frac{T\dot{z}}{V_v}$$

[redacted]

These equations were solved by the Runge-Kutta method of numerical integration which can be made to yield a high degree of accuracy. The solution at each time interval produces a check which determines the maximum interval that can be used consistent with an acceptable degree of accuracy.

The thrust variation with velocity necessary for the solution of the equations of motion was determined by the methods outlined in the sections on rotor system performance. These methods determine the rotor drag coefficient as a function of the non-dimensional advance ratio $V_w/\Omega R$. The various rotor parameters that effect the drag coefficient have been previously discussed and their significance to the resulting performance noted. It was necessary therefore only to introduce the full scale rotochute characteristics into the methods of high speed and of low speed performance to develop the drag coefficient variation with advance ratio for the prototype configuration. As discussed in Section A, the prediction of the prototype performance was dependent on the consideration of the full scale Reynolds number in the low speed performance analysis. As shown in Figure E-1, the maximum rotor drag coefficient was calculated to be approximately 1.53. This is considerably greater than the experimental values determined in the model wind tunnel tests primarily because of the higher Reynolds number associated with the full scale configuration. In addition, the aerodynamically cleaner blade root and grip regions of the prototype have also contributed to the improvement in the maximum low speed drag coefficient. Figure E-1 represents the calculated full scale drag coefficient variation with the velocity tip speed ratio and was used in developing the rotochute trajectories presented in this section.



[redacted]

The remaining quantity necessary to complete the solution of the trajectory problem is the variation of rotor speed with velocity along the flight path. This can be determined from the combined analyses of the blade pitch angle for equilibrium autorotation at each advance ratio ($V_w/\Omega R$) and the dynamic response of the governor mechanism to the aerodynamic, the centrifugal and the spring moments existing at each blade angle and rotor speed. By careful matching of the governor characteristics to the rotor blade aerodynamic and mass characteristics, the rotor speed can be maintained with a minimum variation along the trajectory. The flexibility of the governor design makes it possible to realize the optimum rotor speed consistent with structural limitations from release to the attainment of terminal velocity.

For the purpose of the preliminary design of the prototype, it was considered desirable to determine the trajectory characteristics in relation to various design limit tip speeds corresponding to the "step" condition near terminal descent. The terminal descent velocity is defined as the velocity at which the thrust is equal to the gross weight. It is obtained as a function of the rotor drag coefficient and the rotor disc area by the relationship,

$$V = \sqrt{\frac{2\,W/A}{\rho\, C_{DR}}}$$

Each value of $C_{D_R}$ in Figure R-1 represents an equilibrium condition at a certain velocity-tip speed ratio. Thus to obtain the minimum terminal velocity, the maximum $C_{D_R}$ of 1.53 would be used and the corresponding advance ratio $V_w/\Omega R$ would be equal to 0.13. Substitution of this

drag coefficient into the above equation will give a terminal velocity for the prototype of 78 ft/sec. at a terminal tip speed of 78/.13 or 600 ft/sec. The experimental results of the wind tunnel investigations on model rotochutes have indicated that the peak drag coefficient occurs very near or at the stall boundary and that at velocities slightly above that for peak $C_{D_R}$ an abrupt decrease in rotor speed results from the decelerating torque produced by excessive blade stall. The stall boundary therefore defines the limiting rotor tip speed consistent with a specific terminal velocity. However, if a higher than minimum terminal velocity is allowed, the governor spring rate and preload can be increased with a resulting increase in rotor speed at the same velocity. The advance ratio will therefore be reduced with a consequent reduction in $C_{D_R}$. Under these conditions, operation is confined to that portion of the drag curve shown in Figure E-1 that is to the left of peak drag coefficient. At a terminal drag coefficient of 1.4, for instance, the terminal velocity of the prototype would be increased to 81.6 ft./sec. at a corresponding tip speed of 710 ft/sec. However, since this advance ratio is below that for the stall boundary, the tip speed can be expected to increase further with velocity at a rate similar to that for the high speed model rotochute up to a limiting tip speed of 750 ft/sec. as shown in Figure E-2. At this point the maximum $C_{D_R}$ is again reached but at a velocity of 97.5 ft/sec. instead of the previous value of 78 ft/sec. In order to determine the importance of the limiting tip speed on the developed trajectory, additional conditions were studied for terminal drag coefficients down to 1.20. Figure E-3 shows the terminal velocities and the tip speeds associated with these conditions.

The characteristics of the velocity-tip speed curves beyond the stall boundary were predicted utilizing the results of the wind tunnel tests of the model rotochutes. The results obtained with the high speed rotochute model, which most closely represented the final prototype configuration, were utilized to relate the estimated minimum tip speed encountered beyond stall to the limiting tip speed at the stall boundary. An increase in governor effectiveness with governor spring preload was experienced throughout the wind tunnel investigation. This was evident from the reduction in the slope of the curve of rotor speed versus velocity with each additional increment of preload. Combining this effect with the general increase in the level of the equilibrium rotor speed throughout the complete velocity range achieved with increased governor spring stiffness, it is reasonable to expect that for the final prototype design the minimum rotor tip speed relative to a particular limit tip speed condition will be in the order of that shown in Figure E-2.

Although during the final wind tunnel program an investigation was made of the higher tip speed conditions expected with the full scale rotochute, this could not be done beyond a Mach number of 0.7 because of limited tunnel power. In the trajectory calculations presented in this report an attempt was made to approximate the effects of compressibility on the rate of change of tip speed with velocity. The maximum tip Mach number reached under steady state conditions during this latter program was 0.86 at a tunnel Mach number of 0.65. Up to this point the rotor speed was increasing linearily with the velocity and blade tip compressibility, if present, had no apparent effect. Little is known about the effects of

compressibility at the large angles of attack experienced in rotochute operation at or near the release velocity. The airfoil drag divergence boundary was estimated to exist somewhat above the maximum blade tip Mach number achieved during the wind tunnel tests. For these analyses this boundary as shown in Figure E-2 is defined as the resultant velocity producing a tip Mach number of 0.9 with the tip speed and the advance velocity corrected for the relieving effect of rotor blade coning. For the calculation of the trajectories it was assumed that above a tip Mach number of 0.9, the rotor tip speed remained essentially constant due to the effects of blade section drag rise on the torque balance. This assumption represents a compromise between the increase in tip speed with velocity known to exist below the drag divergence Mach number and the limiting conditions of operating at a constant tip Mach number. Three basic trajectory calculations were made at different limiting tip speed conditions and are designated as Cases I, II, and III (Figure E-2). In addition, the significance of the blade tip compressibility assumption was studied by modifying Case I in two ways; first, by assuming that the maximum tip speed at the release velocity was the same as for Case III, and secondly, by assuming that compressibility had no effect on the tip speed and therefore that the limiting tip speed would be achieved at the release velocity. These conditions are denoted as Case IA and Case IB respectively.

The data presented in Figures E-1 and E-2 formed the basis for the development of the drag versus velocity relationship needed for the solution of the equations of motion. The results of these trajectory solutions are presented in Figures E-4 thru E-8. The velocity along the

flight path, the attitude angle from the vertical, the trajectory range and the time are all plotted in relation to the drop distance below the release altitude. It may be seen from these results that the trajectory range and the velocity along the flight path at a drop distance of [illegible] feet are well within the specified limits in each of the cases investigated. It may also be noted by comparison of Figures E-4, E-7 and E-8 that the variation in tip speed in the region where compressibility is likely to occur produced no significant change in the trajectory performance. The required attitude angle of the vehicle at the specified drop distance is more difficult to achieve and based on the results of this study appears to be the critical operating requirement for this application of the rotochute. Due to the dynamic stability characteristics predicted for the prototype, which are discussed in Section F, it is expected that the amplitude of any oscillations resulting from a disturbance during descent will be sufficiently small to allow the attitude angle to be represented by the angle between the tangent to the trajectory and the vertical. A comparison of the trajectory results for the several cases investigated in terms of the attitude angle at various drop distances clearly shows the importance of operating at the highest possible tip speeds from release to terminal descent. An increase in retarding force is realized throughout the trajectory as a result of the higher tip speed reducing the advance ratio at each velocity and thus increasing the rotor drag coefficient at that velocity. The advantage of operating in terminal descent at an advance ratio below that for maximum $C_{D_R}$ can be seen from the increased tip speed possible at the stall boundary as shown in Figure E-2, and thus at all higher velocities along

the flight path. Since in general the stall boundary coincides with the point of maximum rotor drag coefficient, the higher the tip speed at stall, the larger will be the velocity at which the maximum $C_{D_R}$ is obtained. This will result in a considerably higher retarding force at a time in the trajectory when it can be most beneficial in changing the attitude angle. For example, if the maximum drag coefficient of 1.53 is set to occur in terminal descent, the terminal velocity will be 78 ft/sec. However, if the governor is adjusted to give operation at terminal descent below the stall boundary at a $C_{D_R}$ = 1.2 then the velocity at the point of maximum $C_{D_R}$ will be 118 ft/sec. and the resulting drag for the same $C_{D_R(max)}$ will have increased by a factor of 2.3.

In order to show more directly the significance of the design limit tip speed in relation to the attitude angle along the trajectory at various drop distances below the release altitude, the results of the trajectory analyses were plotted in the form shown in Figure E-9. It can be seen that for the prototype rotor configuration a limit tip speed of 950 ft/sec. is required to achieve an attitude angle of 40 degrees within 200 ft. from the release altitude. The slope of the 40 degree attitude angle curve in this region is rather gradual and with an allowable increase in drop distance of 40 feet the limit rotor tip speed would be reduced to 825 ft/sec. This tip speed condition also corresponds to a 50 degree attitude angle at 200 feet drop distance. The significance of this change in tip speed is apparent when it is considered that it represents approximately a 25 percent reduction in centrifugal force. The centrifugal loading is a primary factor in establishing the quantity of structural material necessary to show satis-

factory structural margins. Thus it influences the gross weight in relation to its affect on the weight of the rotating components. An estimation was made of the variation in gross weight with design limit tip speed. The results are presented in Figure E-10 and show that at the design limit tip speed of 950 ft/sec. corresponding to a 40 degree attitude angle at 200 feet drop distance, the gross weight is 2910 lbs. with a 2000 lb. payload. Since the trajectories are calculated with an assumed 3000 lb. gross weight, the results are valid for a vehicle with a 2090 lb. payload.

## F. STABILITY ANALYSIS

### Theory

The stability analysis is based on classical stability methods in which incremental perturbations from the equilibrium are considered. Perturbations in forward flight velocity can be shown to have no direct effect on the rotochute stability, eliminating that degree of freedom. Further, the assumption of a blade flapping synchroniser precludes independent blade flapping. The thrust vector thus passes through the rotochute center of gravity at all times. The equations of motion are written for four degrees of freedom; translation along the x and y axes and rotation about these axes. The coordinate system used and the positive directions of motions, forces, and moments is shown in the sketch below.

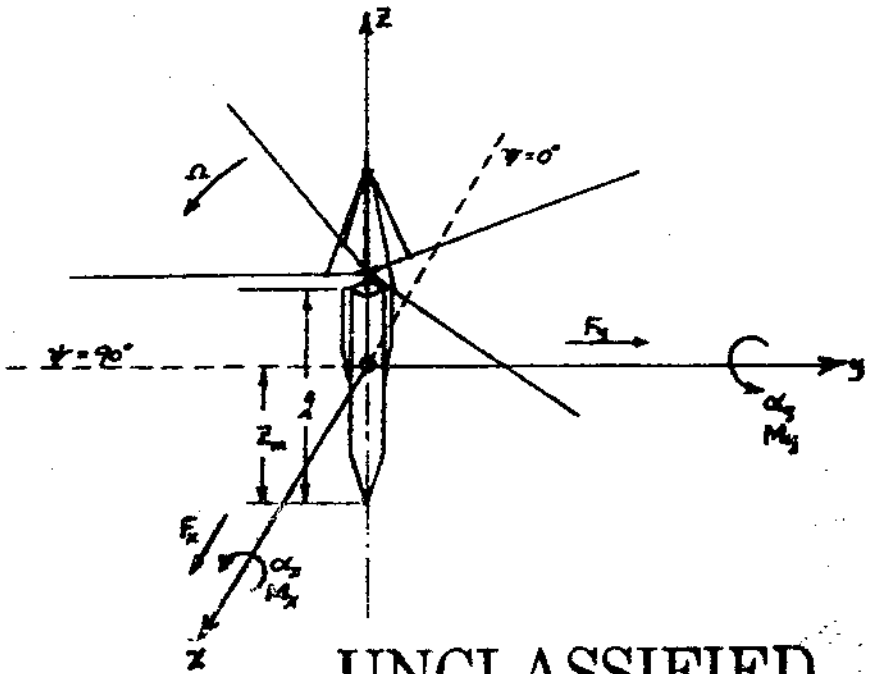

The coordinate system is assumed to descend with the rotochute. For translation of the rotochute and rotation about its center of gravity the equations of motion can be written

$$
\begin{aligned}
m_R\ddot{x} - F_x - f_x &= 0 \\
m_R\ddot{y} - F_y - f_y &= 0 \\
I\ddot{\alpha}_x - M_x - m_x &= 0 \\
I\ddot{\alpha}_y - M_y - m_y &= 0
\end{aligned}
\qquad \text{(F-1)}
$$

where

$$
\begin{aligned}
F_x &= \dot{x}(F_x)_{\dot{x}} + \dot{y}(F_x)_{\dot{y}} + \dot{\alpha}_x(F_x)_{\dot{\alpha}_x} + \dot{\alpha}_y(F_x)_{\dot{\alpha}_y} + \alpha_x(F_x)_{\alpha_x} + \alpha_y(F_x)_{\alpha_y} \\
f_x &= \dot{x}(f_x)_{\dot{x}} + \dot{\alpha}_y(f_x)_{\dot{\alpha}_y} + \alpha_y(f_x)_{\alpha_y} \\
F_y &= \dot{x}(F_y)_{\dot{x}} + \dot{y}(F_y)_{\dot{y}} + \dot{\alpha}_x(F_y)_{\dot{\alpha}_x} + \dot{\alpha}_y(F_y)_{\dot{\alpha}_y} + \alpha_x(F_y)_{\alpha_x} + \alpha_y(F_y)_{\alpha_y} \\
f_y &= \dot{y}(f_y)_{\dot{y}} + \dot{\alpha}_x(f_y)_{\dot{\alpha}_x} + \alpha_x(f_y)_{\alpha_x} \qquad \text{(F-2)} \\
M_x &= \dot{x}(M_x)_{\dot{x}} + \dot{y}(M_x)_{\dot{y}} + \dot{\alpha}_x(M_x)_{\dot{\alpha}_x} + \dot{\alpha}_y\left[(M_x)_{\dot{\alpha}_y} - I_z\Omega\right] + \alpha_x(M_x)_{\alpha_x} + \alpha_y(M_x)_{\alpha_y} \\
m_x &= \dot{y}(m_x)_{\dot{y}} + \dot{\alpha}_x(m_x)_{\dot{\alpha}_x} + \alpha_x(m_x)_{\alpha_x} \\
M_y &= \dot{x}(M_y)_{\dot{x}} + \dot{y}(M_y)_{\dot{y}} + \dot{\alpha}_x\left[(M_y)_{\dot{\alpha}_x} + I_z\Omega\right] + \dot{\alpha}_y(M_y)_{\dot{\alpha}_y} + \alpha_x(M_y)_{\alpha_x} + \alpha_y(M_y)_{\alpha_y} \\
m_y &= \dot{x}(m_y)_{\dot{x}} + \dot{\alpha}_y(m_y)_{\dot{\alpha}_y} + \alpha_y(m_y)_{\alpha_y}
\end{aligned}
$$

Since the rotochute and force system is symmetrical it follows that for the force and moment derivatives in general

$$(G_x)_{\Delta_x} = (G_y)_{\Delta_y}$$
$$(G_x)_{\Delta_y} = -(G_y)_{\Delta_x} \qquad \text{(F-3)}$$

Thus only one set of derivatives, say with respect to the x-axis, need be found.

Rotor Derivatives

In determining the rotor derivatives the rotor speed is assumed large compared to oscillation frequency; the force and moment derivatives can thus be taken as the average for one revolution of the rotor. Expressions for the derivatives are readily found by use of a quasi-steady approach in which the uncoupled motions of the rotochute are considered separately. In general, with the rotochute in a straight flight attitude such as would be encountered for uncoupled motions $\dot{x}$, $\dot{y}$, $\dot{\alpha}_x$, and $\dot{\alpha}_y$, the aerodynamic forces and moments take the form

$$F_x = \frac{1}{2\pi}\int_0^{2\pi}\int_e^R \Big\{\big[dL\cos(\phi+\Delta\phi) + dD\sin(\phi+\Delta\phi)\big]\sin\beta\cos\psi + \big[dL\sin(\phi+\Delta\phi) - dD\cos(\phi+\Delta\phi)\big]\sin\psi\Big\}\,d\psi$$

$$F_y = \frac{1}{2\pi}\int_0^{2\pi}\int_e^R \Big\{\big[dL\cos(\phi+\Delta\phi) + dD\sin(\phi+\Delta\phi)\big]\sin\beta\sin\psi - \big[dL\sin(\phi+\Delta\phi) - dD\cos(\phi+\Delta\phi)\big]\cos\psi\Big\}\,d\psi \qquad \text{(F-4)}$$

$$M_x = -\frac{1}{2\pi}\int_0^{2\pi}\int_e^R \Big\{\big[H\sin\beta + e\cos\beta + k(r-e)\big]\big[dL\cos(\phi+\Delta\phi) + dD\sin(\phi+\Delta\phi)\big]\sin\psi$$

$$-\big[H+(r-e)\sin\beta\big]\big[dL\sin(\phi+\Delta\phi) - dD\cos(\phi+\Delta\phi)\big]\cos\psi\Big\}\,d\psi \qquad \text{(F-4)}$$

$$M_y = \frac{1}{2\pi}\int_0^{2\pi}\int_e^R \Big\{\big[H\sin\beta + e\cos\beta + k(r-e)\big]\big[dL\cos(\phi+\Delta\phi) + dD\sin(\phi+\Delta\phi)\big]\cos\psi$$

$$+\big[H+(r-e)\sin\beta\big]\big[dL\sin(\phi+\Delta\phi) - dD\cos(\phi+\Delta\phi)\big]\sin\psi\Big\}\,d\psi$$

where hub drag is neglected throughout the analysis. For flight with angular displacement about the x-axis, the x-components of force and moment are unaltered from the above expressions; the y-components of force and moment must be written to conform to a yawed position relative to the coordinate system. Thus the force becomes

$$\bar{F}_y = \frac{1}{2\pi}\cos\alpha_x\int_0^{2\pi}\int_e^R \Big\{\big[dL\cos(\phi+\Delta\phi) + dD\sin(\phi+\Delta\phi)\big]\sin\beta\sin\psi$$

$$-\big[dL\sin(\phi+\Delta\phi) - dD\cos(\phi+\Delta\phi)\big]\cos\psi\Big\}\,d\psi \qquad \text{(F-4a)}$$

$$-\frac{1}{2\pi}\sin\alpha_x\int_0^{2\pi}\int_e^R \big[dL\cos(\phi+\Delta\phi) + dD\sin(\phi+\Delta\phi)\big]\cos\beta\,d\psi$$

where the last integral expression is the quasi-steady thrust component. The moment becomes,

$$M_y = \frac{1}{2\pi}\cos\alpha_x \int_0^{2\pi}\int_e^R \Big\{\big[H\sin\beta + \dot{e}\cos\beta + k(r-e)\big]\big[dL\cos(\phi+\Delta\phi) + dD\sin(\phi+\Delta\phi)\big]\cos\psi$$

$$+\big[H+(r-e)\sin\beta\big]\big[dL\sin(\phi+\Delta\phi) - dD\cos(\phi+\Delta\phi)\big]\sin\psi\Big\}\,d\psi \qquad (\text{V-4b})$$

$$-\frac{1}{2\pi}\sin\alpha_x \int_0^{2\pi}\int_e^R \big[e+(r-e)\cos\beta\big]\big[dL\sin(\phi+\Delta\phi) - dD\cos(\phi+\Delta\phi)\big]\sin^2\psi\,d\psi$$

where the steady portion of the last integral must be identically zero to satisfy the condition of zero net torque for quasi-steady motion.

The coefficient $k$, which appears in the moment integrals, is a rotor rigidity factor which governs the effective moment of the blade incremental aerodynamic forces about the rotochute center of gravity. When $k = 1.0$ the rotor is assumed rigid and the aerodynamic moment is transferred undiminished by the synchronizer linkage. When $0<k<1.0$ the rotor is flexible and aeroelastic effects reduce the aerodynamic moment transferred through the synchronizer linkage. The rotor rigidity is a significant factor in determining rotochute stability and is treated separately in Appendix IV.

The lift and drag forces per unit span can be written,

$$dL = \frac{\pi}{2}\rho R\sigma(c_l + \Delta c_l)(V + \Delta V)^2 dr$$

$$dD = \frac{\pi}{2}\rho R\sigma(c_d + \Delta c_d)(V + \Delta V)^2 dr$$

where

$$\Delta c_l = \Delta\alpha\, c_{l_\alpha}$$

$$\Delta c_d = \Delta\alpha\, c_{d_\alpha}$$

$$\Delta\alpha = \Delta\phi = \Delta\left(\tan^{-1}\frac{U_p}{U_T}\right)$$

$$= \frac{U_T(\Delta U_p) - U_p(\Delta U_T)}{U_p^2 + U_T^2}$$

$$V + \Delta V = \sqrt{(U_p + \Delta U_p)^2 + (U_T + \Delta U_T)^2}$$

and since $\Delta\phi$ is considered small,

$$\cos(\phi + \Delta\phi) = \cos\phi - \Delta\phi\sin\phi$$

$$= \frac{U_T}{\sqrt{U_p^2 + U_T^2}} - \frac{U_p\left[U_T(\Delta U_p) - U_p(\Delta U_T)\right]}{(U_p^2 + U_T^2)^{3/2}}$$

$$\sin(\phi + \Delta\phi) = \sin\phi + \Delta\phi\cos\phi$$

$$= \frac{U_p}{\sqrt{U_p^2 + U_T^2}} - \frac{U_T\left[U_T(\Delta U_p) - U_p(\Delta U_T)\right]}{(U_p^2 + U_T^2)^{3/2}}$$

Hence, with non-linear velocity increments assumed negligible and with the use of non-dimensional terminology, the force per unit span normal to the path of rotation and to the blade span axis becomes

$$dL\cos(\phi+\Delta\phi)+dD\sin(\phi+\Delta\phi)=\left\{\frac{dT}{\cos\beta}+\frac{1}{2}\pi\rho\sigma\Omega R^3\left[\bar{C}_1(\Delta U_P)+\bar{C}_2(\Delta U_T)\right]\right\}d\bar{r} \qquad (F\text{-}5)$$

and the force per unit span tangent to the path of rotation and normal to the blade span axis becomes

$$dL\sin(\phi+\Delta\phi)-dD\cos(\phi+\Delta\phi)=\left\{dQ'+\frac{1}{2}\pi\rho\sigma\Omega R^3\left[\bar{C}_3(\Delta U_P)+\bar{C}_4(\Delta U_T)\right]\right\}d\bar{r} \qquad (F\text{-}6)$$

where

$$\bar{C}_1=\frac{\Omega R}{V}\Big\{\left[\xi+(\bar{r}-\xi)\cos\beta\right]^2(c_{l_\alpha}+c_d)+2\lambda^2\cos^2\beta\cdot c_d$$
$$+\lambda\cos\beta\left[\xi+(\bar{r}-\xi)\cos\beta\right](c_l+c_{d_\alpha})\Big\}$$

$$\bar{C}_2=\frac{\Omega R}{V}\Big\{2\left[\xi+(\bar{r}-\xi)\cos\beta\right]^2c_l+\lambda^2\cos^2\beta\cdot(c_l-c_{d_\alpha})$$
$$+\lambda\cos\beta\left[\xi+(\bar{r}-\xi)\cos\beta\right](c_d-c_{l_\alpha})\Big\} \qquad (F\text{-}7)$$

$$\bar{C}_3=\frac{\Omega R}{V}\Big\{\left[\xi+(\bar{r}-\xi)\cos\beta\right]^2(c_l-c_{d_\alpha})+2\lambda^2\cos^2\beta\cdot c_l$$
$$+\lambda\cos\beta\left[\xi+(\bar{r}-\xi)\cos\beta\right](c_{l_\alpha}-c_d)\Big\}$$

$$\bar{C}_4=\frac{\Omega R}{V}\Big\{-2\left[\xi+(\bar{r}-\xi)\cos\beta\right]^2c_d-\lambda^2\cos^2\beta\cdot(c_{l_\alpha}+c_d)$$
$$+\lambda\cos\beta\left[\xi+(\bar{r}-\xi)\cos\beta\right](c_l+c_{d_\alpha})\Big\}$$

$$\frac{V}{\Omega R} = \sqrt{\lambda^2 \cos^2\beta + \left[\xi + (\bar{r} - \xi)\cos\beta\right]^2}$$

The position of the rotochute center of gravity in the x, y plane does not contribute to the aerodynamic derivatives. The velocity increments for the perturbations from equilibrium which need be considered can thus be written:

(1) For motion along the x-axis

$$\Delta U_p = -\dot{x}\sin\beta\cos\psi$$

$$\Delta U_T = \dot{x}\sin\psi$$

(2) For rotational velocity about the x-axis

$$\Delta U_p = \dot{\alpha}_x R\left[\eta\sin\beta - \xi(1-\cos\beta) + \bar{r}\right]\sin\psi$$

$$\Delta U_T = \dot{\alpha}_x R\left[\eta - \xi\sin\beta + \bar{r}\sin\beta\right]\cos\psi$$

(3) For angular displacement about the x-axis

$$\Delta U_p = \lambda_J \Omega R \tan\alpha_x \sin\beta \sin\psi$$

$$\Delta U_T = \lambda_J \Omega R \tan\alpha_x \cos\psi$$

The incremental perturbation velocities and displacements are considered small, hence non-linear terms will be assumed negligible. After substituting the unit span forces Eq's.(F-5) and (F-6) into the integral expressions for force and moment (Eq. (F-4)), integrating with respect to

$\psi$ , and taking the partial derivative within the remaining integral, the force and moment derivatives can be written

$$(F_x)_{\dot{x}} = -\frac{\pi}{4}\rho\sigma\Omega R^3\int_{\xi}^{1}(\bar{c}_1\sin^2\beta - \bar{c}_4)\,d\bar{r}$$

$$(F_y)_{\dot{x}} = \frac{\pi}{4}\rho\sigma\Omega R^3\sin\beta\int_{\xi}^{1}(\bar{c}_2 + \bar{c}_3)\,d\bar{r}$$

$$(F_x)_{\alpha_x} = \frac{\pi}{4}\rho\sigma\Omega R^4\int_{\xi}^{1}\Big\{\bar{c}_2\sin\beta(\eta - \xi\sin\beta + \bar{r}) + \bar{c}_3\left[\eta\sin\beta - \xi(1-\cos\beta) + \bar{r}\right]\Big\}\,d\bar{r} \qquad \text{(V-8)}$$

$$(F_y)_{\alpha_y} = \frac{\pi}{4}\rho\sigma\Omega R^4\int_{\xi}^{1}\Big\{\bar{c}_1\sin\beta\left[\eta\sin\beta - \xi(1-\cos\beta) + \bar{r}\right] - \bar{c}_4(\eta - \xi\sin\beta + \bar{r}\sin\beta)\Big\}\,d\bar{r}$$

$$(F_x)_{\alpha_x} = \lambda_s\Omega R(F_y)_{\dot{x}}$$

$$(F_y)_{\alpha_x} = -\lambda_d\Omega R(F_x)_{\dot{x}} - T$$

$$(M_x)_{\dot{\chi}} = -\frac{\pi}{4}\rho\sigma\Omega R^4\int_{\xi}^{1}\Big\{\bar{C}_2\big[\eta\sin\beta + \xi\cos\beta + k(\bar{r}-\xi)\big] + \bar{C}_3\sin\beta(\eta - \xi\sin\beta + \bar{r}\sin\beta)\Big\}d\bar{r}$$

$$(M_y)_{\dot{\chi}} = -\frac{\pi}{4}\rho\sigma\Omega R^4\int_{\xi}^{1}\Big\{\bar{C}_1\sin\beta\big[\eta\sin\beta + \xi\cos\beta + k(\bar{r}-\xi)\big] - \bar{C}_4(\eta - \xi\sin\beta + \bar{r}\sin\beta)\Big\}d\bar{r}$$

(7-8)

$$(M_x)_{\dot{\alpha}_x} = -\frac{\pi}{4}\rho\sigma\Omega R^5\int_{\xi}^{1}\Big\{\bar{C}_1\big[(\eta\sin\beta + \xi\cos\beta)^2 + (\bar{r}-\xi)(1+k)(\eta\sin\beta + \xi\cos\beta) + k(\bar{r}-\xi)^2\big] - \bar{C}_4(\eta - \xi\sin\beta + \bar{r}\sin\beta)^2\Big\}d\bar{r}$$

$$(M_y)_{\dot{\alpha}_x} = \frac{\pi}{4}\rho\sigma\Omega R^5\int_{\xi}^{1}\Big\{\bar{C}_2\big[(\eta\sin\beta + \xi\cos\beta)(\eta - \xi\sin\beta + \bar{r}\sin\beta) + k(\bar{r}-\xi)(\eta - \xi\sin\beta + \bar{r}\sin\beta)\big] + \bar{C}_3(\eta - \xi\sin\beta + \bar{r}\sin\beta)(\eta\sin\beta + \xi\cos\beta + \bar{r} - \xi)\Big\}d\bar{r}$$

$$(M_x)_{\alpha_x} = \lambda_d\Omega R(M_y)_{\dot{\chi}}$$

$$(M_y)_{\alpha_x} = -\lambda_d\Omega R(M_x)_{\dot{\chi}}$$

It should be noted that the assumption of small cone angle $\beta$, results in the coefficients $\bar{C}_i$ being independent of $\beta$. This assumption appreciably reduces the calculations required in determining the derivatives and is valid in the range of interest.

Body Derivatives

Slender-body potential theory, references (16) and (17) was utilized for the purpose of determining the derivatives for the body without fins. The test results given in reference (17) indicate that neglecting the non-linear, slender-body, viscous flow terms results in little loss in accuracy for small angles of attack. The lift and the moment about the rotochute center of gravity for the body without fins can be written approximately as

$$L_B = \rho V_v^2 \int_0^l (K_2 - K_1) \frac{dS}{dz} \alpha \, dz$$

$$M_B = \rho V_v^2 \int_0^l (z_m - z)(K_2 - K_1) \frac{dS}{dz} \alpha \, dz \qquad \text{(F-9)}$$

Determination of the aerodynamic forces due to the fins, including the induced effect of the body, was adapted from reference (18). The fins are essentially thin, flat-plate wings hence a section lift curve slope of $2\pi$ is assumed; the aspect ratio correction is included in the lift and moment

expressions. Since a cruciform fin arrangement is used it can be assumed that one set of fins is always aerodynamically effective. The lift of the fins and the moment about the body center of gravity due to the fins, including the induced effect of the body on the fins, can be written

$$L_w = \frac{\frac{\pi}{2}\rho V_\infty^2 (\bar{B}-\bar{D})^2 \left(1+\frac{\bar{D}}{\bar{B}}\right)\alpha}{1+\sqrt{1+\left(\frac{A_s}{2}\right)^2(1-M_0^2)}} \tag{F-10}$$

$$M_w = \frac{\frac{\pi}{2}\rho V_\infty^2 (\bar{B}-\bar{D})^2 \left(1+\frac{\bar{D}}{\bar{B}}\right)\alpha}{1+\sqrt{1+\left(\frac{A_s}{2}\right)^2(1-M_0^2)}} (z_m - z_p)$$

The body lift induced by the presence of the flow field about the fins can be approximated as

$$L_{B_{ind}} = L_w K_3 \tag{F-11}$$

where $K_3$ as a function of $\bar{D}/\bar{B}$ is given in reference (18). The center of pressure of the induced body lift is assumed to coincide with the center of pressure of the fins.

The expressions for the total body lift and the total body moment, including fins, about the rotochute center of gravity can now be written

$$f = \rho V_v^2 \left\{ \int_0^1 (K_2 - K_1) \frac{dS}{dz} \alpha \, dz + \frac{\frac{\pi}{2}(\bar{B} - \bar{D})^2 \left(1 + \frac{\bar{D}}{\bar{B}}\right) \alpha}{1 + \sqrt{1 + \left(\frac{A_s}{2}\right)^2 (1 - M_o^2)}} (1 + K_3) \right\}$$

(F-12)

$$m = \rho V_v^2 \left\{ \int_0^1 (z_m - z)(K_2 - K_1) \frac{dS}{dz} \alpha \, dz + \frac{\frac{\pi}{2}(\bar{B} - \bar{D})^2 \left(1 + \frac{\bar{D}}{\bar{B}}\right) \alpha}{1 + \sqrt{1 + \left(\frac{A_s}{2}\right)^2 (1 - M_o^2)}} (z_m - z_p)(1 + K_3) \right\}$$

The angle of attack in the above expressions is determined by the disturbance of the rotochute body from the equilibrium. For the three perturbations previously considered the angle of attack can be written as follows:

(1) For motion along the x-axis

$$\alpha = -\frac{\dot{x}}{V_v}$$

(2) For rotational velocity about the x-axis

$$\alpha = (z - z_m) \frac{\dot{\alpha}_x}{V_v}$$

(3) For angular displacement about the x-axis

$$\alpha = \alpha_x$$

The angle of attack is considered small for each of the rotochute perturbations. The lift thus becomes the force in the x or y-direction; the moment about the rotochute center of gravity becomes the moment about the x or y axis. Substitution into Eq. (F-12) of the appropriate angle of attack in terms of the perturbation, integration over the body length, and subsequent partial differentiation leads to the force and moment derivatives for the rotochute body. Then

$$(f_x)_{\dot{x}} = -\rho V_v \left\{ S_B + \frac{\frac{\pi}{2}(\bar{B}-\bar{D})^2\left(1+\frac{\bar{D}}{\bar{B}}\right)}{1+\sqrt{1+\left(\frac{A_R}{2}\right)^2(1-M_o^2)}}(1+K_s) \right\}$$

$$(f_y)_{\dot{\alpha}_x} = \rho V_v \left\{ S_B(1-z_m) - V_B + \frac{\frac{\pi}{2}(\bar{B}-\bar{D})^2\left(1+\frac{\bar{D}}{\bar{B}}\right)}{1+\sqrt{1+\left(\frac{A_R}{2}\right)^2(1-M_o^2)}}(z_p-z_m)(1+K_s) \right\} \qquad \text{(F-13)}$$

$$(f_y)_{\alpha_x} = -V_v (f_x)_{\dot{x}}$$

$$(m_y)_{\dot{x}} = \rho V_v \left\{ V_B - S_B(1-z_m) + \frac{\frac{\pi}{2}(\bar{B}-\bar{D})^2\left(1+\frac{\bar{D}}{\bar{B}}\right)}{1+\sqrt{1+\left(\frac{A_R}{2}\right)^2(1-M_o^2)}}(z_p-z_m)(1+K_s) \right\}$$

$$(m_z)_{\dot{\alpha}_y} = \rho V_y \Big\{ 2M_y - S_B(z_m^2 + l^2) + 2z_m(lS_B - V_B)$$

$$- \frac{\frac{\pi}{2}(\bar{b}-3)^2\left(1+\frac{\bar{b}}{8}\right)}{1+\sqrt{1+\left(\frac{A_R}{2}\right)^2(1-M_0^2)}}(z_p - z_m)^2(1+K_3)\Big\} \qquad \text{(7-23)}$$

$$(m_z)_{\alpha_x} = V_y (m_y)_{\dot{\alpha}_x}$$

where $(K_2 - K_1)$ is assumed equal to unity for bodies of high fineness ratio. The derivatives thus found are applicable to the rotochute body whether or not the rotor is operative.

Solution of the Equations of Motion

Substitution of Eq's (F-2) into Eq's (F-1) leads to a set of linear, second order, simultaneous differential equations. The harmonic solutions

$$x = x_0 e^{pt}$$
$$y = y_0 e^{pt}$$
$$\alpha_x = \alpha_{x_0} e^{pt}$$
$$\alpha_y = \alpha_{y_0} e^{pt}$$

where $p$ is complex $(p = -\omega\zeta \pm i\omega\sqrt{1-\zeta^2})$ lead to a set of simultaneous, linear, algebraic equations in $x$, $y$, $\alpha_x$, and $\alpha_y$. For solutions, other than the trivial case where no motion is possible, the determinant of the coefficients must be equal to zero. Since the motions indicated by the equations are symmetrical with respect to both $x$ and $y$ and $\alpha_x$ and $\alpha_y$ the four by four determinant can be more simply expressed as the product of a complex two by two determinant and its complex conjugate. Thus, the characteristic equation is obtained by taking the square of the modulus of one of the complex determinants. The resulting equation is of the form

$$p^6 + A_5 p^5 + A_4 p^4 + A_3 p^3 + A_2 p^2 + A_1 p + A_0 = 0$$

being of 6th degree rather than 8th degree because the position $x, y$ of the rotochute center of gravity does not contribute to the forces acting on the rotochute. Solution of the 6th degree equation can be achieved by any of several well known methods. The six characteristic roots define the motion of the rotochute. When it is desirable to study the variation of

several rotochute parameters or operating conditions, as in the present study, solution of the equations of motion is most readily achieved by the direct approach of electrical analogy.

Calculations

The equations of motion and the stability derivatives are written in a generalized form which makes the analysis applicable to any portion of the flight trajectory. Flight test experience with various rotochute configurations has indicated that the stability of the vehicle is most critical at initial release, prior to the start of rotation, and at the terminal descent condition. Thus, with the rotor operating, it appears that the stability analysis need only be concerned with the terminal descent condition.

The force and moment derivatives can be found by summation over a finite number of radial strips using the net inflow, lift, and drag distributions prepared for the performance calculations. The lift curve and drag curve slopes are then taken to be the slopes at the mid-point of each radial blade segment. The rotational speed of the rotor is determined, for a given inflow distribution, as that speed which is necessary to provide thrust, as a function of cone angle, equal to gross weight. This method of obtaining the force and moment derivatives appears to be the only practical method of coping with the high degree of stall encountered in practical rotochutes. It appears that the artifice of assuming uniform inflow and linear lift curve slope would result in spurious stability derivatives for the semi-stalled airfoil condition. The body derivatives are calculated in a straightforward manner as outlined in the section devoted to that purpose. For terminal descent it is evident that the square of the Mach number is negligibly small compared to unity. In general, as the rotor cone angle is decreased the body has increased influence on the stability of the vehicle at

terminal descent.

The stability of the vehicle at initial release requires primarily that it possess a slight margin of static stability. The static stability depends to a considerable extent, however, on the effective area of the base of the body; a blunt base tends to increase stability and a base resulting from a diffusing rearward contour tends to decrease stability. At high flight speeds it appears probable that the flow will follow the surface of only the most gentle diffusing contour. In general the effective base area will be greater than the geometric base area as a result of flow separation. It appears that wind tunnel tests might be necessary to determine a realistic effective base area for a given diffusing contour. An alternative which will always give conservative results is to assume the effective base area equal to the geometric base area (i.e., as in purely potential flow) and then determine the fin area aft of the vehicle center of gravity which will provide marginal static stability.

Analytical Investigation

Analytical stability investigations were conducted for both the prototype rotochute and a rotochute presently being flight tested by The Kaman Aircraft Corporation (designated the M2 rotochute). The geometric, mass, and inertia properties of the two rotochutes are given in Table F-4; the operating conditions which were investigated are given in Table F-5.

Solution of the equations of motion was achieved by the use of a GPS electrical analog computer. The solution for one operating condition was also obtained by hand calculation in order to substantiate the analog results. An example of the solutions obtained is shown in Figure F-1 for one operating condition with a systematic variation of the rotor rigidity factor.

Analytical investigation of the M2 rotochute stability was undertaken only as a means of substantiating the proposed analysis method by use of the qualitative experimental data available for that vehicle. A further attempt to substantiate the analytical method was to have been by comparison of analytically and experimentally determined rotor static yaw derivatives. The experimental work was performed in the UAC 8 foot diameter wind tunnel; inadequacy of the balance system for the conditions imposed, however, resulted in side forces and moments of questionable quantitative accuracy.

Initial attempts to predict the stability of the M2 rotochute involved the calculation of derivatives for an assumed rigid rotor. The method predicted a reasonable margin of stability for operating conditions which, in fact, could not be obtained experimentally due to extremely divergent spiral oscillations. Subsequent study of the derivatives having

[redacted]

a significant effect on the rotochute stability indicated the deleterious nature of aeroelastic effects. The rotor rigidity factor was then included in the stability derivatives. In Figure F-2 the damping of the spiral oscillations, resulting from an initial yaw condition, is given as a function of the rotor rigidity factor. The damping is shown as the percent of critical damping (i.e., for which no oscillation is possible regardless of initial deflection); stability is associated with positive damping. The significance of the rotor rigidity factor on the rotochute stability is readily apparent. It is interesting to note that comparison of analytical stability results and experimental stability observations, including the oscillation frequency in each case, indicates that the rotor rigidity factor of the M2 rotochute is approximately $k = .44$. The trends shown in Figure F-2 indicate further that there is a significant dependence of stability on the advance ratio, $\lambda_d$ ; increased advance ratio corresponds to increased stability. The qualitative dependence of stability on advance ratio has been observed for a large number of test flights with various rotochute configurations and tends to confirm the trend indicated by the analytical results. The analytical methods outlined in the section on stability theory appear to give a reliable estimate of the rotochute stability as compared with experimental observations.

The principle results of the stability investigation conducted on the prototype rotochute are also shown in Figure F-2. Comparison with the results for the M2 rotochute indicates that the rotor rigidity factor affects the prototype rotochute in a very similar manner. This rotochute is seen to possess a good margin of stability, however, for the range of rigidity factors



[redacted]

investigated. The physical parameters and operating conditions of the two rotochutes are such that the difference in stability levels cannot be attributed to specific design parameters in so complex a relationship. The high degree of dependence of rotochute stability on certain derivatives does permit some insight into the establishment of some important physical parameters of the system.

The influence of the rotor inertia on the spiral oscillation damping is shown in Figure F-3. This parameter affects the gyroscopic moment which tends to dynamically couple rotations about the x and y axes. It appears that reducing rotor inertia is in general advantageous to rotochute stability. However, for design purposes a balance between rotor rigidity and rotor inertia must evidently be maintained. It is interesting to note that for large rotor inertia an oscillation associated with the gyroscopic nutation becomes rather suddenly predominant; this leads to a high frequency spiral instability which is superimposed on the aerodynamic oscillations. The reduction of rotor inertia to zero resulted in increased damping for a rotor rigidity of $k = 1.0$. It was determined that damping above approximately 70 percent of critical damping could not be accurately measured on the oscilloscope used in conjunction with the analog computer. The reduction of rotor inertia to zero resulted in a sudden decrease in damping for a rotor rigidity of $k = .40$. Maximum damping for this configuration appeared to be at $I_R/I = .043$, but the actual damping value was too high for accurate determination. The spiral oscillation frequency increased consistently with decreasing rotor inertia.

The influence of five of the combined rotor and body stability derivatives on the spiral oscillation damping was very large compared to

the influence of the remaining seven derivatives. The effect of varying these derivatives separately is shown in Figure F-4. The influence of the combined aerodynamic damping moment derivative, $(\bar{M}_x)_{\dot{\alpha}_x}$, shows a trend which could be expected (Figure F-4a). Increasing this derivative to a value close to zero results in the predominance of the high frequency oscillations associated with gyroscopic nutation regardless of rotor rigidity. Decreasing the value of this derivative has a pronounced stabilizing effect on the rotochute.

The influence of the combined restoring moment derivative $(\bar{M}_x)_{\alpha_{x_0}}$ shows a trend which is of considerable importance to rotochute design (Figure F-4b). With the rotor assumed rigid, decreasing the derivative (increasing restoring moment) appears to increase stability at an increasing rate. It is shown that this trend does not continue for reduced rotor rigidity; the rate of stabilizing influence of the derivative decreases as the derivative decreases.

Recalling from Eq's. (F-8) and (F-13) that $(\bar{M}_y)_{\dot{x}} = \frac{1}{V_\varphi}(\bar{M}_x)_{\alpha_x}$ and noting the influence of the combined translational coupling moment derivative, $(\bar{M}_y)_{\dot{x}}$, (Figure F-4c), it is conceivably possible to design a rotochute which is dynamically unstable due to excessive static stability and low rotor rigidity. That is,,the coupling moment derivative shows a pronounced destabilizing trend with decreasing value and decreasing rotor rigidity. Since the proportionality factor between the two derivatives is the reciprocal of descent velocity it appears that increasing the descent velocity has a stabilizing effect. This trend appears to offer an explanation for the stabilizing trend of increased advance ratio indicated for the RR rotochute in Figure F-2.

The influence of the rotational coupling moment derivative, $(M_y)_{\alpha_x}$, is shown in Figure F-4d. A pronounced stabilising trend with increasing value of the derivative is indicated. The large degree of influence exhibited by this derivative is evidently partially responsible for the existence of spiral oscillations which do not involve gyroscopic nutation (i.e., when $I_z$ is assumed equal to zero).

The influence of the combined rotational coupling force derivative, $(\bar{F}_y)_{\alpha_x}$, is shown in Figure F-4e. This derivative is approximately equal to the thrust force acting on the rotochute and indicates that high load factors result in a destabilising trend of the derivative. Since high load factors occur only at high speeds, which in general favorably effect more influential derivatives, the net effect of increased load factor appears to be beneficial despite the trend shown for $(\bar{F}_y)_{\alpha_x}$.

The fact that the important derivatives were moment contributions in all but one instance is strong evidence that the rotation of the rotochute about its center of gravity is the principle motion of the system. The fundamental rotations about the x and y axes are coupled in a manner which produces the spiral motion observed in test drops and on the analog computer. The period of the predominant motion is shown in Figure F-5 to be a function of both rotor rigidity and cone angle. The trend indicated is that which would intuitively be expected; the oscillation period decreases as cone angle is increased and the oscillation period increases as the rotor rigidity is decreased.

The investigation has provided an insight into the problem of rotochute stability which permits the qualitative establishment of some of

the important physical parameters of the system. The rotor rigidity factor has been established as a significant system parameter. Although a high degree of rotor rigidity is shown to be beneficial to rotochute stability, it is shown that increased rotor inertia has an adverse affect on stability. It appears that a design balance between rotor rigidity and rotor inertia is necessary for a design of maximum stability. In general, it appears that the rotor rigidity factor will be considerably less than unity. Since the combined translational coupling moment derivative, $(\bar{M}_q)_{\dot{z}}$, is inversely proportional to the descent velocity, the design terminal descent velocity should be sufficiently high to prevent instability which would result from a large negative value of this derivative. In this respect it appears that excessive static stability is undesirable since $(\bar{M}_q)_{\dot{z}}$ is directly proportional to the combined restoring moment derivative, $(\bar{M}_q)_{\alpha_w}$. A conceivable method of reducing static stability, for rotochutes which have significant body stability derivatives, is to design the body configuration for a sufficiently high degree of static instability. The high density body configuration of the prototype rotochute, however, results in body stability derivatives which are rather insignificant compared to the rotor derivatives. The rotochute body, as suspended from the rotor, would be quite unstable if the rotor were replaced by an equal mass having equal inertia about the body center of gravity and incurring no aerodynamic forces. From Eq's (F-8) it appears that such a configuration would result if either $\sigma$ or $R$ (and to a certain extent $\Omega$ ) were vanishingly small. Inductive reasoning thus indicates that, with all other influencing parameters unchanged, increases in those parameters must have a stabilizing effect on the rotochute. A de-

tailed investigation would be necessary to determine quantitatively the influence of each parameter on retochute stability since any change must affect other significant parameters.

TABLE F-II

**Rotochute Operating Conditions**

**Used for Stability Investigation**

| Rotochute | $\lambda_d$ | $\theta$ (Degrees) | $\Omega$ (rad/sec) | $\beta$ (Degrees) | $C_{D_R}$ | Airfoil Section |
|---|---|---|---|---|---|---|
| Prototype | .12 | 2.85 | 57.21 | 5 | 1.522 | NACA 0012* |
| Prototype | .12 | 2.85 | 58.21 | 10 | 1.522 | NACA 0012* |
| Prototype | .12 | 2.85 | 59.92 | 15 | 1.522 | NACA 0012* |
| M2 | .168 | 3.175 | 59.6 | 10.75 | 1.0 | NACA 0012† |
| M2 | .220 | 2.60 | 51.99 | 12 | .767 | NACA 0012† |

* Lift and drag curves were corrected for compressibility effects.

† Incompressible flow was assumed throughout.

TABLE F-I

Rotochute Geometric, Mass, and Inertia Properties

Used for Stability Investigation

| Parameter | Prototype Rotochute | M2 Rotochute |
|---|---|---|
| R, ft | 10 | 7 |
| b | 4 | 2 |
| $\sigma$ | .139 | .106 |
| $\xi$ | .05833 | .08333 |
| $\eta$ | .37706 | .28571 |
| I, slug ft$^2$ | 507 | 208 |
| $I_{xx}$, slug ft$^2$ | 103.18 | 35 |
| $m_R$, slugs | 82 | 28 |
| $I_b$, slug ft$^2$ | 25.795 | 17.4 |
| P, slugs | 1.834 | 2.33 |
| $l$, ft | 8.46 | 13.6 * |
| $V_B$, ft$^3$ | 13.07 | - - -* |
| $V_v$, ft$^4$ | 62.00 | - - -* |
| $S_B$, ft$^2$ | 1.77 | 2.4 * |
| $z_m$, ft | 5.02 | 5.1 * |
| $z_p$, ft | 7.26 | 10.4 * |
| $S_p$, ft$^2$ | 1.083 | - - -* |
| B - D, ft | .857 | - - -* |

* Key configuration derivatives were determined from wind tunnel test data.

## G. EXPERIMENTAL PROGRAM

### DESCRIPTION OF MODELS, APPARATUS AND TESTS

**Models**

The models tested were all of 4 ft. diameter with the same basic governor linkage system. They differed in detail according to the purposes of the tests. The following table lists the basic model configurations.

TABLE G-I

Characteristics of Models Tested

| Model No. | Hub | Blades Number | Blades Chord | Blades Core | Blades Position | Governor Spring K | Taper Ratio |
|---|---|---|---|---|---|---|---|
| 1 | 2-P | 2 | 4" | Alum. | Normal | 1400 | 1.0 |
| 2 | 2-P | 2 | 4" | Alum. | Normal | 985 | 1.0 |
| 3 | 2-P | 2 | 6" | Wood | Normal | 985 | 1.0 |
| 4 | 4A | 4 | 4" | Steel | Normal | 750 | 1.0 |
| 5 | 4A | 2 | 4" | Steel | Normal | 750 | 1.0 |
| 6 | 4A | 2 | 6" | Wood | Normal | 750 | 1.0 |
| 7 | 4A | 2 | 6" | Wood | Normal | 250 | 1.0 |
| 8 | 4A | 2 | 6" | Wood | Aft | 250 | 1.0 |
| 9 | 4A | 4 | 6" | Wood | Normal | 750 | 1.0 |
| 10 | 2-P | 2 | 4" | Alum. | Normal | 1400 | 1.0 |
| 11 | 4A | 4 | 4" | Steel | Normal | 250 | 1.0 |
| 12 | 2-G | 2 | 4" | Alum. | Normal | 1400 | 1.0 |
| 13 | 4A | 4 | 4" | Steel | Forward | 750 | 1.0 |
| 14 | 4A | 4 | 4" | Weighted | Aft | 750 | 1.0 |

TABLE G-I (Continued)

| Nodal No. | Hub | Blades Number | Blades Chord | Blades Core | Blades Position | Governor Spring K | Taper Ratio |
|---|---|---|---|---|---|---|---|
| 15 | 4A | 4 | 4" | Weighted | Aft | 250 | 1.0 |
| 16 | 4A | 4 | 4" | Alum. | Normal | 750 | 1.0 |
| 17 | 4B | 4 | 4" | Steel | Normal | 750 | 1.0 |
| 18 | 4B | 4 | 4" | Steel | Normal | 750 | 1.0 |
| 19 | 4B | 4 | 4" | Alum. | Normal | 1000 | .644 |
| 20 | 4C | 4 | 2.3* | Wood | Normal | 1600 | .644 |
| 21 | 4C | 4 | 2.3* | Wood | Normal | 1600 | .644 |
| 22 | 4C | 4 | 2.3* | Wgt. TE Heavy | Normal | 1600 | .644 |
| 23 | 4A | 4 | 4" | Steel | Normal | 750 | 1.0 |
| 24 | 4A | 4 | 6" | Wood | Normal | 750 | 1.0 |
| 25 | 4A | 4 | 4" / | Wood | Normal | 750 | 1.0 |
| 26 | 4C | 4 | 2.3* | Wgt.TE Heavy | Normal | 2440 | .644 |
| 27 | 4C | 4 | 2.3 | Wood | Normal | 2440 | .644 |

Hub 4A has low underslung blade-grips

Hub 4B has high underslung blade-grips

Hub 4C has zero underslung blade-grips

Hub 2 is two-bladed hub with: - P pressure measuring configuration
- G strain gage measuring configuration

Weighted blades were of built-up construction with leading edge or trailing edge mass balance.

* Average chord

/ Blades were 20% thick

Apparatus

The retochute models were mounted on a cantilever support in the 18 and 8 ft. test sections of the UAC Wind Tunnel. A diagram of the installation in the 8 ft. test section is presented as Figure G-1. The support was secured to a housing through two strain gaged links for measuring thrust. The housing was attached to two struts which were mounted on the wind tunnel balance frame. The downstream strut was used to pitch the model about an axis at the forward strut.

The pressure difference between the upper and lower surfaces of the blade was measured at five chordwise positions. These 5 pressure readings were individually repeated for 5 spanwise stations. The output signals from each of the five chordwise pressure gages along with the signals from the governor crank angle and coning angle potentiometers were transmitted by means of a slip ring assembly in the rotor hub. A sixteen channel oscillograph was used to record the pressure signals as well as the signals from the spring collar position indicator, the two thrust links, the rotor speed and the tunnel speed transducers. The rotor speed signal was transmitted from a variable reluctance pickup which was actuated by a magnetized slug inserted in the rotating governor spring disc. The rotor speed was also measured by a Hewlett-Packard frequency meter.

The tunnel airspeed was measured at four peripheral stations in the plane of the rotor disc to minimize wind tunnel interference effects. The four pressure orifices were then tied to a 5 psi Statham pressure transducer in order to obtain an average value of airspeed.

Provision was made to study the rotochute opening cycle by taking Fastax motion pictures as well as the conventional oscillograph records.

Tests

The tests were conducted with two purposes in mind; first to gain an insight into those phases of rotochute operation which could not be precisely analyzed because of the theoretical limitations of rotor aerodynamics and, secondly, to determine the operating characteristics of a rotochute with which to compare analytical methods. In general both of these aims were achieved.

The tests were divided into three phases. Phase I consisted principally in determining the effect of spring rate and solidity on the performance at high speed. For this series of tests, Models 1, 2 and 3 were used. During this phase, an attempt was made to measure the load distribution on the blades from which an inflow distribution could be calculated. The slip-ring assembly failed and unfortunately was not discovered until it was too late in the test period for retesting.

Performance characteristics of the model at low speed was one of the objectives of the second phase. This phase was conducted in the 18 ft. test section. The effect of solidity and of various changes in governor configuration were also investigated. For example, in the Kaman linkage system, changes in coning angle affect governor operation (see Section D). The equilibrium coning angle was, therefore, varied by providing for different amounts of underslung. The relationship between underslung and equilibrium coning angle is given in Appendix I. Governor operation with respect to the effects of blade mass, chordwise center of gravity and chord-

wise center of pressure relative to the feathering axis was investigated. In these tests, Models 4 to 19 of Table I were used.

The tests of the third phase were principally concerned with obtaining performance data on a tapered blade configuration which simulated the aerodynamic characteristics of the proposed prototype. For these tests, Models 20, 21, 22, 26 and 27 were used. The spring rate and preload were adjusted so that tip speeds of the same order as that proposed for the prototype were obtained. In addition, the model was restrained from rotating and the static starting torque was measured by means of a strain gaged link for various values of sweep and precone angles. Finally, time histories of the opening cycle were measured at various sweep angles, precone angles and Mach numbers. In general, the basic requirements of the tests were accomplished for the model configurations noted.

The data were reduced in accordance with the procedures outlined in Reference 20. A complete tabulation of the reduced data is given in Reference 22. In order to make the best use of the available time, the complete data reduction procedure was programmed for automatic computation on the IBM 704 calculator. The reduced data included time average values of the thrust coefficient, Mach number, rotor rotational speed and rotor drag coefficient. The oscillograph data were reduced to values of the governor-crank angle, coning and pitch angles, governor spring preload length, governor spring feathering moment and the differential pressures between the blade upper and lower surfaces measured at five chordwise and five spanwise stations. An extensive amount of instrumentation was used throughout the tests and a large quantity of data were recorded in rela-

[redacted]

tively short test periods. The frequency of the test periods prevented complete scrutinization of the unreduced data before they were reduced. A certain percentage of the computed results therefore are either in error or questionable. However, the primary purpose of the test programs was to provide experimental verification of the analytical methods. The data to be completely analyzed, therefore, were selected to compare with the calculations on an overall performance basis. Because of the good correlation obtained on an overall integrated basis, corroboration of the intermediate steps in the analyses was not considered necessary.



[redacted]

## H. ROTOCHUTE DESIGN PROCEDURE

The principles outlined in the preceding sections are used in designing a rotochute for a specific set of requirements. The requirements are usually given as specifications on the trajectory. The design procedure used to fulfill the trajectory specifications will now be described. The final design will depend on which of the specifications are to be emphasized. For example, if emphasis is placed on attitude angle at a particular drop distance, it may be more advantageous to design the rotochute to attain terminal descent after it has passed the peak value of rotor drag coefficient. The section on rotochute trajectories demonstrated this fact.

Whatever the emphasized specifications may be, however, the general dimensions of the rotochute must first be ascertained. With the specified terminal velocity and gross weight and an empirical attainable terminal velocity rotor drag coefficient the rotor radius is tentatively chosen as:

$$R = \sqrt{\frac{2W}{\pi \rho V_v^2 C_{D_R}}}$$

The solidity is chosen as the maximum attainable consistent with the geometric installation requirements, such as the fit of the rotochute and body either internally or in an external store on a particular aircraft. A maximum tip speed must then be tentatively chosen.

With the geometric parameters of radius, solidity and maximum tip speed chosen the rotochute blade can be laid out and the mass characteristics ascertained for purposes of preliminary performance and stress analyses.

The performance can then be calculated according to the methods outlined in sections A and B. The variation of rotor drag coefficient with advance ratio is thereby obtained. Using the tentatively chosen design maximum tip speed, an empirical variation of velocity with tip speed and the calculated performance curve, the trajectory is calculated according to the method outlined in section E. The calculated trajectory is compared with the specifications. If the specifications are not met, the rotor radius and/or tip speed is adjusted and the above procedure is repeated. The second recycling is usually sufficient to approximate the specified trajectory fairly closely.

Thus far the rotor radius, solidity and maximum tip speed have been established but not the actual variation of velocity with tip speed. To establish this relationship, the governor characteristics must be determined. The values of blade pitch and coning angles that are to be inserted into the feathering equilibrium equation are found from the performance analysis and that part of the governor analysis which determines the pitch angle at high advance ratios. The governor linkage mechanism is tentatively laid out and the dimensions determined. The solution of the feathering equilibrium equation is an iterative

procedure together with the opening cycle analysis since there are at least two unknowns; the advance ratio at which the maximum rotational speed is attained and the spring force. The advance ratio for maximum rotational speed is calculated from the opening cycle analysis (Section C).

The feathering equilibrium equation is then solved for the spring force at the aforementioned value of advance ratio as well as the advance ratio corresponding to terminal descent. The spring forces at these two advance ratios correspond to the extremes in spring displacement which are a result of the specific blade pitch angles necessary for autorotation at these conditions. The spring force results from a combination of spring rate and preload. A spring may therefore be chosen which, with an adequate combination of rate and preload, yields the required spring forces at these two conditions. Slight changes in governor link geometry may be necessary in this matching process. Having established the spring rate and preload, the feathering equilibrium equation can be solved for the rotational speed at several other advance ratios. The actual velocity-tip speed relationship for the particular governor geometry and spring characteristics is thereby established. The trajectory is recalculated and the results compared with the mission specifications. If the trajectory satisfied the specifications, the chosen value of maximum tip speed is satisfactory and a final weight estimation and stress analysis is made. Should the trajectory performance be

inadequate, minor modifications in governor design, maximum tip speed, or spring characteristics can be made and the procedure repeated. Thus, by successive analyses of preliminary and intermediate configurations, the final design can be established which will produce compliance with the trajectory and airplane stowage requirements.

## APPENDIX I

### DEVELOPMENT OF THE LOW SPEED PERFORMANCE EQUATIONS

In the development of the low speed performance method the following assumptions were made:

1. The Glauert-Lock empirical curves for thrust coefficients F and f can be applied to an elemental annulus (see text).
2. The lift and drag on any elemental annulus are the same as they would be if the blade section were in two-dimensional flow.
3. The tip loss is accounted for by assuming no lift on the outer 4 percent of the blade.

**Through Flow Velocity Equation**

The expression for an element of thrust, using assumption 2 is:

$$dT = \frac{\rho}{2} c \pi R^2 (\Omega R)^2 \cos\beta \left[ \left( y_I \cos\beta + e/R \right)^2 + \lambda^2 \cos^2\beta \right] \left( C_l \cos\phi + C_d \sin\phi \right) dy_I$$

Using Glauerts empirical thrust coefficient $f$ as a correction to the momentum theory,

$$dT = 4\pi\rho\, y_I R^2 (\Omega R)^2 \lambda_i^2 \cos^2\beta\, f \left( y_I \cos\beta + e/R \right) dy_I$$

Equating both expressions for thrust element and solving for f, the following is obtained:

$$f = \frac{\sigma}{8} \frac{\left[\left(y_I \cos\beta + e/R\right)^2 + \lambda^2 \cos^2\beta\right]\left(C_l \cos\phi + C_d \sin\phi\right)}{\lambda_d^2 \left(y_I \cos\beta + e/R\right) \cos\beta} \qquad \text{(I-1)}$$

Now referring to sketch (a)

$$\tan\phi = \frac{\lambda \cos\beta}{y_I \cos\beta + e/R} \qquad \text{(I-2)}$$

$$\sin\phi = \frac{\lambda \cos\beta}{\sqrt{\lambda^2 \cos^2\beta + \left(y_I \cos\beta + e/R\right)^2}} \qquad \text{(I-3)}$$

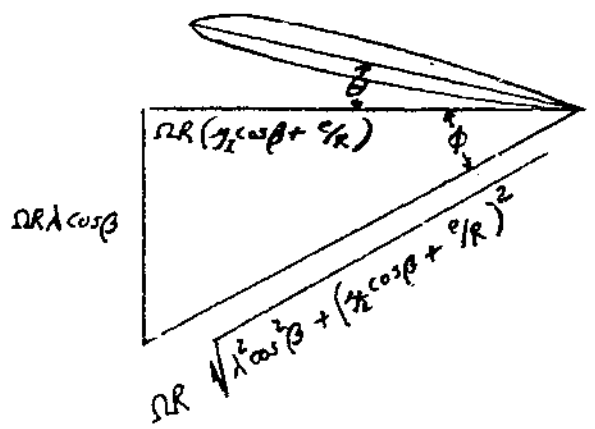


Sketch (a)

$$\cos\phi = \frac{\left(y_I \cos\beta + e/R\right)}{\sqrt{\lambda^2 \cos^2\beta + \left(y_I \cos\beta + e/R\right)^2}} \qquad \text{(I-4)}$$

UNCLASSIFIED

[redacted]

Now

$$\alpha_r = \theta + \phi = \theta + \arctan \frac{\lambda \cos\beta}{(y_I \cos\beta + e/R)}$$

Using the other Glauert thrust coefficient F

$$\lambda_d^2 f = \lambda^2 F$$

So

$$\lambda_d = \lambda\sqrt{\frac{F}{f}} \quad \text{or} \quad \lambda = \lambda_d\sqrt{\frac{f}{F}}$$

Substituting the above value for $\lambda$ into Equation I-1 as well as into the expressions for $\sin\phi$ and $\cos\phi$, Equation I-2 becomes:

$$\frac{\sigma}{8\lambda_d^2}\left[(y_I\cos\beta + e/R)^2 + \lambda_d^2\frac{f}{F}\cos^2\beta\right]^{1/2}(C_l + C_d\tan\phi) - f\cos\beta \qquad \text{(I-5)}$$

where $\tan\phi$ has become

$$\tan\phi = \frac{\lambda_d\sqrt{\frac{f}{F}}\cos\beta}{(y_I\cos\beta + e/R)}$$

Torque Equilibrium Equation

The blade element torque coefficient expression based on assumption 2 is:

$$dC_Q = \frac{\sigma}{2}(C_d\cos\phi - C_l\sin\phi)\left[(y_I\cos\beta + e/R)^2 + \lambda_d^2\frac{f}{F}\cos^2\beta\right](y_I\cos\beta + e/R)\,dy_I \qquad \text{(I-6)}$$

Substituting the values for $\sin\phi$ and $\cos\phi$ (Equations I-3 and I-4), Equation I-6 becomes:

UNCLASSIFIED

[redacted]

$$C_Q = \frac{\sigma}{2}\sum_{0}^{1}(C_d - C_l \tan\phi)\left[\left(y_I\cos\beta + e/R\right)^2 + \lambda_d^2\frac{f}{F}\cos^2\beta\right]^{1/2}\left(y_I\cos\beta + e/R\right)^2 \Delta y_I$$

where as before, $\tan\phi = \dfrac{\lambda_d\sqrt{\frac{f}{F}}\cos\beta}{y_I\cos\beta + e/R}$ .

This value of $C_Q$ must be zero for equilibrium autorotation.

Thrust Equation

Using the blade element expression for thrust coefficient,

$$dC_T = \frac{\sigma}{2}\left[\left(y_I\cos\beta + e/R\right)^2 + \lambda_d^2\frac{f}{F}\cos^2\beta\right]\left(C_l\cos\phi + C_d\sin\phi\right)\cos\beta\, dy_I \qquad \text{(I-7)}$$

Substituting the expressions for $\sin\phi$ and $\cos\phi$ Equation I-7 becomes:

$$dC_T = \frac{\sigma}{2}\cos\beta\left[C_l + C_d\tan\phi\right]\left(y_I\cos\beta + e/R\right)\left[\left(y_I\cos\beta + e/R\right)^2 + \lambda_d^2\frac{f}{F}\cos^2\beta\right]^{1/2} dy_I \qquad \text{(I-8)}$$

The expression for $C_l$ is summed from the second increment to the next to last whereas the expression containing $C_d$ is summed over the full radius. So,

$$C_T = \frac{\sigma}{2}\cos\beta\left\{\sum_{y_{I_2}}^{y_{n-1}} C_l\left(y_I\cos\beta + e/R\right)\left[\left(y_I\cos\beta + e/R\right)^2 + \lambda_d^2\frac{f}{F}\cos^2\beta\right]^{1/2}\Delta y_I\right.$$

$$\left. + \sum_{0}^{1} C_d\tan\phi\left(y_I\cos\beta + e/R\right)\left[\left(y_I\cos\beta + e/R\right)^2 + \lambda_d^2\frac{f}{F}\cos^2\beta\right]^{1/2}\Delta y_I\right. \qquad \text{(I-9)}$$


[redacted]

The rotor drag coefficient is then,

$$C_{D_R} = \frac{2C_T}{\lambda_d^2}$$

Coning Angle Expression

The coning angle is obtained from an equilibrium between the centrifugal and aerodynamic flapping moments.

The following are defined:

$\bar{\mu}$ - mass per foot of span

$\theta_0$ - the equilibrium coning angle assuming no aerodynamic force. Referring to sketch (b), it is the angle which brings the blade center of gravity to the plane of rotation and is a function of the undersling h .

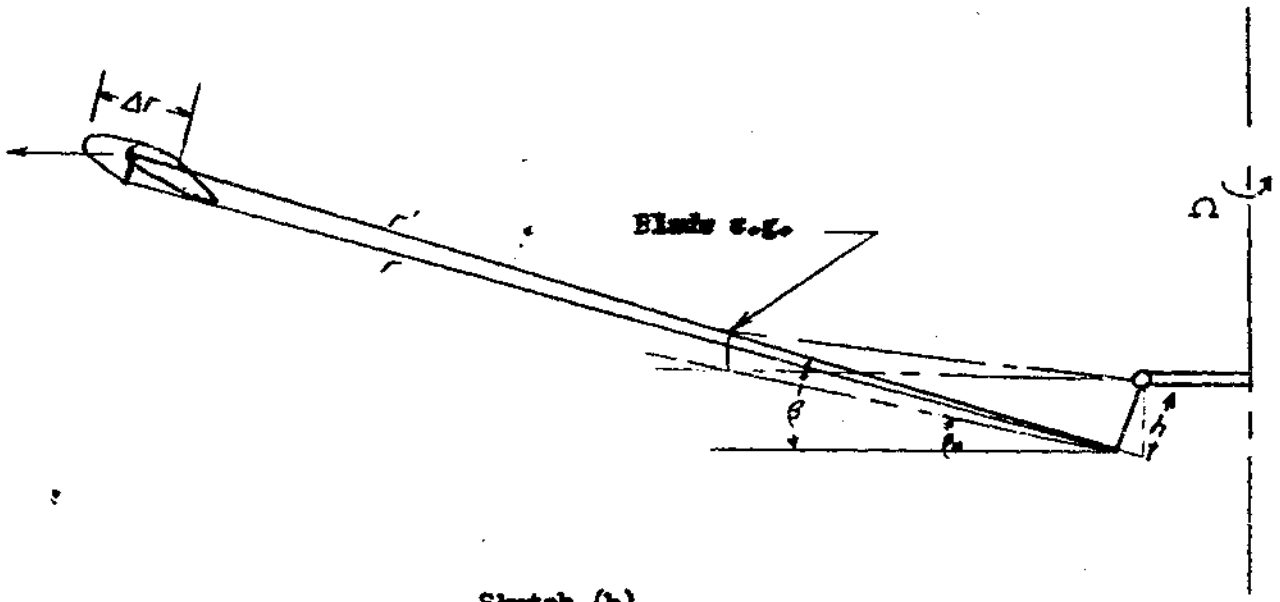


Sketch (b)

The centrifugal force on element $\Delta r$ , therefore is:

$$F_{CF} = \bar{\mu}\,\Delta r\,\Omega^2 (r'\cos\beta + e)$$

where $r' = R y_I + h\tan\beta$

The centrifugal force moment then is:

$$\Delta M_{CB} = \Omega^2 \bar{\mu} \left( [r + h\tan\beta]\cos\beta + e \right)\left( r\sin\beta - h\cos\beta \right) dr$$

Letting $y_I = \frac{r}{R}$ and $dr = R\,dy_I$

$$dM_{cB} = \bar{\mu}\,\Omega^2\left(\left[R y_I + h\tan\beta\right]\cos\beta + e\right)\left(y_I R\sin\beta - h\cos\beta\right) R\,dy_I$$

$$= \bar{\mu}(\Omega R)^2 R\left(y_I\cos\beta + \frac{h}{R}\sin\beta + \frac{e}{R}\right)\left(y_I\sin\beta - \frac{h}{R}\cos\beta\right) dy_I \qquad \text{(I-10)}$$

Now $\beta = \beta_0 + \beta'$, where $\beta_0$ is as defined.

Upon substitution for $\beta$, Equation I-10 becomes:

$$dM_{cB} = \bar{\mu}(\Omega R)^2 R\left[y_I\cos(\beta_0+\beta') + \frac{h}{R}\sin(\beta_0+\beta') + e/R\right]\left[y_I\sin(\beta_0+\beta') - \frac{h}{R}\cos(\beta_0+\beta')\right] \qquad \text{(I-11)}$$

Substituting the trigonometric equations for the functions of sums of angles, Equation I-11 becomes

$$dM_{cB} = \bar{\mu}(\Omega R)^2 R\left[y_I\cos\beta_0\cos\beta' - y_I\sin\beta_0\sin\beta' + \frac{h}{R}\sin\beta_0\cos\beta' + \frac{h}{R}\sin\beta'\cos\beta_0 + e/R\right]$$

$$\left[y_I\sin\beta_0\cos\beta' + y_I\sin\beta'\cos\beta_0 - \frac{h}{R}\cos\beta_0\cos\beta' + \frac{h}{R}\sin\beta_0\sin\beta'\right]\Delta y_I \qquad \text{(I-12)}$$

Since in this ragime $\beta$ will be small, the following small angle assumptions are made:

$$\cos\beta' = 1.0 \qquad \sin\beta_o = \beta_o \qquad \text{and } \sin\beta' = \beta'$$

The equation I-12 then becomes:

$$dM_{cB} = \bar{\mu}(\Omega R)^2 R\left[y_I\cos\beta_o - y_I\beta_o\beta' + \frac{h}{R}\beta_o + \frac{h}{R}\beta'\cos\beta_o + \frac{e}{R}\right] \cdot$$

$$\left[y_I\beta_o + y_I\beta'\cos\beta_o - \frac{h}{R}\cos\beta_o + \frac{h}{R}\beta_o\beta'\right] dy_I \qquad \text{(I-13)}$$

Multiplying the expressions in the brackets and summing over the blade the following is obtained:

$$M_{cB} = \bar{\mu}(\Omega R)^2 R\int_{e/R}^{1}\Big\{\left[y_I\frac{h}{R}\cos^2\beta_o - y_I^2\beta_o\cos\beta_o - y_I\frac{h}{R}\beta_o^2 + \left(\frac{h}{R}\right)^2\beta_o\cos\beta_o\right]\beta'^2$$

$$+\left[3\frac{h}{R}y_I\beta_o\cos\beta_o - \left(\frac{h}{R}\right)^2\cos^2\beta_o - y_I^2\beta_o^2 + y_I\cos^2\beta_o + \frac{e}{R}y_I\cos\beta_o + \frac{h}{R}\beta_o\cos\beta_o + \left(\frac{h}{R}\right)^2\beta_o^2 + \frac{he}{R^2}\beta_o\right]\beta'$$

$$-\frac{h}{R}\cos^2\beta_o - \left(\frac{h}{R}\right)^2\beta_o\cos\beta_o - \frac{he}{R^2}\cos\beta_o + y_I\beta_o\cos\beta_o + y_I\frac{h}{R}\beta_o^2 + y_I\frac{e}{R}\beta_o\Big\}dy_I \qquad \text{(I-14)}$$

This can be simplified by assuming $h$ will be small compared to $R$ and $\beta'^2 \approx 0$.

The aerodynamic moment is written, assuming the contribution due to $C_d$ is negligible as;

$$M_A = \frac{\rho}{2} c (\Omega R)^2 R \int_{e/R}^{B} C_l \, y_I^2 \, dy_I \qquad \text{(I-15)}$$

Equating the two moment expressions the result is:

$$\bar{\mu} \int \Big\{ \Big[ 3\frac{h}{R} y_I \beta_0 \cos\beta_0 + y_I \cos^2\beta_0 + \frac{e}{R} y_I \cos\beta_0 + \frac{h}{R}\beta_0 \cos\beta_0 \Big]\beta' - \frac{h}{R}\cos^2\beta_0$$
$$- \frac{he}{R^2}\cos\beta_0 + y_I \beta_0 \cos\beta_0 + y_I \frac{e}{R}\beta_0 \Big\} dy_I = \frac{\rho}{2} c R \int C_l \, y_I^3 \, dy_I \qquad \text{(I-16)}$$

which becomes,

$$\Big[ 3\frac{h}{R}\beta_0 \cos\beta_0 \int \bar{\mu}\, y_I \, dy_I + \cos^2\beta_0 \int \bar{\mu}\, y_I \, dy_I + \frac{e}{R}\cos\beta_0 \int \bar{\mu}\, y_I \, dy_I + \frac{h}{R}\beta_0 \cos\beta_0 \int \bar{\mu}\, dy_I \Big]\beta'$$

$$= \frac{h}{R}\cos^2\beta_0 \int \bar{\mu}\, dy_I + \frac{he}{R^2}\cos\beta_0 \int \bar{\mu}\, dy_I - \beta_0 \cos\beta_0 \int \bar{\mu}\, y_I \, dy_I - \frac{e}{R}\beta_0 \int \bar{\mu}\, y_I \, dy_I + \frac{\rho}{2} c R \int C_l \, y_I^3 \, dy_I$$

(I-17)

Now let

$$\int \bar{\mu}\, y_I \, dy_I = S_s \qquad \int \bar{\mu}\, dy_I = P \qquad \int C_l \, y_I^3 \, dy_I = \Sigma_4$$

Then

$$\beta' = \frac{\left[\cos^2\beta_0 + \frac{e}{R}\cos\beta_0 - \cos\beta_0 - \frac{e}{R} + \frac{\rho c R \Sigma_4}{2\beta_0 S_s}\right]}{\cos\beta_0\left[\frac{3h}{R} + \frac{\cos\beta_0}{\beta_0} + \frac{e}{R\beta_0} + \beta_0\right]} \tag{I-18}$$

Now assuming $\beta_0$ is a small angle, $\tan\beta_0 = \beta_0$ and as

$$\beta_0 = \frac{hP}{RS_s}$$

So

$$\beta' = \frac{\left[\cos\left(\frac{hP}{RS_s}\right) + \frac{e}{R} - 1 - \frac{e}{R}\frac{1}{\cos\frac{hP}{RS_s}} + \frac{\rho c R \Sigma_4}{\frac{2hP}{R}\cos\frac{hP}{RS_s}}\right]}{\frac{3h}{R} + \frac{RS_s}{hP}\cos\frac{hP}{RS_s} + \frac{e}{h}\frac{S_s}{P} + \frac{hP}{RS_s}}$$

$$\beta = \beta_0 + \beta' \tag{I-19}$$

$$\beta = \frac{hP}{RS_s} + \frac{\left[\cos\left(\frac{hP}{RS_s}\right) + \frac{e}{R} - 1 - \frac{e}{R}\sec\left(\frac{hP}{RS_s}\right) + \frac{\rho c R^2 \Sigma_4}{2hP\cos\left(\frac{hP}{RS_s}\right)}\right]}{3h/R + \frac{R}{h}\frac{S_s}{P}\cos\frac{hP}{RS_s} + \frac{eS_s}{hP} + \frac{hP}{RS_s}} \tag{I-20}$$

## APPENDIX II

### OPENING CYCLE EQUATIONS OF MOTION

The equations of motion for the high-speed rotochute were developed using Lagrange's equations and the assumption that the mass of the blade could be concentrated in a single line. This assumption means that the chordwise inertia is negligible compared to the spanwise inertia and that the spanwise moment of inertia about a line parallel to the chord is equal to the spanwise moment of inertia about a line normal to the chord.

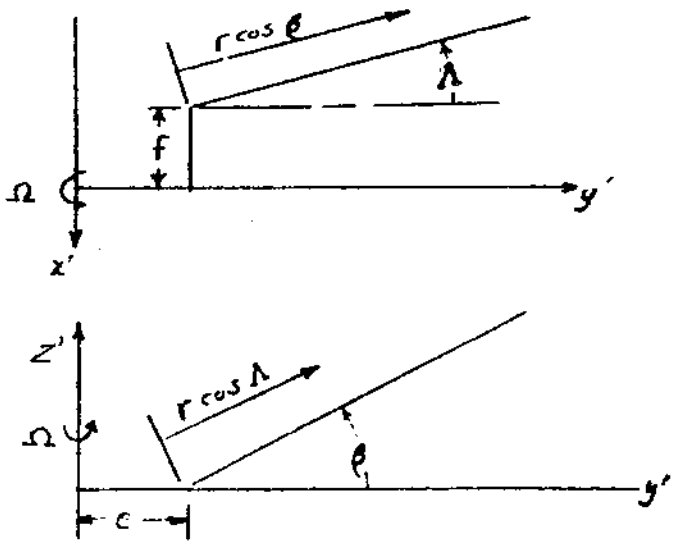


The coordinates of any point on the blade can be written in the rotating coordinate system as:

$$x' = -f - r\cos\beta\sin\Lambda$$

$$y' = e + r\cos\beta\cos\Lambda$$

$$z' = r\cos\Lambda\sin\beta$$

In non-rotating coordinates these are:

$$x = x' \cos \psi - y' \sin \psi$$

$$y = y' \cos \psi + x' \sin \psi$$

$$z = z'$$

Differentiate these with respect to time and put them in the kinetic energy equation,

$$T = \frac{1}{2} \int \bar{\mu} \left( \dot{x}^2 + \dot{y}^2 + \dot{z}^2 \right) dr$$

which then yields,

$$T = \frac{1}{2} \Big\{ f^2 P \dot{\psi}^2 + I_s \dot{\beta}^2 \sin^2\beta \sin^2\Lambda + I_s \dot{\psi}^2 \cos^2\beta \sin^2\Lambda + e^2 P \dot{\psi}^2$$

$$+ I_s \dot{\beta}^2 \sin^2\beta \cos^2\Lambda + I_s \dot{\psi}^2 \cos^2\beta \cos^2\Lambda + 2 f S_s \dot{\beta} \dot{\psi} \sin\beta \cos\Lambda$$

$$- 2 e S_s \dot{\psi} \dot{\beta} \sin\beta \sin\Lambda + 2 e S_s \dot{\psi}^2 \cos\beta \cos\Lambda + 2 f S_s \dot{\psi}^2 \cos\beta \sin\Lambda$$

$$+ I_s \dot{\beta}^2 \cos^2\Lambda \cos^2\beta \Big\} \qquad \text{(II-1)}$$

Lagrange's equation now states that:

$$\frac{d}{dt}\left(\frac{\partial T}{\partial \dot{\psi}}\right) - \frac{\partial T}{\partial \psi} = Q \qquad \text{for rotation, and}$$

(II-2)

$$\frac{d}{dt}\left(\frac{\partial T}{\partial \dot{\beta}}\right) - \frac{\partial T}{\partial \beta} = M_f \qquad \text{for flapping.}$$

Substituting the equation for the kinetic energy into Lagrange's equation:

For rotation:

$$\ddot{\psi}\left[f^2P + e^2P + I_s\cos^2\beta + 2fS_s\cos\beta\sin\Lambda + 2eS_s\cos\beta\cos\Lambda\right]$$
$$+ \ddot{\beta}\left[fS_s\sin\beta\cos\Lambda - eS_s\sin\beta\sin\Lambda\right] + \dot{\psi}\dot{\beta}\left[-2I_s\sin\beta\cos\beta\right.$$
$$\left.-2eS_s\sin\beta\cos\Lambda - 2fS_s\sin\beta\sin\Lambda\right] + \dot{\beta}^2\left[fS_s\cos\beta\cos\Lambda\right.$$
$$\left.- eS_s\cos\beta\sin\Lambda\right] = Q \qquad \text{(II-3)}$$

For flapping:

$$\ddot{\psi}\left[fS_s\sin\beta\cos\Lambda - eS_s\sin\beta\sin\Lambda\right] + \ddot{\beta}\left[I_s\sin^2\beta + I_s\cos^2\beta\cos^2\Lambda\right]$$
$$+ \dot{\psi}^2\left[I_s\sin\beta\cos\beta + eS_s\sin\beta\cos\Lambda + fS_s\sin\beta\sin\Lambda\right]$$
$$+ \dot{\beta}^2\left[I_s\sin\beta\cos\beta\sin^2\Lambda\right] = M_{flap.} \qquad \text{(II-4)}$$

## APPENDIX III

### FEATHERING EQUILIBRIUM EQUATIONS

Centrifugal Feathering Moment:

In order to write an equation for the centrifugal feathering moment, the various components of centrifugal force must be found and multiplied by their moment arms. These forces were divided into those acting about the feathering hinge and those acting about the z -axis. Referring to figure D-1,

The moments about the feathering hinge;

$$M_{CT} = \Omega^2 \int_{blade} (x-f) z \, d\bar{u} + \Omega^2 \int_{blade} (y+e) z \sin\delta \, d\bar{u} \qquad \text{(III-1)}$$

The moments about the z -axis;

$$M_z = \Omega^2 \int_{blade} (y+e) x \, d\bar{u} - \Omega^2 \int_{blade} (x-f) y \, d\bar{u} \qquad \text{(III-2)}$$

By referring again to figure D-1 it is seen that the moment about the z -axis can be transformed into a moment acting in the same direction as the moment about the feathering hinge. First, let $M_z$ equal $F[d\cos\Delta \sec\delta]$ where F is a force acting at the junction of the flapping link and the governor crank link in a direction parallel to the x - y plane. Now, letting F' equal a force parallel to the z -axis one can write an equilibrium about the fulcrum H ;

$$F\cos\delta(e\sin\gamma) = F' e \cos\gamma \qquad \text{(III-3)}$$

The feathering moment derived from the moments about the z -axis is,

$$M_{CT} = F'(d \cos\Delta \sec\delta) \quad \text{, or} \tag{III-4}$$

$$M_{CT} = \left[\Omega^2 \int_{blade} (y+e)\, x\, d\bar{m} - \Omega^2 \int_{blade} (x-f)\, y\, d\bar{m}\right] \cos\delta \tan\gamma \tag{III-5}$$

The total centrifugal feathering moment is then;

$$M_{CT} = \Omega^2 \left\{ \left[ \int_{blade} (y+e)\, x\, d\bar{m} - \int_{blade} (x-f)\, y\, d\bar{m} \right] \cos\delta \tan\gamma + \int_{blade} (x-f)\, z\, d\bar{m} + \int_{blade} (y+e)\, z \sin\delta\, d\bar{m} \right. \tag{III-6}$$

or combining terms

$$M_{CT} = \Omega^2 \int_{blade} \left\{ [fy + xe] \cos\delta \tan\gamma + z[(x-f) + (y+e) \sin\delta] \right\} d\bar{m} \tag{III-7}$$

From figure D-1 expressions for the coordinates x , y , and z of an element of mass on the blade can be written;

$$x = \cos\delta\left[-R y_I \sin\beta \sin\theta_h + R x_I \cos\theta_h + h \cos\beta \sin\theta_h\right] - \sin\delta\left[h \sin\beta + R y_I \cos\beta\right] \tag{III-8}$$

$$y = \cos\delta\left[h \sin\beta + R y_I \cos\beta\right] + \sin\delta\left[-R y_I \sin\beta \sin\theta_h + R x_I \cos\theta_h + h \cos\beta \sin\theta_h\right] \tag{III-9}$$

$$z = R y_I \sin\beta \cos\theta_h + R x_I \sin\theta_h - h \cos\beta \cos\theta_h \tag{III-10}$$

[redacted]

Substituting equations III-8, III-9, and III-10 into equation III-7 and integrating over the blade the centrifugal feathering moment is obtained as follows:

$$
\begin{aligned}
M_{CT} = \Omega^2 \Big\{ & \big[ f S_c \theta_h - I_c \theta_h - e S_c \theta_h \delta - I_c \theta_h \delta^2 + f S_c \delta \tan\gamma + e S_s \tan\gamma \big] \\
& - \big[ f S_s + I_p \theta_h^2 - I_p - e S_s \delta + I_p \theta_h^2 \delta^2 - I_p \delta^2 - f S_s \theta_h \delta \tan\gamma \\
& - f h P \tan\gamma + c h P \delta \tan\gamma - e S_s \theta_h \tan\gamma \big] \sin\beta \\
& - \big[ - f h P - h S_c \theta_h^2 + h S_c + e h P \delta - h S_c \theta_h^2 \delta^2 + h S_c \delta^2 + f h P \theta_h \delta \tan\gamma \\
& - f S_s \tan\gamma + e S_s \delta \tan\gamma + e h P \theta_h \tan\gamma \big] \cos\beta + \big[ I_s \theta_h + I_s \theta_h \delta^2 \big] \sin^2\beta \\
& + \big[ h^2 P \theta_h + h^2 P \theta_h \delta^2 \big] \cos^2\beta + \big[ -2 h S_s \theta_h - 2 h S_s \theta_h \delta^2 \big] \sin\beta \cos\beta
\end{aligned}
\qquad \text{(III-11)}
$$

where $\delta$ has been assumed small so that $\sin\delta = \delta$ and $\cos\delta = 1$.

In the integration the following terms are defined;

$$R^2 \int_{blade} y_I^2 \, d\bar{m} = I_s \qquad R \int_{blade} y_I \, d\bar{m} = S_s$$

$$R^2 \int_{blade} x_I^2 \, d\bar{m} = I_c \qquad R \int_{blade} x_I \, d\bar{m} = S_c$$

$$R^2 \int_{blade} x_I y_I \, d\bar{m} = I_p \qquad \int_{blade} d\bar{m} = P$$


[redacted]

[redacted]

Aerodynamic Moment about Feathering Axis

At high speed, assume the moment about the z axis due to the chord force is zero as the z axis is close to the axis of rotation where the torque is balanced. Referring to figure D-1 and sketch (a),

$M_{Af_1}$ is the moment about feathering axis as such

$$M_{Af_1} = -\frac{\rho}{2}(\Omega R)^2 c R^2 \sum_{h/R}^{1} \left[ c_n \bar{x}_I + c\left(\frac{h}{R} - y_I \tan\beta\right)\right]$$

$$\left\{ \left(y_I \cos\beta + \frac{e}{R}\right)^2 + \left[\lambda_d - \lambda_i\right]^2 \cos^2\beta \right\} \Delta y_I \cos\beta \cos\theta_h$$

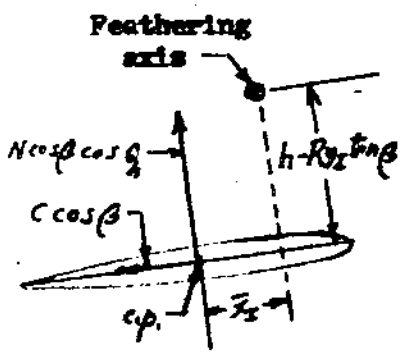


Sketch (a)

Let $M_{Af_2}$ equal the moment about the feathering axis due to the reaction from the link arm caused by $M_{Az}$

The aerodynamic force normal to the z axis is,

$$F_A = \sum_{h\sin\beta}^{R} \left[ N\cos\beta \sin\theta_h + C\cos\beta\cos\theta_h \right] \Delta y_I \qquad \text{(III-13)}$$

The moment of this force about the x axis is:

$$M_z = -\sum_{h/R\sin\beta}^{1} R N \cos\beta \sin\theta_h \, y_I \Delta y_I - R\sum_{h/R\sin\beta}^{1} C\cos\beta\cos\theta_h \, y_I \Delta y_I$$



[redacted]

Using the preceeding assumption,

$$M_Z = -R\sum_{h/R\sin\beta}^{1} N\, y_I \cos\beta \sin\theta_h \Delta y_I$$

Referring to the equation for the centrifugal moment, equation III-5

$$M_{H_2} = M_Z \cos\delta \tan\gamma$$ , therefore

$$M_{A_{f_2}} = -\sum_{h/R\sin\beta}^{1} \frac{\rho}{2}(\Omega R)^2 c R^2 C_n y_I \cos\beta \sin\theta_h \cos\delta \tan\gamma$$

$$\left\{\left(y_I\cos\beta + e/R\right)^2 + (\lambda_d - \lambda_i)^2\cos^2\beta\right\}\Delta y_I \qquad \text{(III-16)}$$

The total aerodynamic feathering moment therefore is:

$$M_A = M_{A_{f_1}} + M_{A_{f_2}}$$

$$M_A = -\frac{\rho}{2}(\Omega R)^2 c R^2 \cos\beta \left\{\sum_{h/R\sin\beta}^{1} R\cos\theta_h\left(C_n \Sigma_I + C_c\left[\frac{h}{R} - y_I\tan\beta\right]\right)\right.$$

$$\left[\left(y_I\cos\beta + e/R\right)^2 + (\lambda_d - \lambda_i)^2\cos^2\beta\right]\Delta y_I + R\sum_{h/R\sin\beta}^{1} C_n y_I \sin\theta_h \cos\delta \tan\gamma$$

$$\left.\left[\left(y_I\cos\beta + e/R\right)^2 + (\lambda_d - \lambda_i)^2\cos^2\beta\right]\Delta y_I\right\} \qquad \text{(III-17)}$$

This must be solved on a strip-wise basis. $C_n$ and $C_c$ are functions of the respective angles of attack at each station which is,

$$\alpha_r = \theta + \arctan\frac{(\lambda_d - \lambda_i)\cos\beta}{y_I\cos\beta + e/R}$$

## APPENDIX IV

### ROTOR RIGIDITY FACTOR

The rotor rigidity factor can be interpreted as the ratio of the apparent moment about the blade flapping hinge with the design blade configuration to the apparent moment about the blade flapping hinge with an assumed rigid rotor configuration for any given rotochute disturbance from the equilibrium. A rigorous solution for the rotor rigidity factor can be obtained, but would involve lengthy aerodynamic and blade flexibility calculations using the approach of reference 19. For design purposes it appears that the rotor rigidity factor can be reasonably approximated by a rather simple approach. With no loss in generality the incremental blade forces can be represented by a cyclic pitch variation. Further, the flexible rotor system can be represented by blades which flap about a restrained flapping hinge (schematic diagram below).

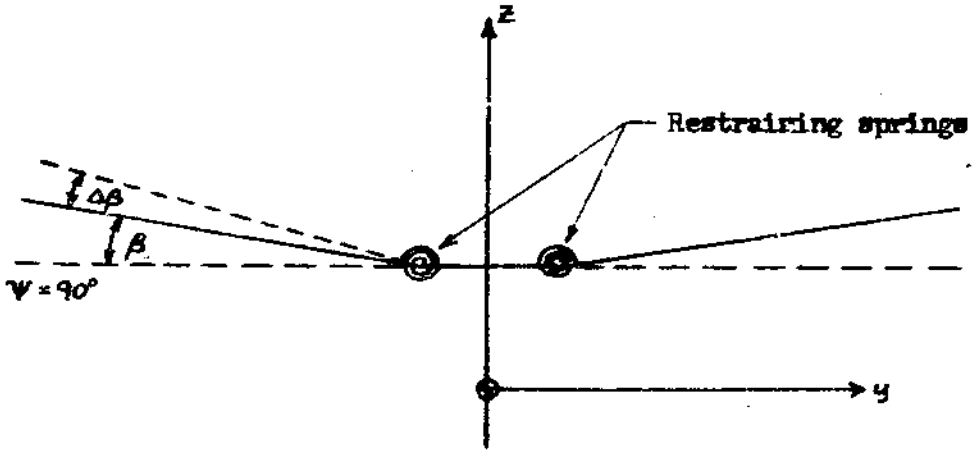

The blade flapping equation of motion can be written

$$I_b(\Delta\ddot{\beta}) + I_b\Omega^2(\Delta\beta) + C_\beta(\Delta\beta) = \frac{\partial M_\beta}{\partial\theta}\left(\theta - \frac{\Delta\dot{\beta}}{\Omega}\right) \qquad \text{(IV-1)}$$

where $C_\beta$ is the spring constant of the flapping hinge restraint, $M_\beta$ is the aerodynamic moment about the flapping hinge, and $\theta$ is the cyclic pitch variation. Considering first harmonic flapping

$$\Delta\beta = \beta_1 \sin\Omega t + \beta_2 \cos\Omega t$$
$$\theta = \theta_1 \sin\Omega t \qquad \text{(IV-2)}$$

By substitution of Equations IV-2 in Equation IV-1, it is apparent that the inertia terms cancel; the equation of motion becomes

$$C_\beta(\beta_1 \sin\Omega t + \beta_2 \cos\Omega t) = \frac{\partial M_\beta}{\partial\theta}(\theta_1 \sin\Omega t - \beta_1 \cos\Omega t + \beta_2 \sin\Omega t) \qquad \text{(IV-3)}$$

Equating the coefficients of $\sin\Omega t$ and $\cos\Omega t$ separately this can be written

$$C_\beta\beta_1 - \frac{\partial M_\beta}{\partial\theta}\beta_2 = \frac{\partial M_\beta}{\partial\theta}\theta_1 \qquad \text{(IV-4)}$$

$$C_\beta\beta_2 + \frac{\partial M_\beta}{\partial\theta}\beta_1 = 0 \qquad \text{(IV-5)}$$

Equations (IV-4) and (IV-5) can be solved simultaneously for $\beta_1$

$$\beta_1 = \frac{\frac{\partial M_\beta}{\partial \theta}\theta_1 c_\beta}{c_\beta^2 + \left(\frac{\partial M}{\partial \theta}\right)^2} \qquad \text{(IV-6)}$$

The flapping hinge moment of the flexible system can be written

$$M_{flex} = c_\beta \beta_1 \qquad \text{(IV-7)}$$

and the flapping hinge moment of the rigid system is given by

$$M_{rig} = \frac{\partial M_\beta}{\partial \theta}\theta_1 \qquad \text{(IV-8)}$$

Thus, making use of Equations (IV-6) through IV-8), the rotor rigidity factor can be written

$$k = \frac{M_{flex}}{M_{rig}} = \frac{c_\beta^2}{c_\beta^2 + \left(\frac{\partial M}{\partial \theta}\right)^2} \qquad \text{(IV-9)}$$

The aerodynamic moment derivative, $\partial M_\beta / \partial \theta$ , can be approximated as follows:

$$\frac{\partial M_\beta}{\partial \theta} = R \frac{\partial}{\partial \theta} \int_\xi^1 (\bar{r} - \xi)\left(\frac{dT}{b \cos\beta}\right) \qquad \text{(IV-10)}$$

where, since $\xi$ and $\beta$ are both small, the differential thrust per blade can be written

$$\frac{dT}{b} = \frac{1}{2}\pi\rho\frac{\sigma}{b}\Omega^2 R^4 (\bar{r} C_l + \lambda C_d)\sqrt{\lambda^2+\bar{r}^2}\,\cos^3\beta\, d\bar{r} \qquad \text{(IV-11)}$$

$$\frac{\partial}{\partial\theta}\left(\frac{dT}{b}\right) = \frac{1}{2}\pi\rho\frac{\sigma}{b}\Omega^2 R^4 \left(\bar{r}\frac{\partial C_l}{\partial\theta} + \lambda\frac{\partial C_d}{\partial\theta}\right)\sqrt{\lambda^2+\bar{r}^2}\,\cos^3\beta\, d\bar{r} \qquad \text{(IV-12)}$$

In general, the inner portion of blade is stalled even for terminal descent conditions. It can thus be assumed that

$$\begin{aligned} &\bar{r}\frac{\partial C_l}{\partial\theta} + \lambda\frac{\partial C_d}{\partial\theta} \approx 0 \quad , \quad \xi \leq \bar{r} < \bar{r}_s \\ &\bar{r}\frac{\partial C_l}{\partial\theta} + \lambda\frac{\partial C_d}{\partial\theta} \approx \bar{r}\frac{\partial C_l}{\partial\theta} = a\bar{r} \quad , \quad \bar{r}_s < \bar{r} \leq 1.0 \end{aligned} \qquad \text{(IV-13)}$$

where $\bar{r}_s$ is the non-dimensional radius which separates the stalled and unstalled portions of the blade. Thus, substituting Equation (IV-12) into (IV-10) and making use of the relationships of Equations (IV-13), the moment derivative about the flapping hinge becomes

$$\frac{\partial M_\beta}{\partial\theta} = \frac{1}{2}\pi\rho\frac{\sigma}{b}\Omega^2 R^5 \int_{\bar{r}_s}^{1} a\bar{r}\sqrt{\lambda^2+\bar{r}^2}\,(\bar{r}-\xi)\cos^2\beta\, d\bar{r} \qquad \text{(IV-14)}$$

Since for unstalled flow the net inflow parameter, $\lambda$, is small, the approximation

$$\sqrt{\lambda^2 + \bar{r}^2}\,(\bar{r} - \xi) \approx \bar{r}^2, \qquad \bar{r}_s < \bar{r} \leq 1.0$$

appears to introduce no appreciable error.

Integration of Equation (IV-14) then leads to the simple result

$$\frac{\partial M_\beta}{\partial \theta} \cong \frac{1}{8}\Omega^2 I_b \gamma \cos^2\beta\,(1 - \bar{r}_s^4)$$

$$\cong \frac{1}{8}\Omega^2 I_b \gamma \cos^2\beta \qquad \text{(IV-15)}$$

where the lock number, $\gamma$, is defined

$$\gamma = \frac{\pi \rho a \sigma R^5}{b I_b}$$

It appears that the approximation for $\partial M_\beta / \partial \theta$ will be reasonably accurate for the rotochute at terminal descent. The rotor rigidity factor, Equation (IV-9), can thus be written

$$k = \frac{\left(\frac{\omega_\beta}{\Omega}\right)^4}{\left(\frac{\omega_\beta}{\Omega}\right)^4 + \left(\frac{\gamma}{8}\cos^2\beta\right)^2}$$

where

$$\left(\frac{\omega_\beta}{\Omega}\right)^2 = \frac{c_\beta}{I_b \Omega^2}$$

Rigorously, $\omega_\beta$ is the static natural circular frequency of a rigid blade oscillating in the flapping mode about a restrained hinge. This represents, for practical configurations, the static natural flapping frequency of a flexible blade with the synchronizer linkage locked at the rotor axis. It is interesting to note that the rotor rigidity factor shows a dependence on cone angle. For the usual condition of small cone angle at terminal descent, however, the influence of small changes in cone angle should not be particularly significant.

The ratio of blade static flapping frequency to rotor rotation velocity, $\omega_\beta/\Omega$, is of greater significance. The fourth power of the ratio appears in the expression for the rotor rigidity factor. Thus changes in either the blade natural frequency or the rotor rotational velocity should have a pronounced effect on the rotor rigidity. Since the blade natural frequency is fixed for a particular rotor design, any variation in the ratio can be considered to be a change in the rotor speed, $\Omega$. In Figure F-6 the variation in rotor rigidity factor as a function of $\omega_\beta/\Omega$ is shown. The adverse affect of increased rotor speed or decreased blade static flapping frequency is clearly indicated. Increased rotor speed has been shown to have a deleterious affect on rotochute stability in test flights conducted with several rotochute configurations. It appears that the trend indicated in Figure F-6 offers a partial explanation for the adverse effects of increased rotor speed.

REFERENCES

1. Glauert, H.: The Analysis of Experimental Results in the Windmill Brake and Vortex Ring States of an Airscrew. Br. ARC R & M 1026

2. Lock, C.N.H., Bateman, H. & Townsend, C.H.: An Extension of the Vortex Theory of Airscrews of Small Pitch, Including Experimental Results. Br. ARC R & M 1014

3. Abbott, I.H., von Doenhoff, A.E., and Stivers, L.S., Jr: A Summary of Airfoil Data, NACA Rep. No. 824, 1945

4. Goett, Harry I. & Bullivant, W.K.: Tests of NACA 0009, 0012, and 0018 Airfoils in the Full Scale Tunnel. NACA Rep. No. 647, 1938

5. Loftin, L.K. and Smith, H.: Aerodynamic Characteristics of 15 NACA Airfoil Sections at Seven Reynolds Numbers from $.7 \times 10^6$ to $9 \times 10^6$. NACA TN 1945, 1949

6. Spreiter, J.R. and Steffen, R.J.: Effect of Mach Number and Reynolds Number on the Maximum Lift Coefficient. NACA TN 1044, 1946

7. Muse, T.C.: Some Effects of Reynolds and Mach Numbers on the Lift of an NACA 0012 Rectangular Wing in the NACA 19-foot Pressure Tunnel. NACA Wartime Rep. L-406, 1943

8. Wilson, H.B., Jr. and Horton E.A.: Aerodynamic Characteristics at High and Low Subsonic Mach Numbers of Four NACA 6-Series Airfoil Sections at Angles of Attack from $-2^\circ$ to $31^\circ$. NACA RM L53c20, 1953

9. Berggren, R.E. and Graham, D.J.: Effects of Leading-Edge Radius and Maximum Thickness-Chord Ratio on the Variation with Mach Number of the Aerodynamic Characteristics of Several Thin NACA Airfoil Sections NACA TN 3172, 1954

10. Graham, D.J., Nitsberg, G.E. and Olson, R.N.: A Systematic Investigation of Pressure Distributions at High Speed over 5 Representative NACA Low Drag and Conventional Airfoil Sections. NACA Rep. No. 832, 1945

11. Goethert, B.: High Speed Tests on Symmetrical Profiles with Different Thickness Ratios in the DVL High Speed Tunnel and Comparison with Measurements in Other Wind Tunnels. Technical Transfer No. TT-38 National Research Council of Canada. Dec. 17, 1951

12. Cris Critzos, Heyson, Harry and Boswinkle, Robert: The Aerodynamic Characteristics of the NACA 0012 Airfoil Section at Angles of Attack from 0 to 180°. NACA TN 3361, January 1955

13. Himmelskamp, H.: Profilmessungen an einem umlaufenden Propeller. Thesis Gottingen (1945) Reports of the Max Planck Institute, Gottingen, No. 2, 1950

14. Rushemann, D.: Types of Flow on Swept Wings. Journal of the Royal Aeronautical Society Vol. 57, No. 515, November 1953

15. Gessow, Alfred and Myers, Garry C. Jr.: Aerodynamics of the Helicopter. The MacMillan Company, New York, 1952

16. Allen, H. Julian: Estimation of the Forces and Moments Acting on Inclined Bodies of Revolution of High Fineness Ratio. NACA RM A9I26, 1949

17. Allen, H. Julian and Perkins, Edward W.: Characteristics of Flow Over Inclined Bodies of Revolution. NACA RM A50H 7, 1951

18. Johnson, Harold S.: Wind Tunnel Investigation at Low Speed of the Effect of Varying the Ratio of Body Diameter to Wing Span from 0.1 to 0.6 on the Aerodynamic Characteristics in Pitch of a 45° Sweptback Wing-Body Combination. NACA RM L53J09a, 1953

19. Berman, Alex: Response Matrix Method of Rotor Blade Analysis. Journal of the Aeronautical Sciences Vol. 23, No. 2, 1956

20. Wilson, John C.: Tests of a Kaman Aircraft Corporation Type-K Rotochute Model in the United Aircraft Corporation 8-foot Wind Tunnel. UAC Research Dept. Report No. R-0991-1, 1956

21. Watkins, D. J.: Final Report of Sandia Rotochute Program, Phase I Preliminary Design Study, Kaman Aircraft Corporation Report R-176 7 March 1957

22. Fitzpatrick, J. E.: Sandia Rotochute Program Phase I. Wind Tunnel Test Data, Kaman Aircraft Corporation Report R-181, April 1957

[redacted]

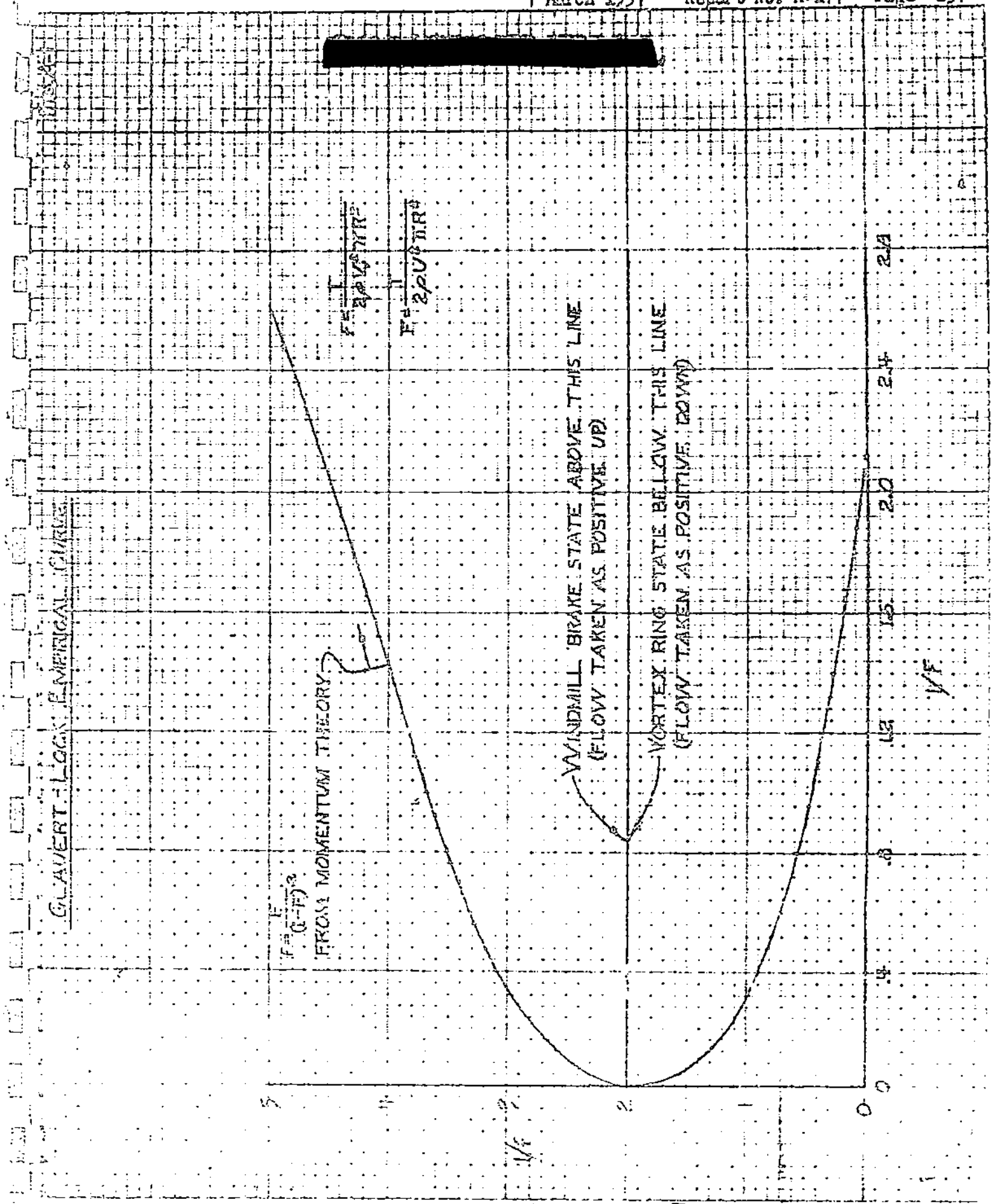


[redacted] UNCLASSIFIED

FIG. A-2

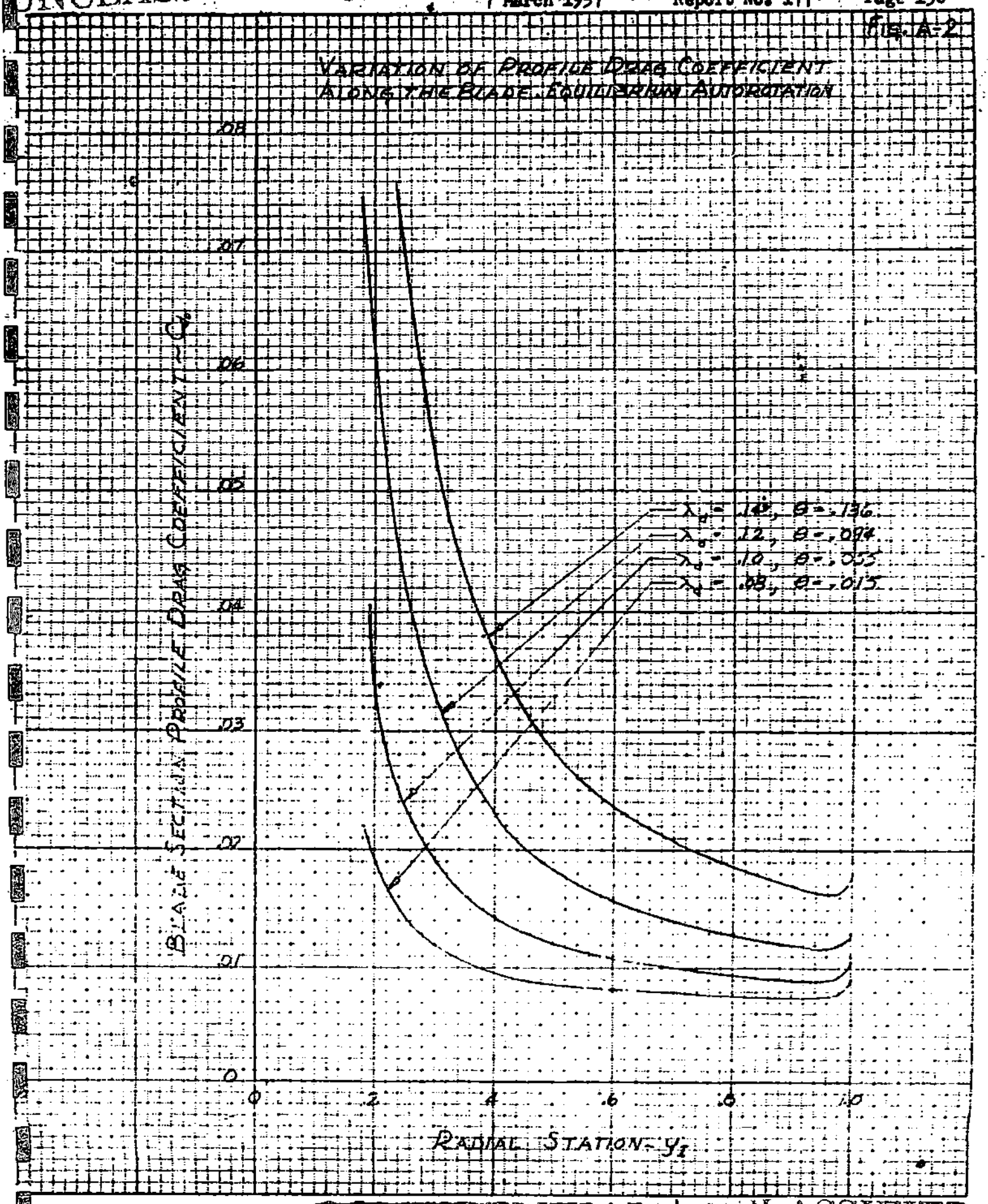
VARIATION OF PROFILE DRAG COEFFICIENT
ALONG THE BLADE. EQUILIBRIUM AUTOROTATION
BLADE SECTION PROFILE DRAG COEFFICIENT - $C_{d_0}$
.08
.07
.06
.05
.04
.03
.02
.01
0
0
.2
.4
.6
.8
1.0
RADIAL STATION - $y_I$
$\lambda_d$ = .14, $\theta$ = .136
$\lambda_d$ = .12, $\theta$ = .094
$\lambda_d$ = .10, $\theta$ = .055
$\lambda_d$ = .08, $\theta$ = .015

UNCLASSIFIED

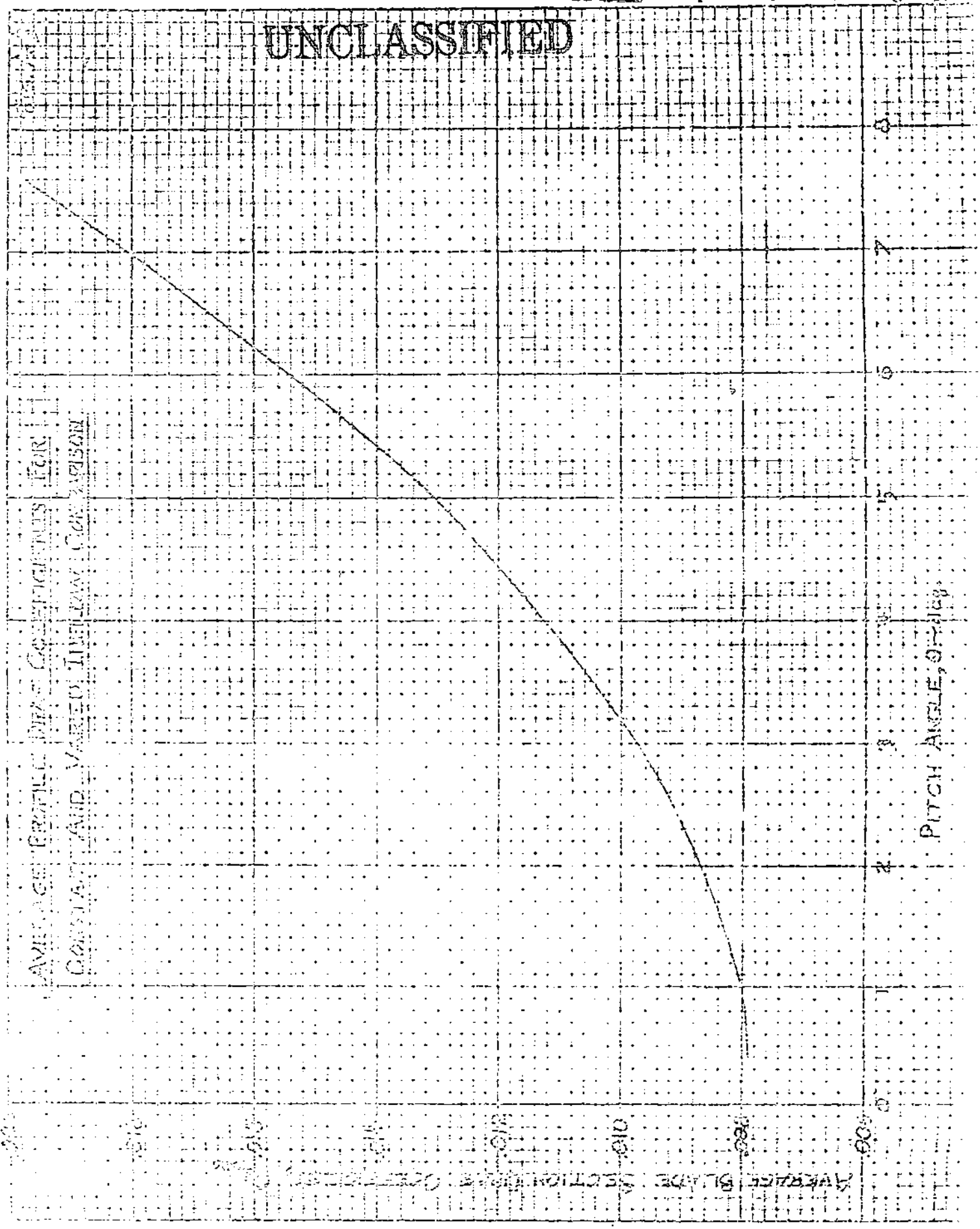


[redacted] UNCLASSIFIED

UNCLASSIFIED

FIG. A-4

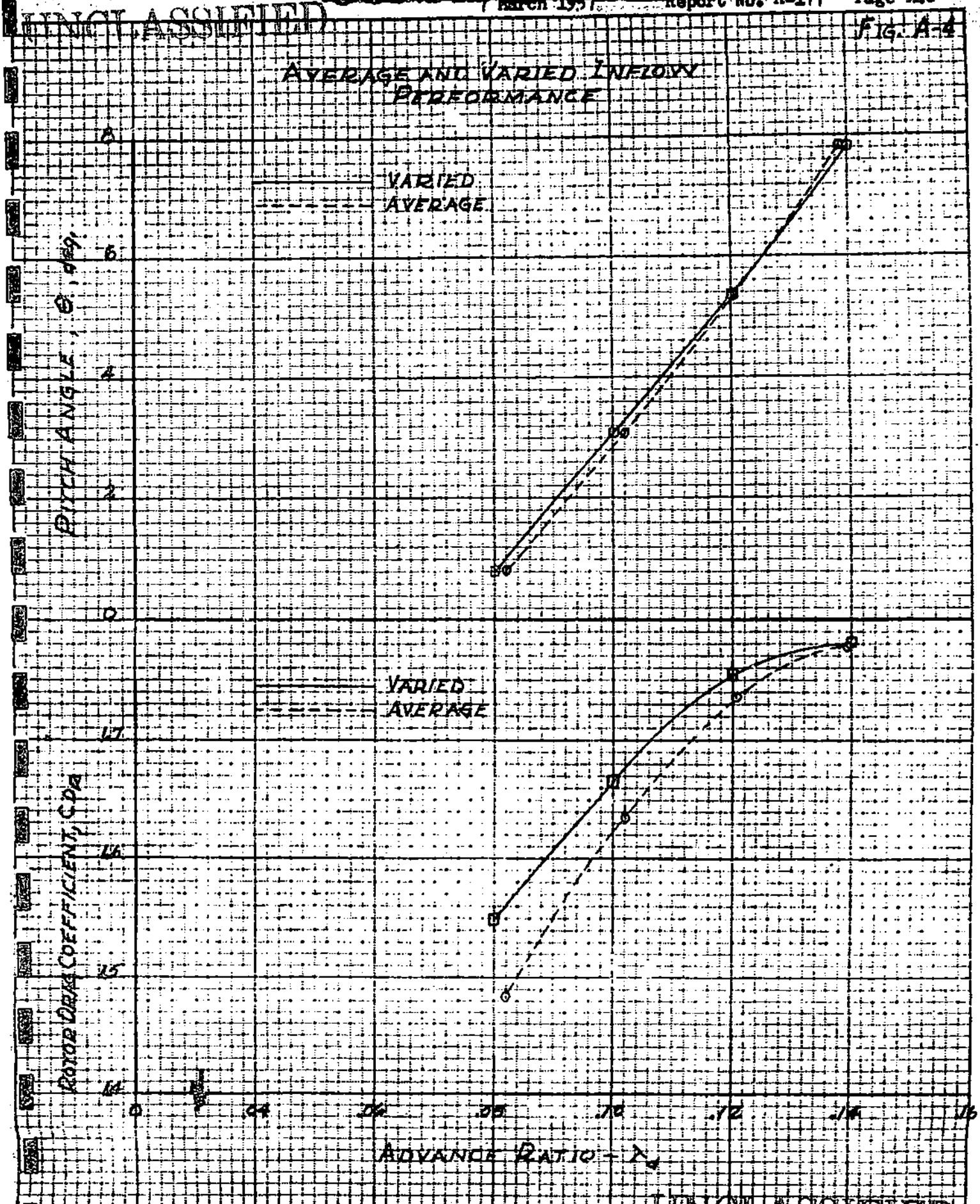


UNCLASSIFIED

[redacted]

0 0 0 5 3 5

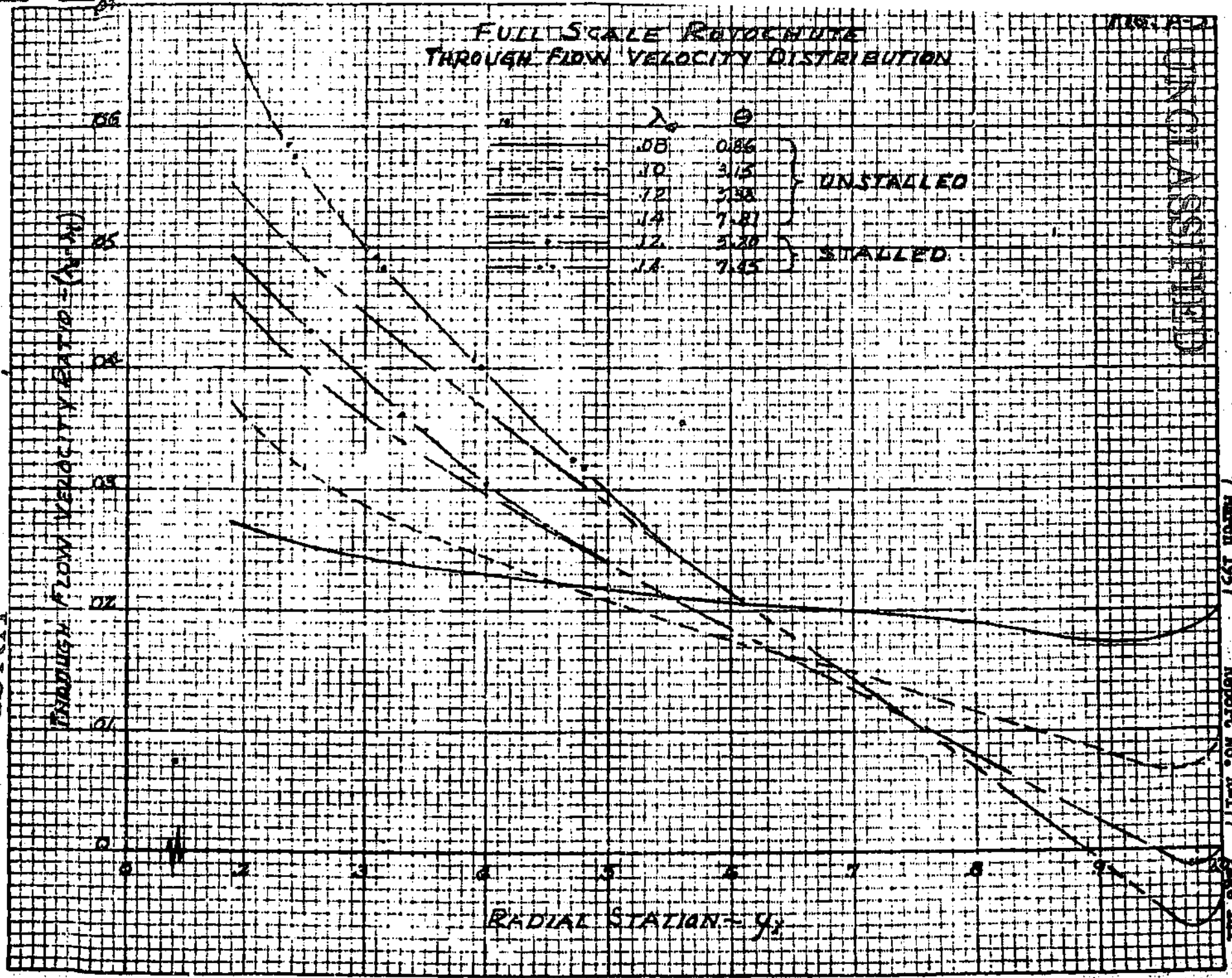


UNCLASSIFIED

UNCLASSIFIED

FIG. 14F

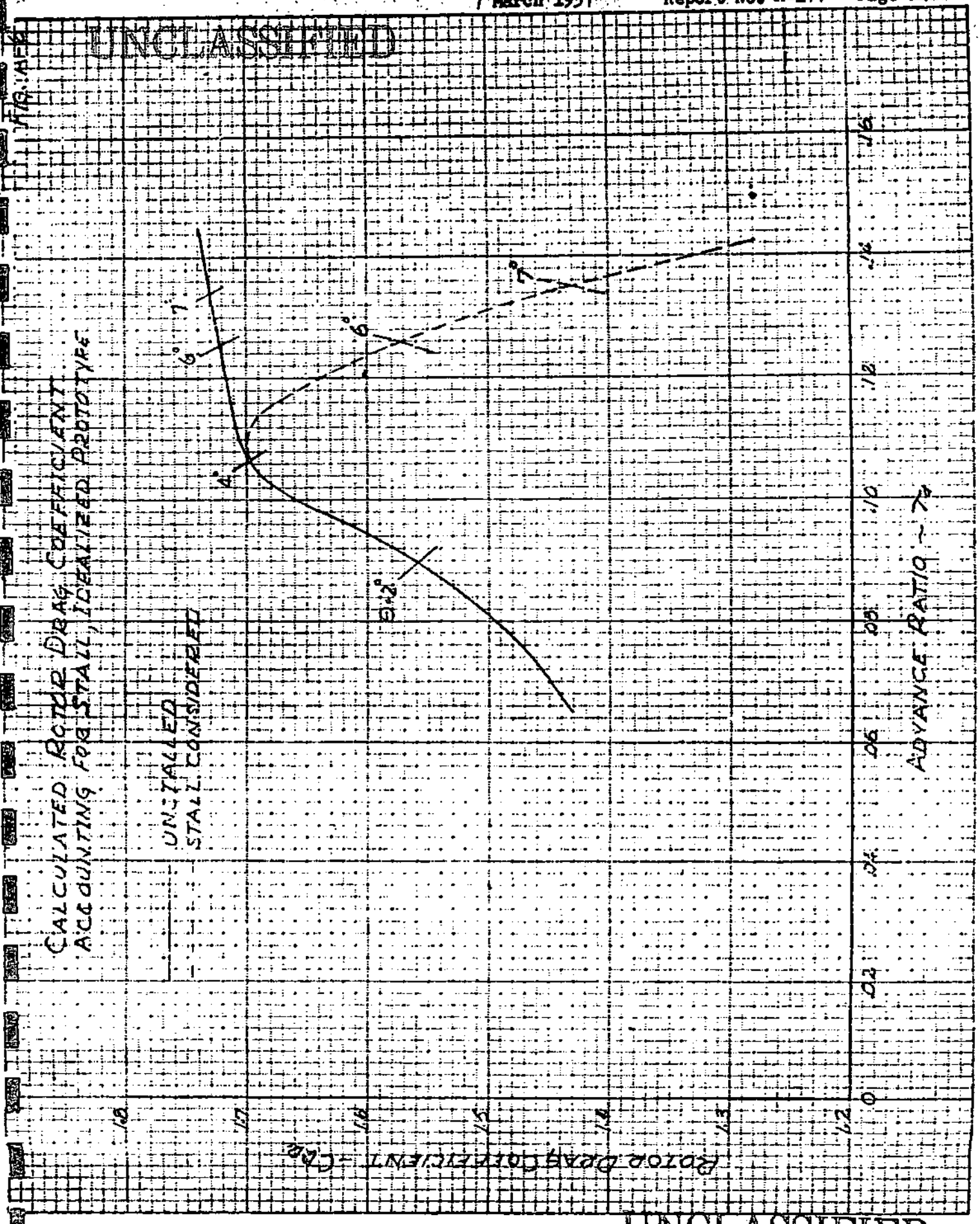

UNCLASSIFIED

FIG. A-7

COMPARISON OF CALCULATED AND EXPERIMENTAL ROTOR DRAG COEFFICIENT

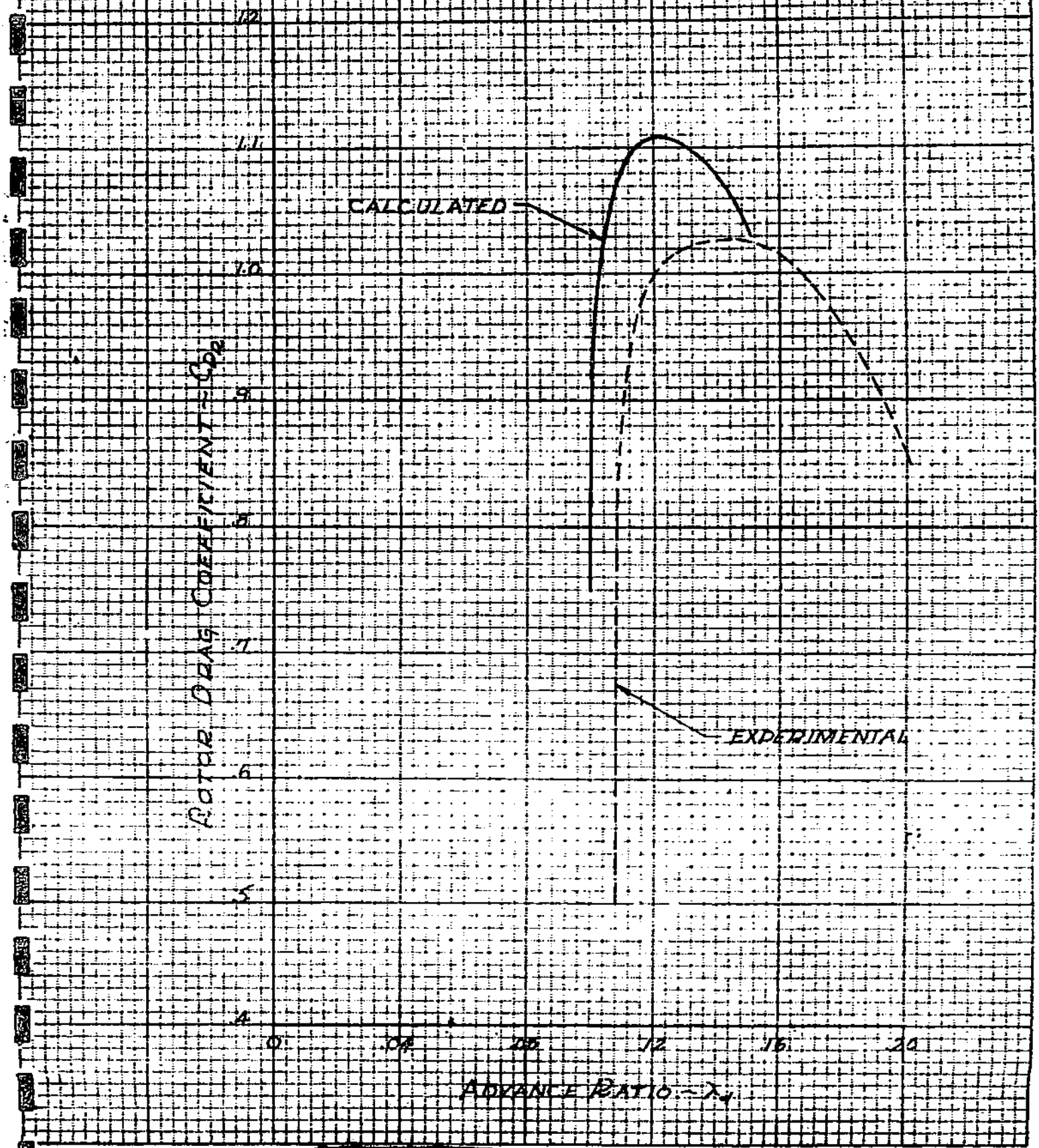

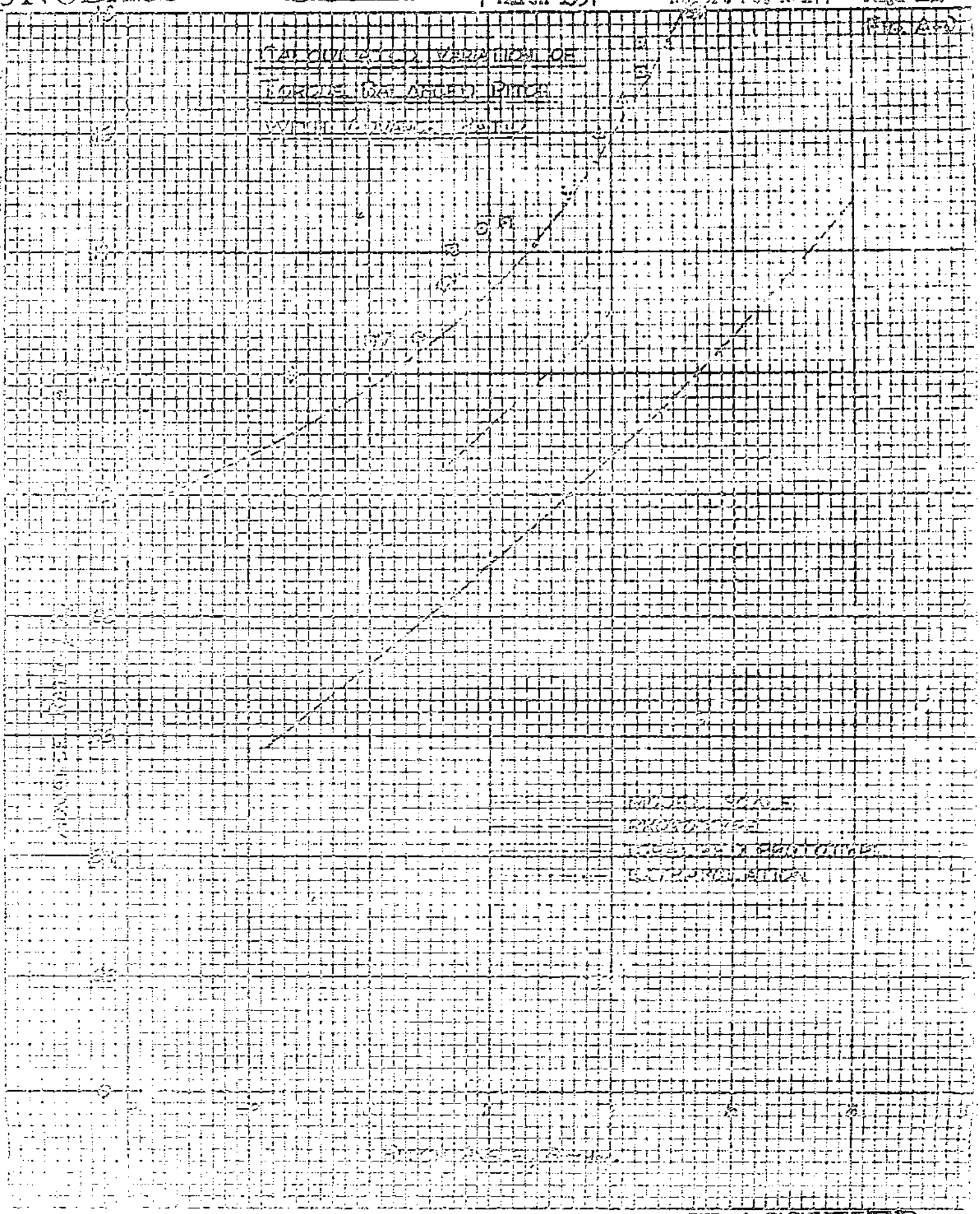
FIG. 4-7
INDUCED VERTICAL OF
FORCES ON ANGLED PINCH
WITH ROUNDED PARTS
MODEL SCALE
PROTOTYPE
INDUCED VERTICAL
EXPERIMENTAL

FIG. B-2

KAMAN ROTOCHUTE PERFORMANCE

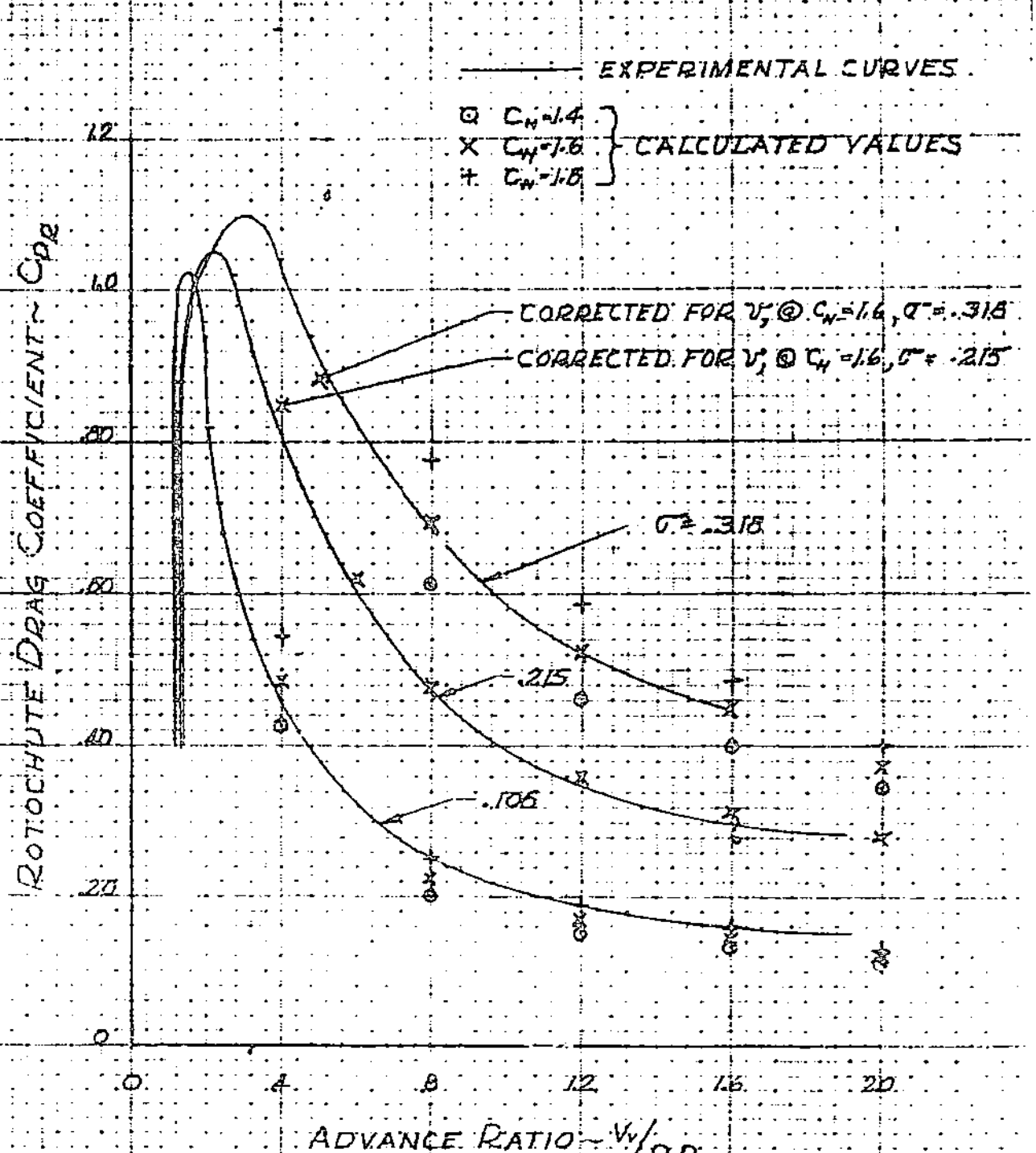

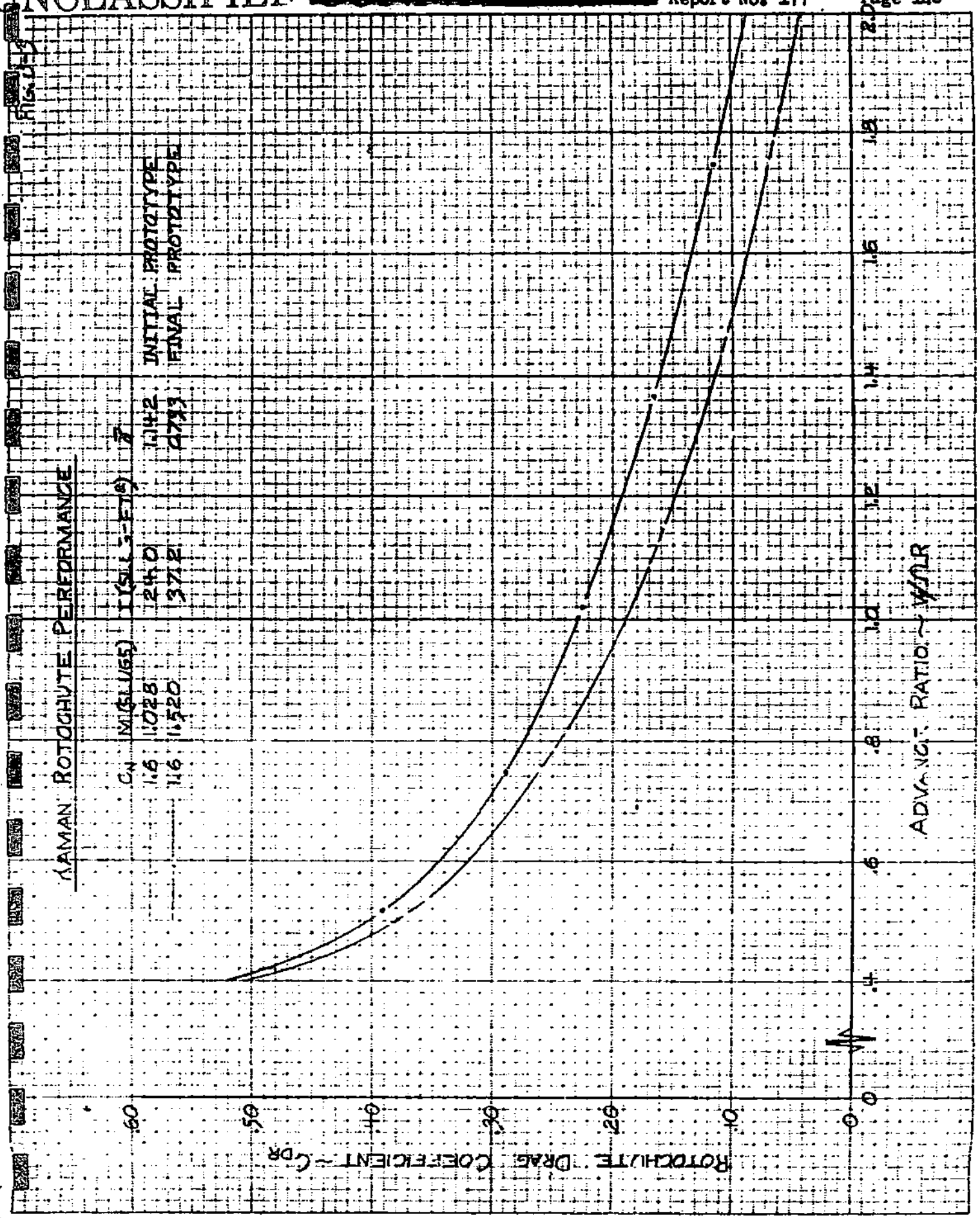
FIGURE 5
KAMAN ROTOCHUTE PERFORMANCE
$C_N$ M(SLUGS) I(SLUG-FT²) $\bar{\gamma}$
1.6 1.028 240 1.42 INITIAL PROTOTYPE
1.6 1.520 372 4.73 FINAL PROTOTYPE
ROTOCHUTE DRAG COEFFICIENT ~ $C_{DR}$
.60
.50
.40
.30
.20
.10
0
0
.4
.6
.8
1.0
1.2
1.4
1.6
1.8
2.0
ADVANCE RATIO ~ V/ΩR

UNCLASSIFIED

FIG. C-1

VARIATION OF STARTING TORQUE WITH DYNAMIC PRESSURE

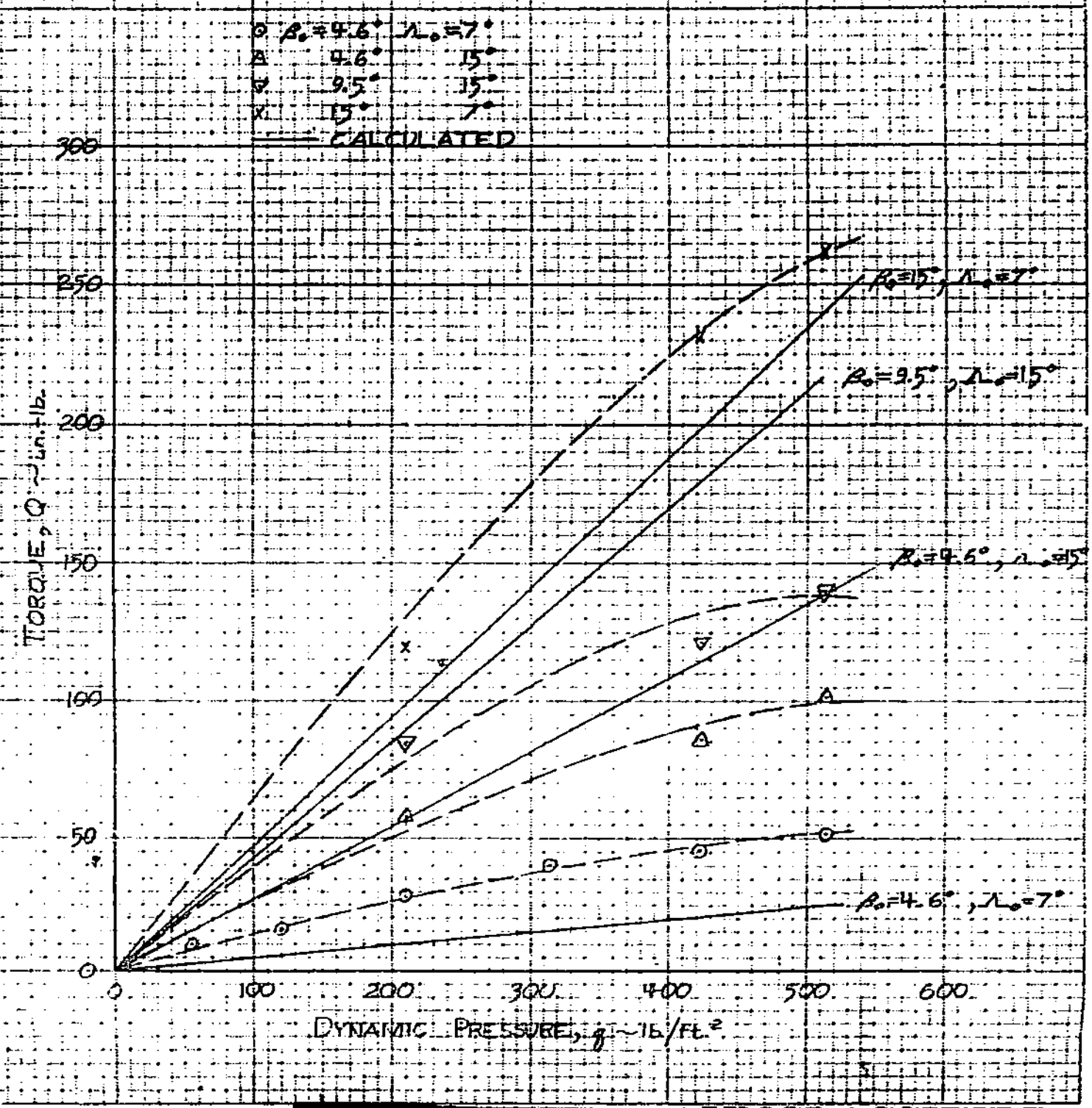


[redacted] UNCLASSIFIED

FIG. C-2

EFFECT OF BLADE TWIST AND BENDING ON STARTING TORQUE

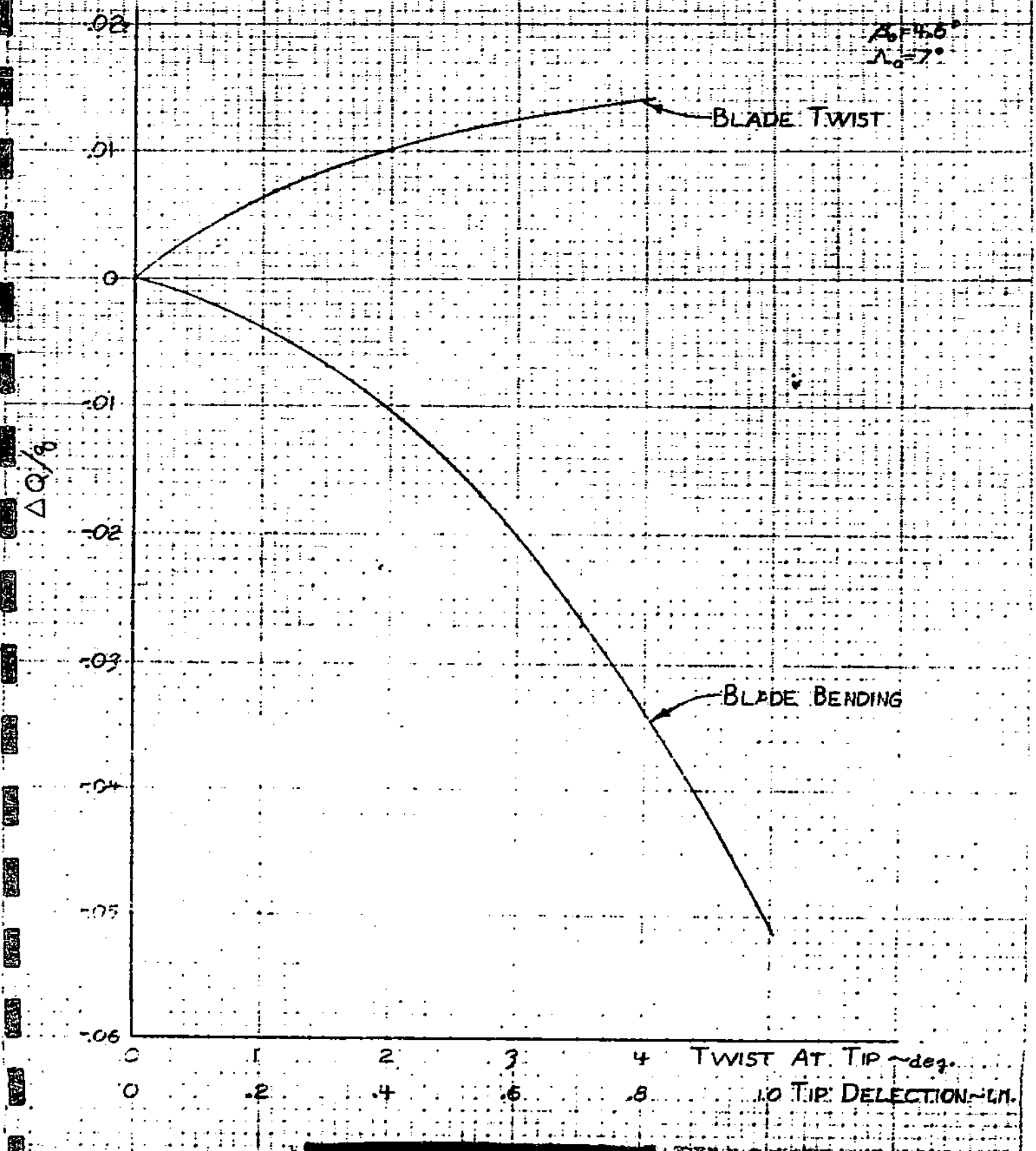

UNCLASSIFIED

Fig. C-3

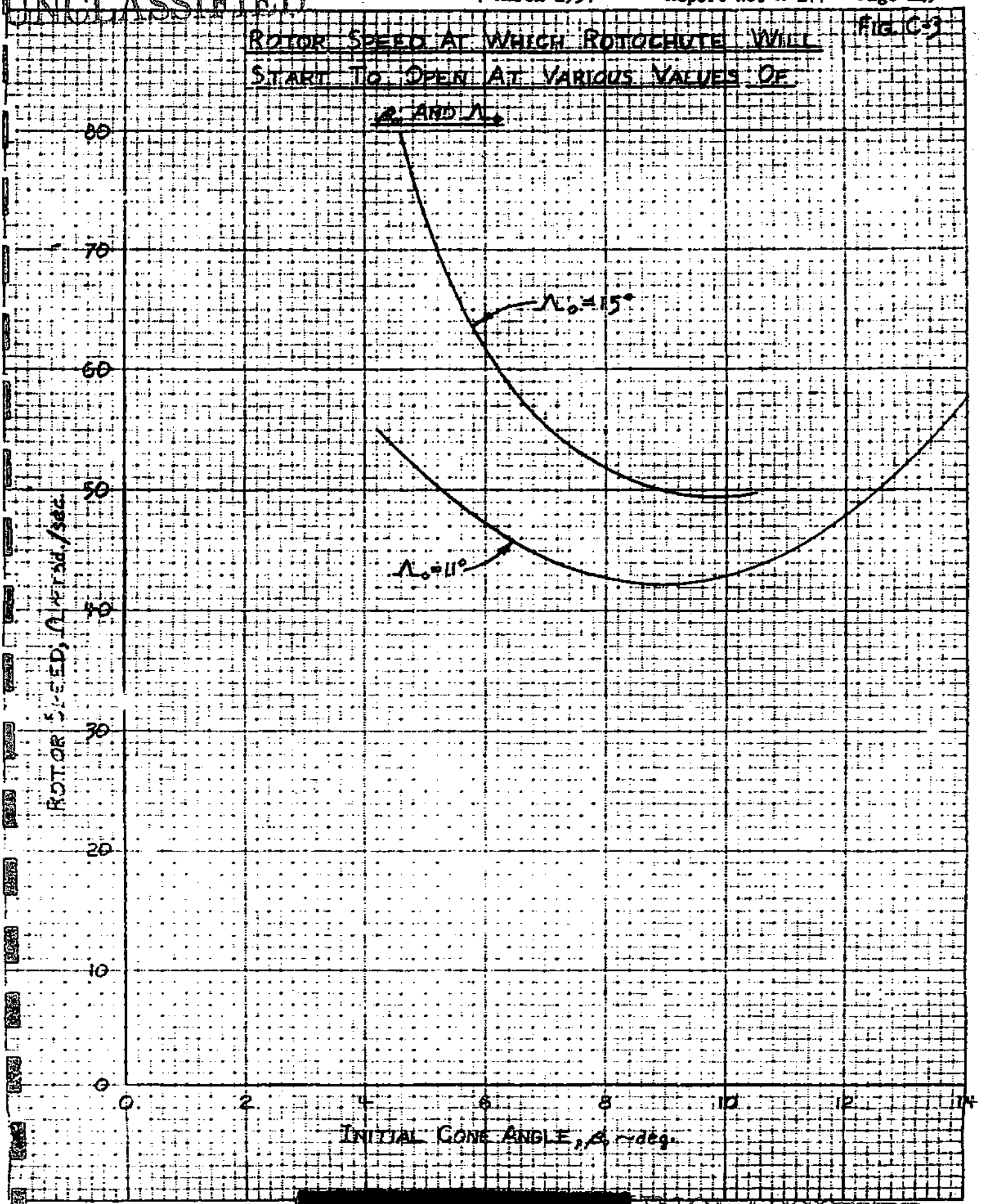

FIG. C-4

ROTOR SPEED AND TIME REQUIRED TO START ROTOCHUTE OPENING AT VARIOUS VALUES OF $\beta_0$ AND $\Lambda_0$

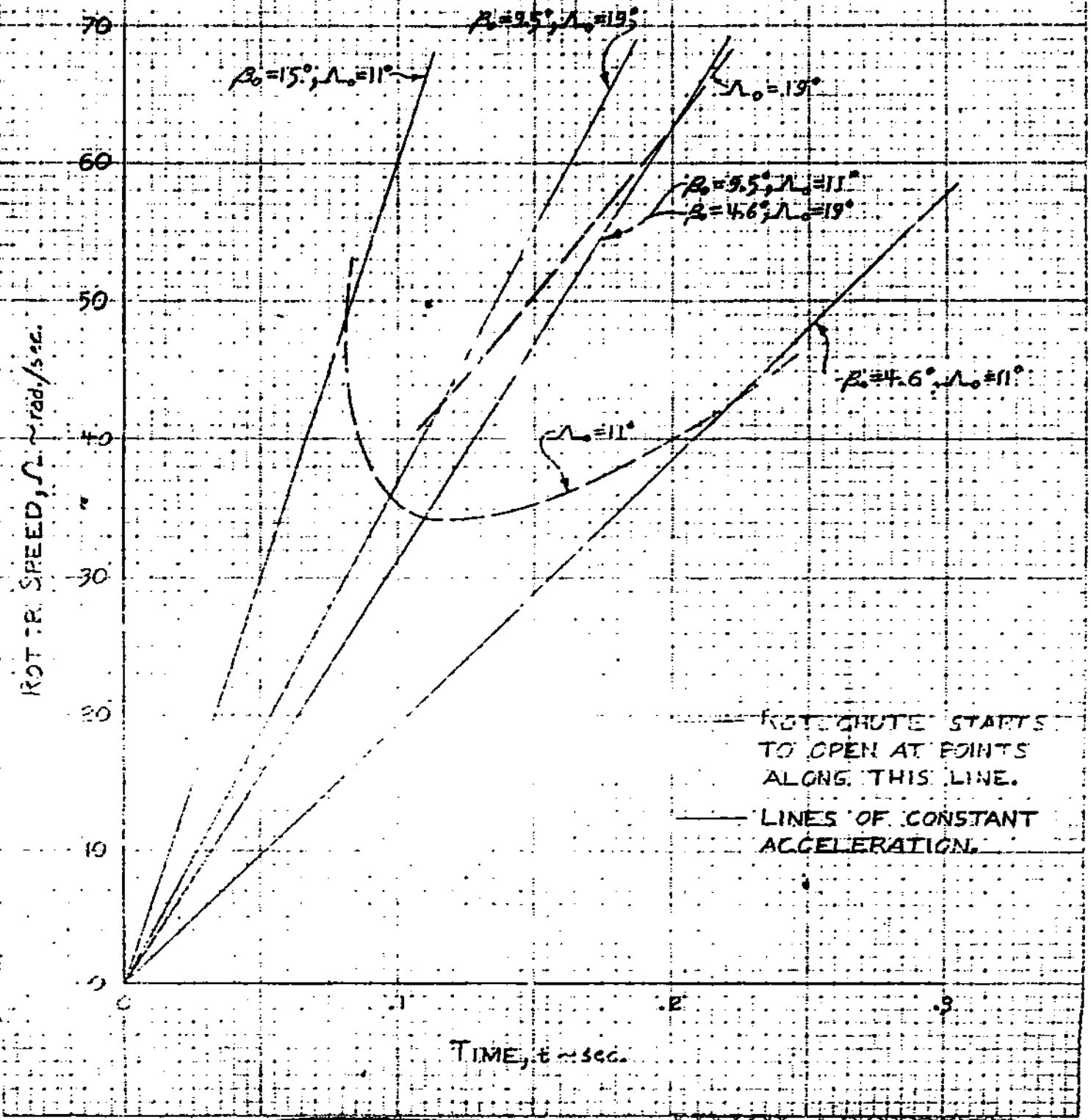

FIG. G-5

VARIATION OF STARTING TORQUE WITH INITIAL VALUES OF CONE AND SWEEP

UNCLASSIFIED

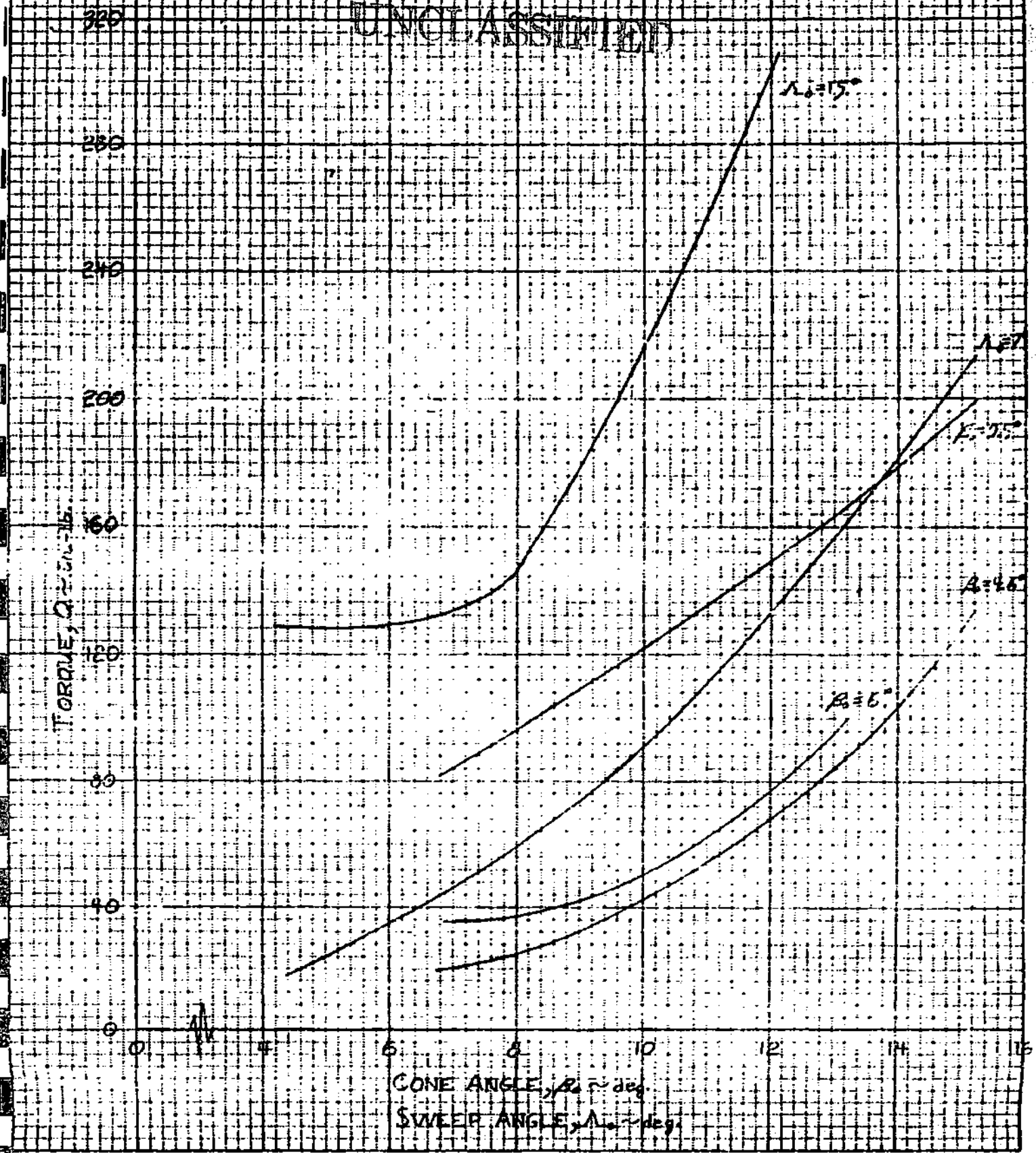


[redacted] UNCLASSIFIED

FIG. 66

ROTOCHUTE OPENING - TEST RESULTS

UNCLASSIFIED

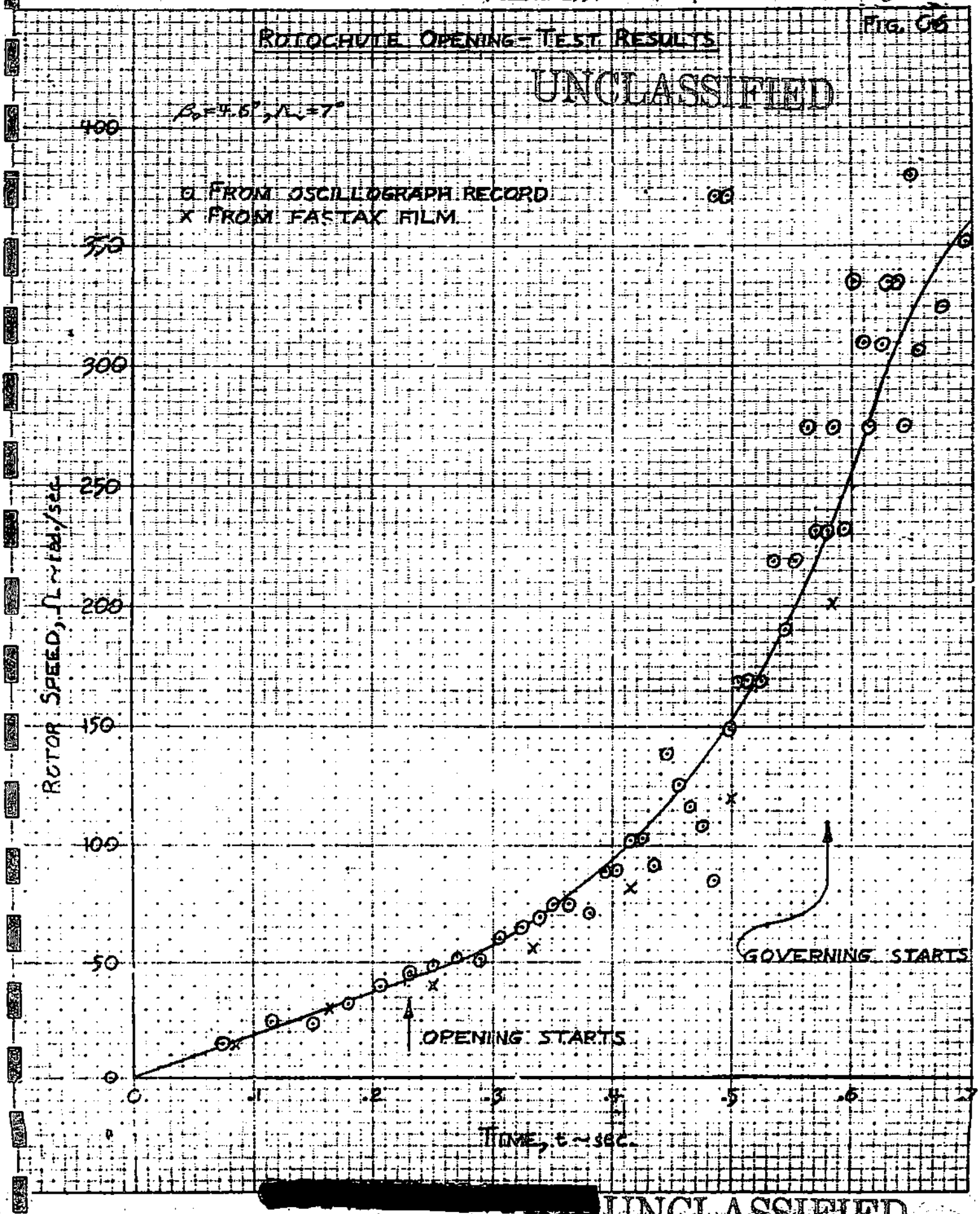




UNCLASSIFIED

FIG. C-7

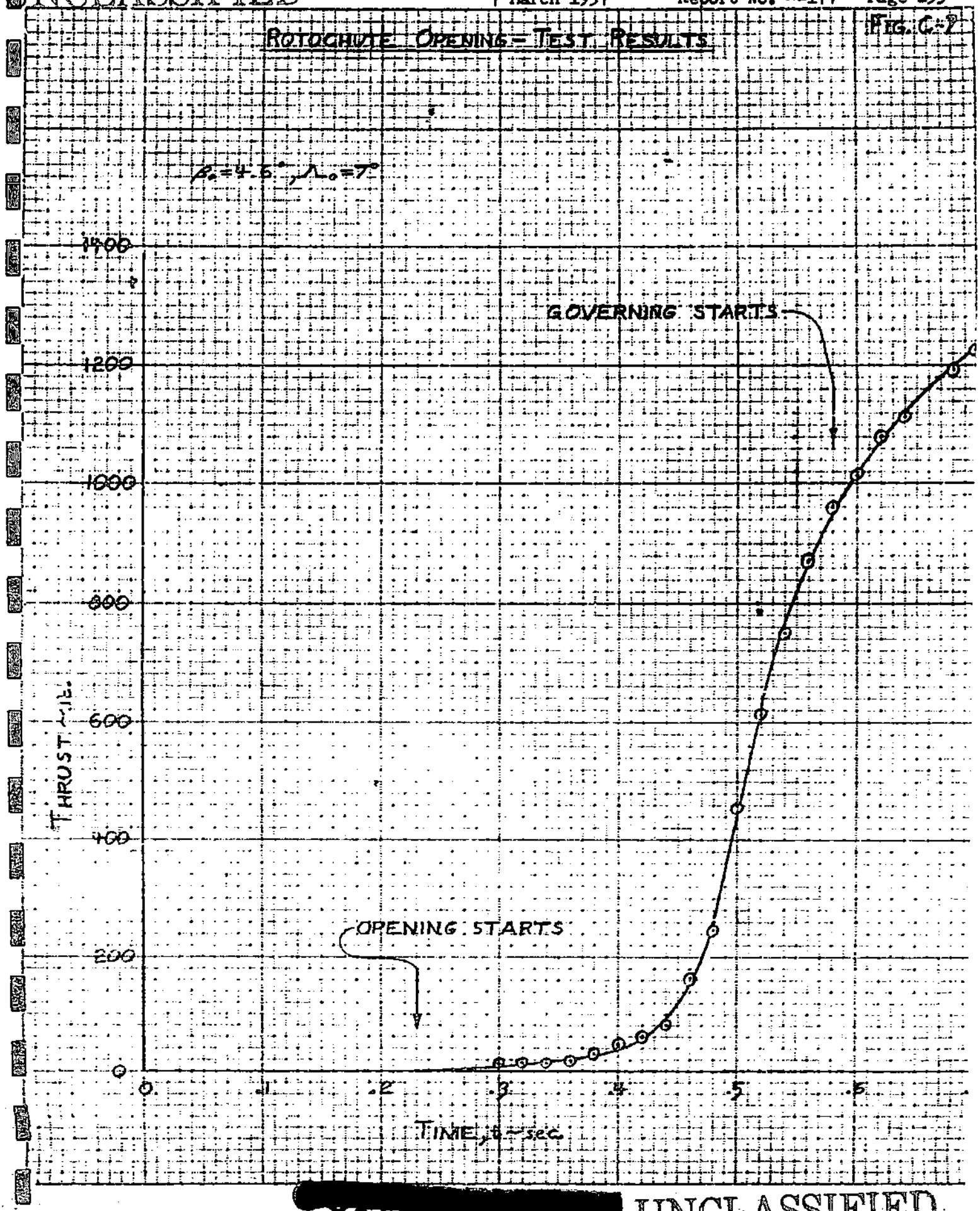
ROTOCHUTE OPENING – TEST RESULTS
$\beta_0 = 4.5°$, $\Lambda_0 = 7°$
GOVERNING STARTS
OPENING STARTS
THRUST ~ lb.
1400
1200
1000
800
600
400
200
0
0
.1
.2
.3
.4
.5
.6
TIME, t ~ sec.

FIG. C-8

ROTOCHUTE OPENING-TEST RESULTS

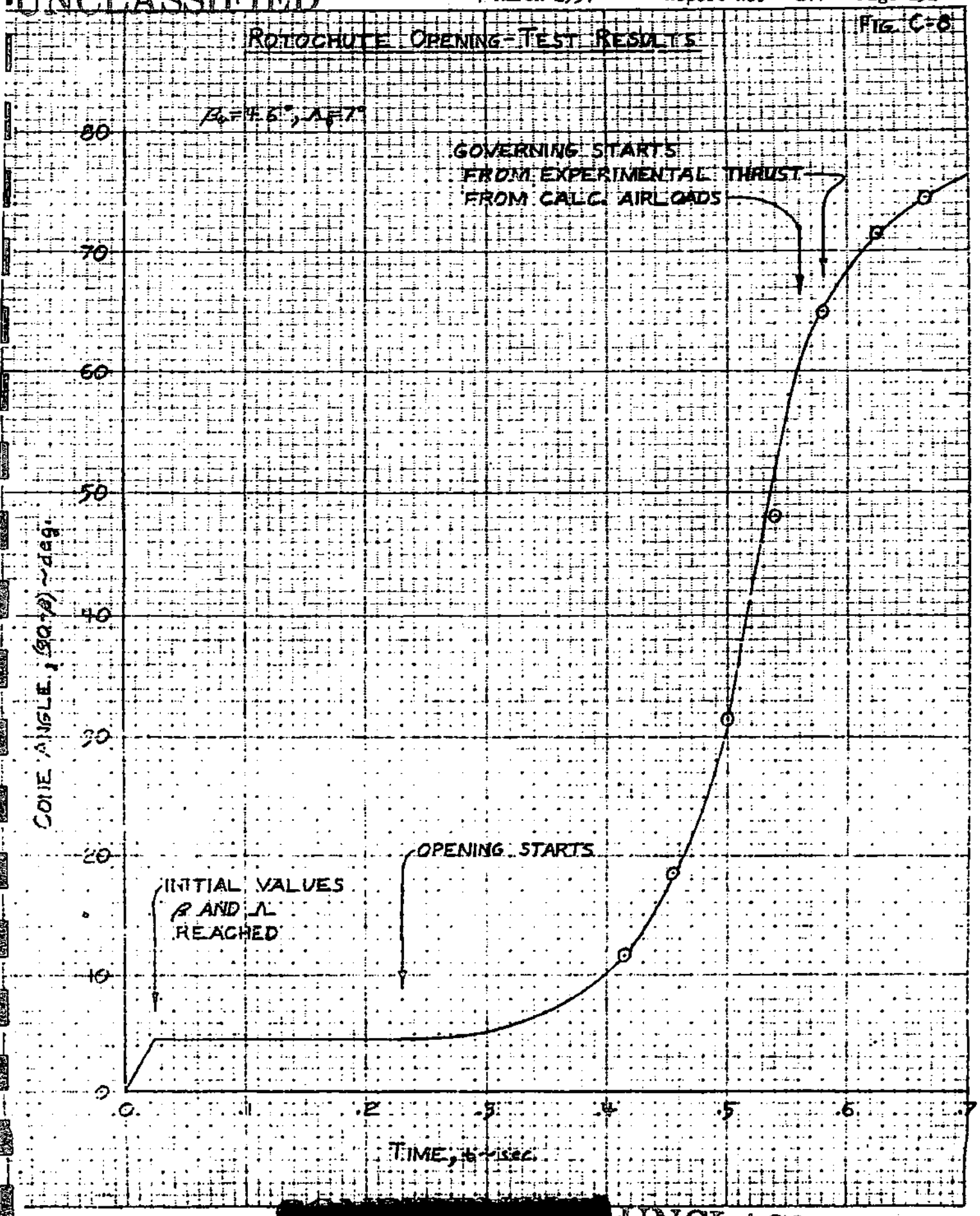

FIG. C-9

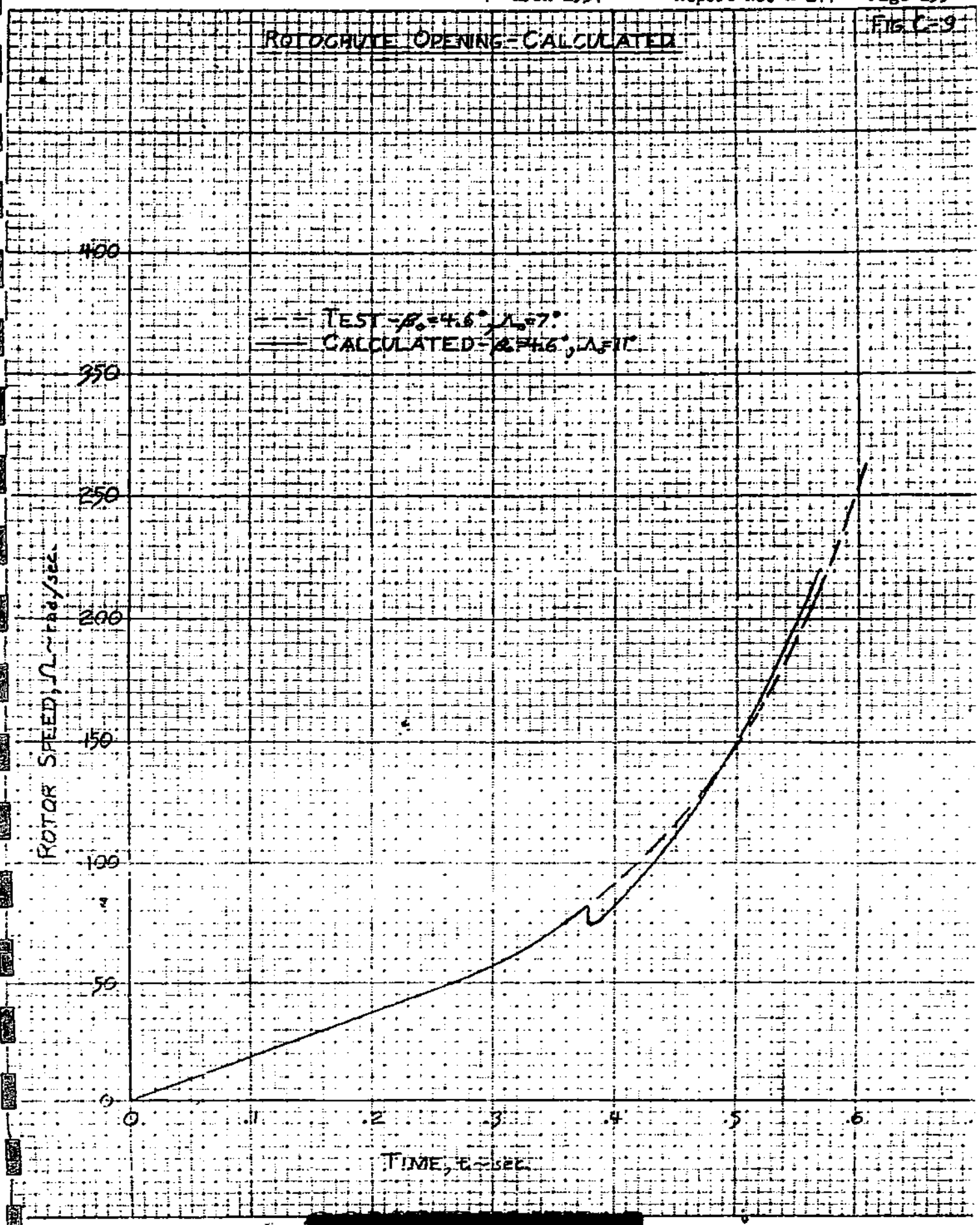
ROTOCHUTE OPENING - CALCULATED
--- TEST - $\beta_0$=4.6°, $\Lambda_0$=7°
—— CALCULATED - $\beta_0$=4.6°, $\Lambda_0$=11°
400
350
250
200
150
100
50
0
ROTOR SPEED, Ω ~ rad/sec
0
.1
.2
.3
.4
.5
.6
TIME, t ~ sec

FIG. G-10

ROTOCHUTE OPENING - CALCULATED

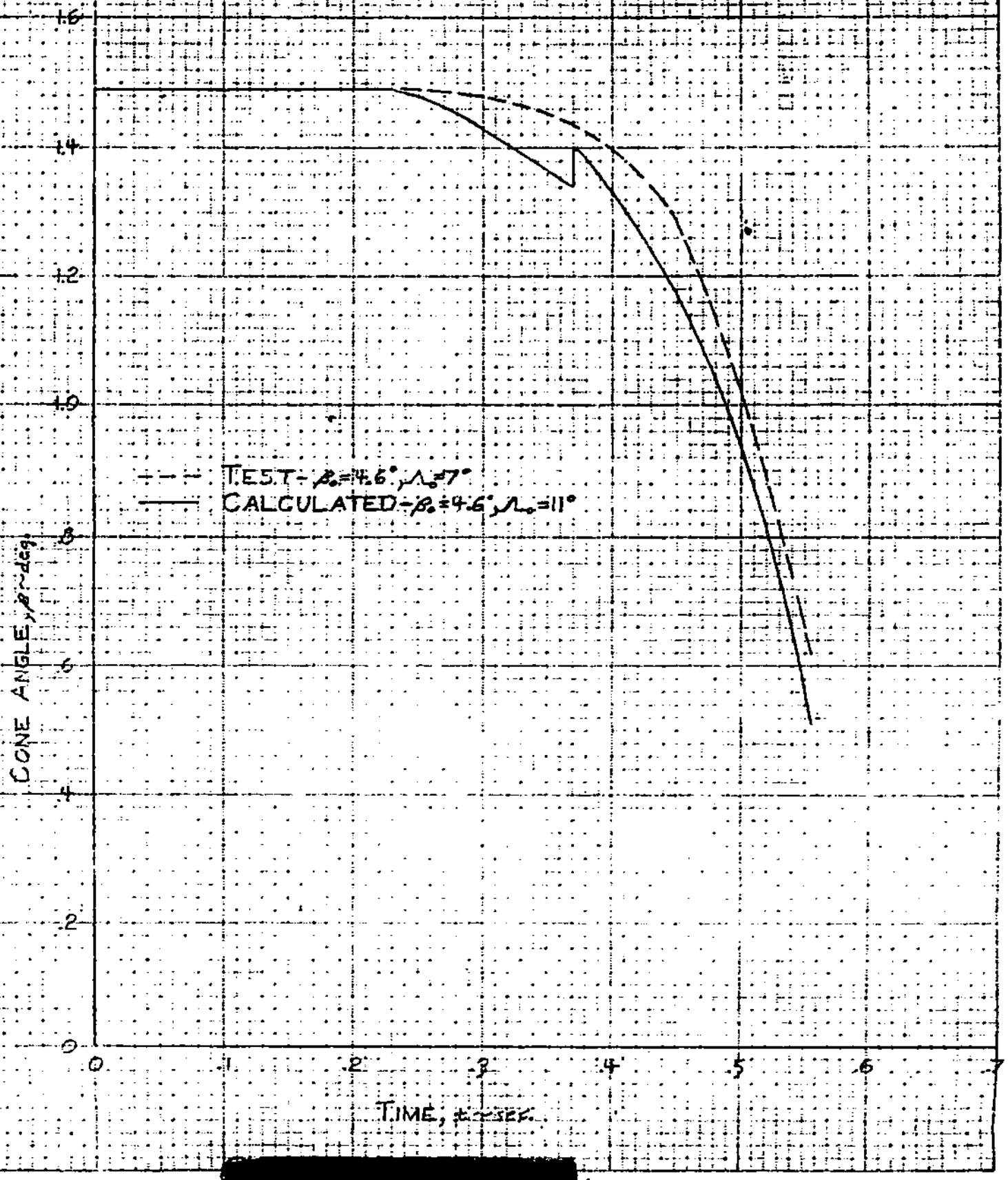


[redacted]

SCHEMATIC DIAGRAM OF GOVERNOR LINKAGE GEOMETRY

Figure D-1

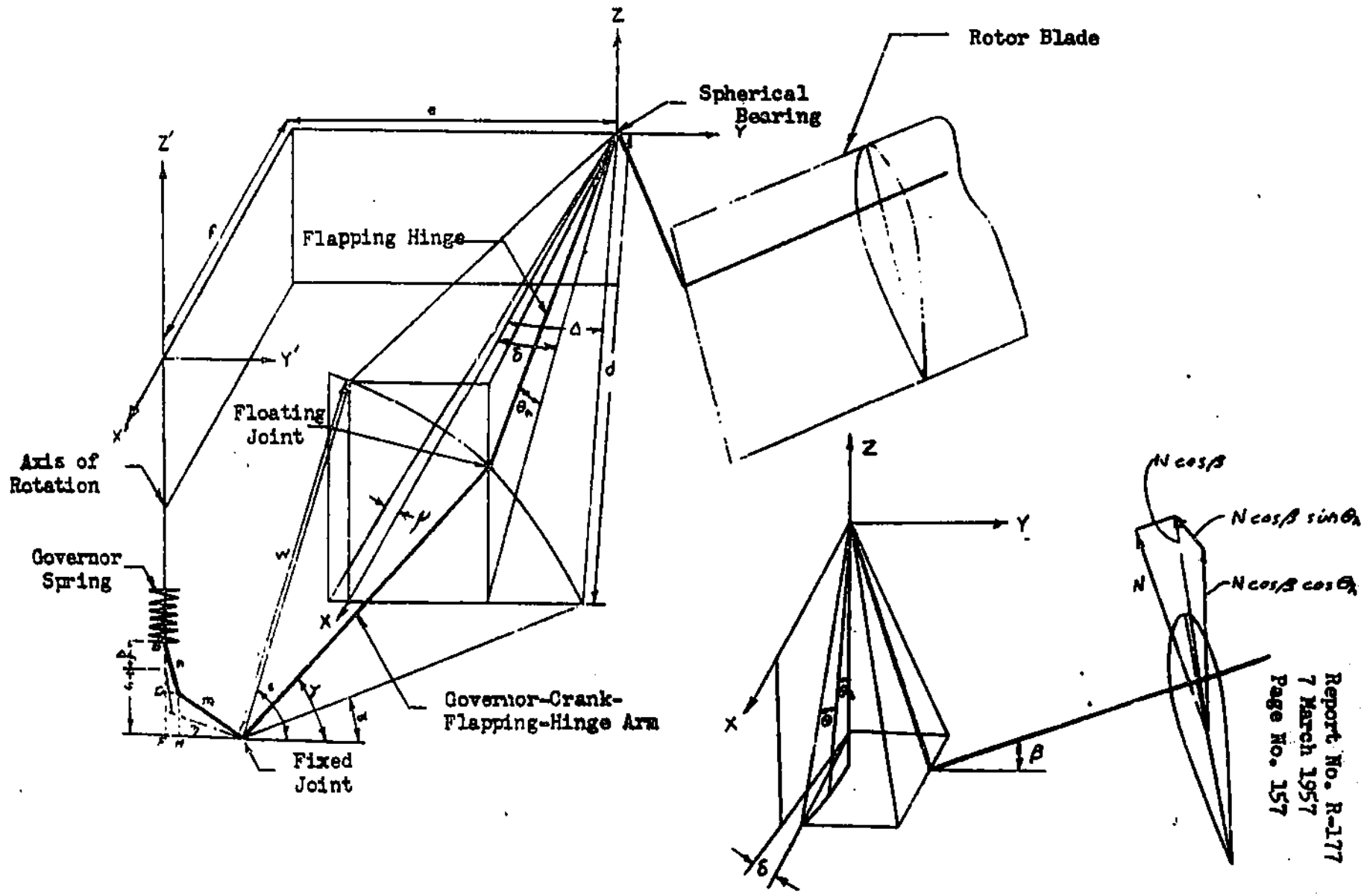

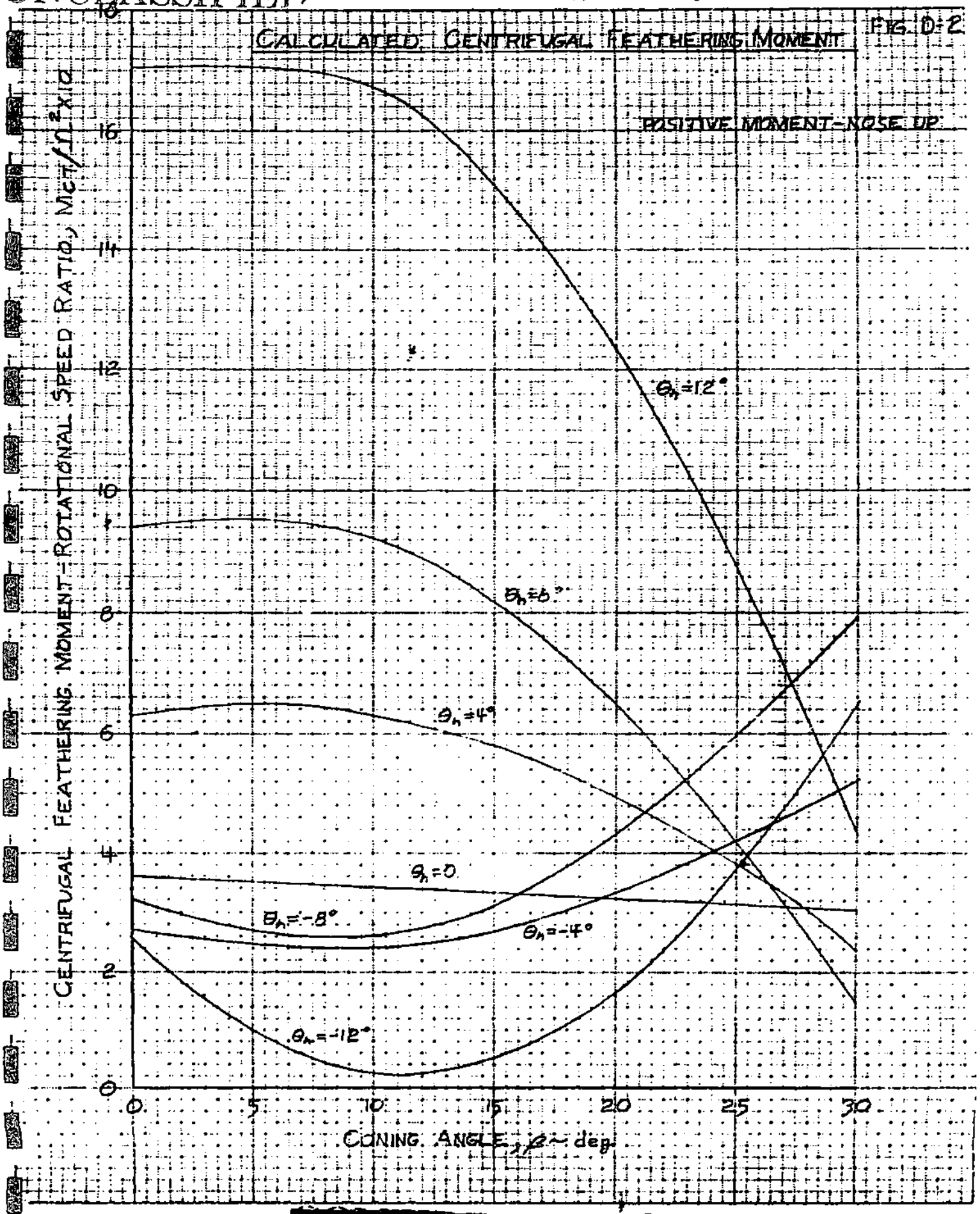
CALCULATED CENTRIFUGAL FEATHERING MOMENT
FIG. D-2
POSITIVE MOMENT-NOSE UP
CENTRIFUGAL FEATHERING MOMENT-ROTATIONAL SPEED RATIO, $M_{CF}/\Omega^2 x_{ia}$
CONING ANGLE, $\beta$ ~ deg
$\theta_h = 12°$
$\theta_h = 8°$
$\theta_h = 4°$
$\theta_h = 0$
$\theta_h = -8°$
$\theta_h = -4°$
$\theta_h = -12°$
0
2
4
6
8
10
12
14
16
18
0
5
10
15
20
25
30

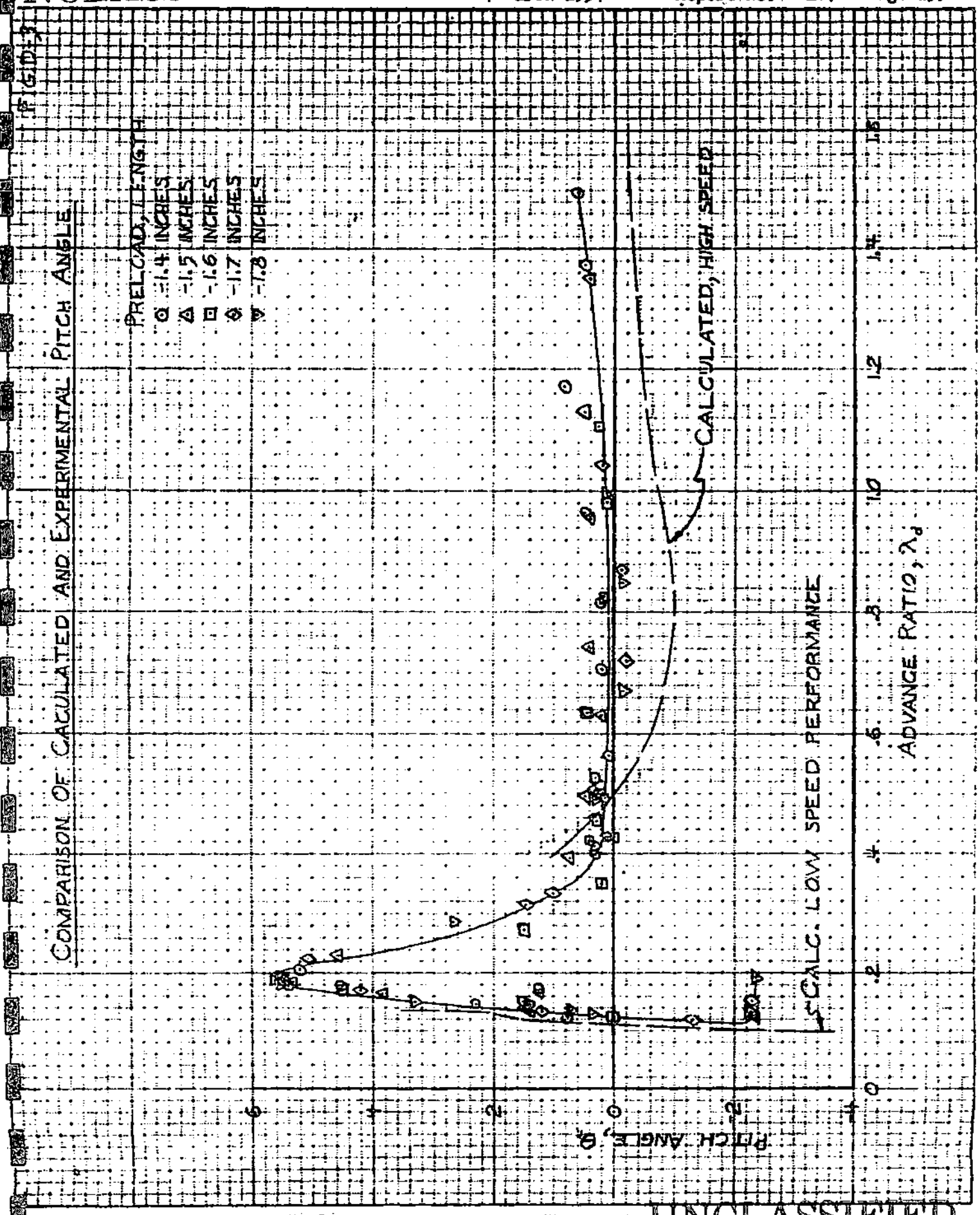
FIGURE 3
COMPARISON OF CALCULATED AND EXPERIMENTAL PITCH ANGLE
PRELOAD, LENGTH
-1.4 INCHES
-1.5 INCHES
-1.6 INCHES
-1.7 INCHES
-1.8 INCHES
CALCULATED, HIGH SPEED
CALC. LOW SPEED PERFORMANCE
PITCH ANGLE, θ
ADVANCE RATIO, λd
-6
-4
-2
0
2
4
0
.2
.4
.6
.8
1.0
1.2
1.4
1.6

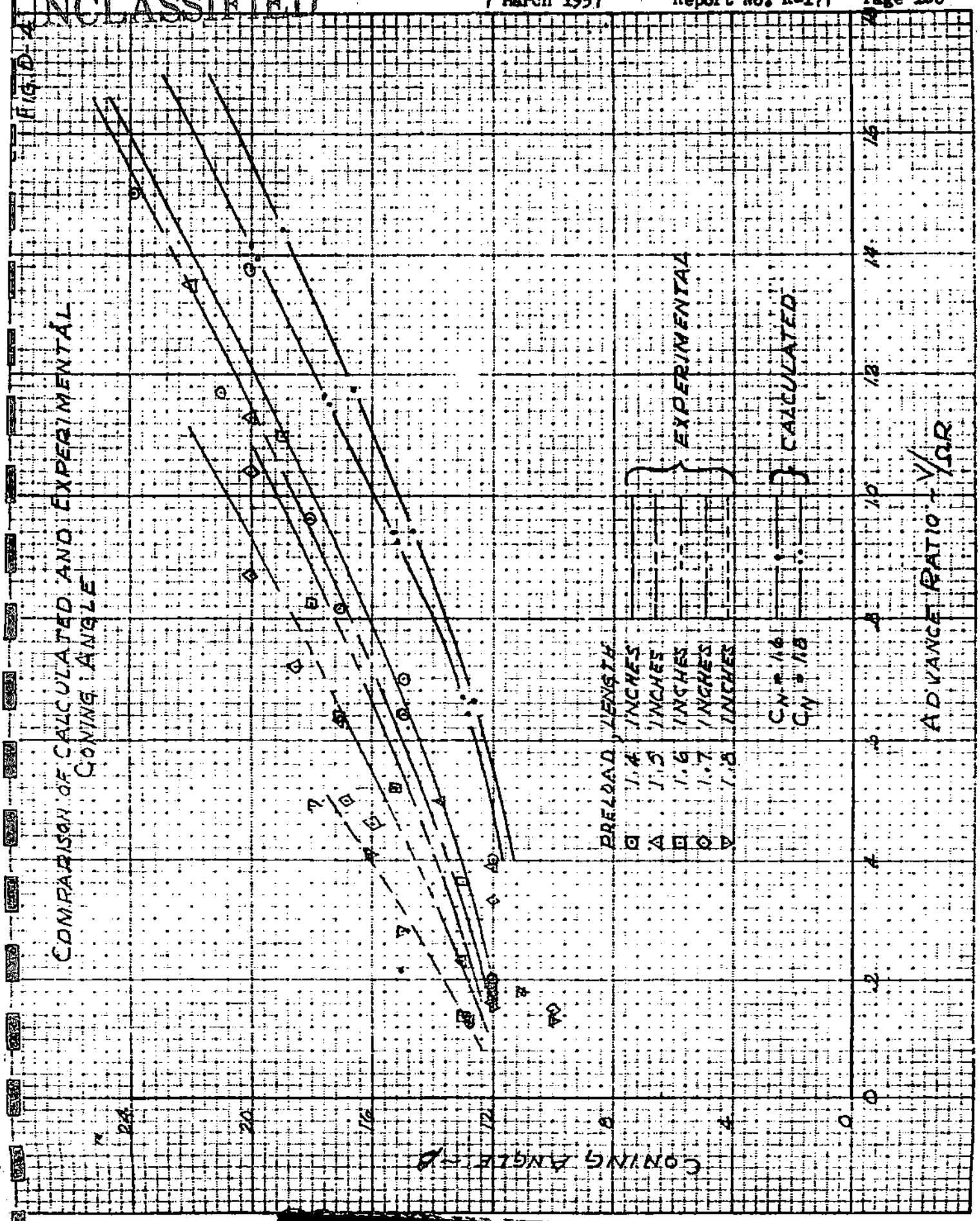
FIG. D-4
COMPARISON OF CALCULATED AND EXPERIMENTAL
CONING ANGLE
PRELOAD LENGTH
1.4 INCHES
1.5 INCHES
1.6 INCHES
1.7 INCHES
1.8 INCHES
EXPERIMENTAL
CALCULATED
CN = .16
CN = .18
ADVANCE RATIO - V/ΩR
CONING ANGLE - β
0
2
4
6
8
10
12
14
16
18
20
22
24

FIG. D-5

COMPARISON OF EXPERIMENTAL AND CALCULATED AERODYNAMIC FEATHERING MOMENT

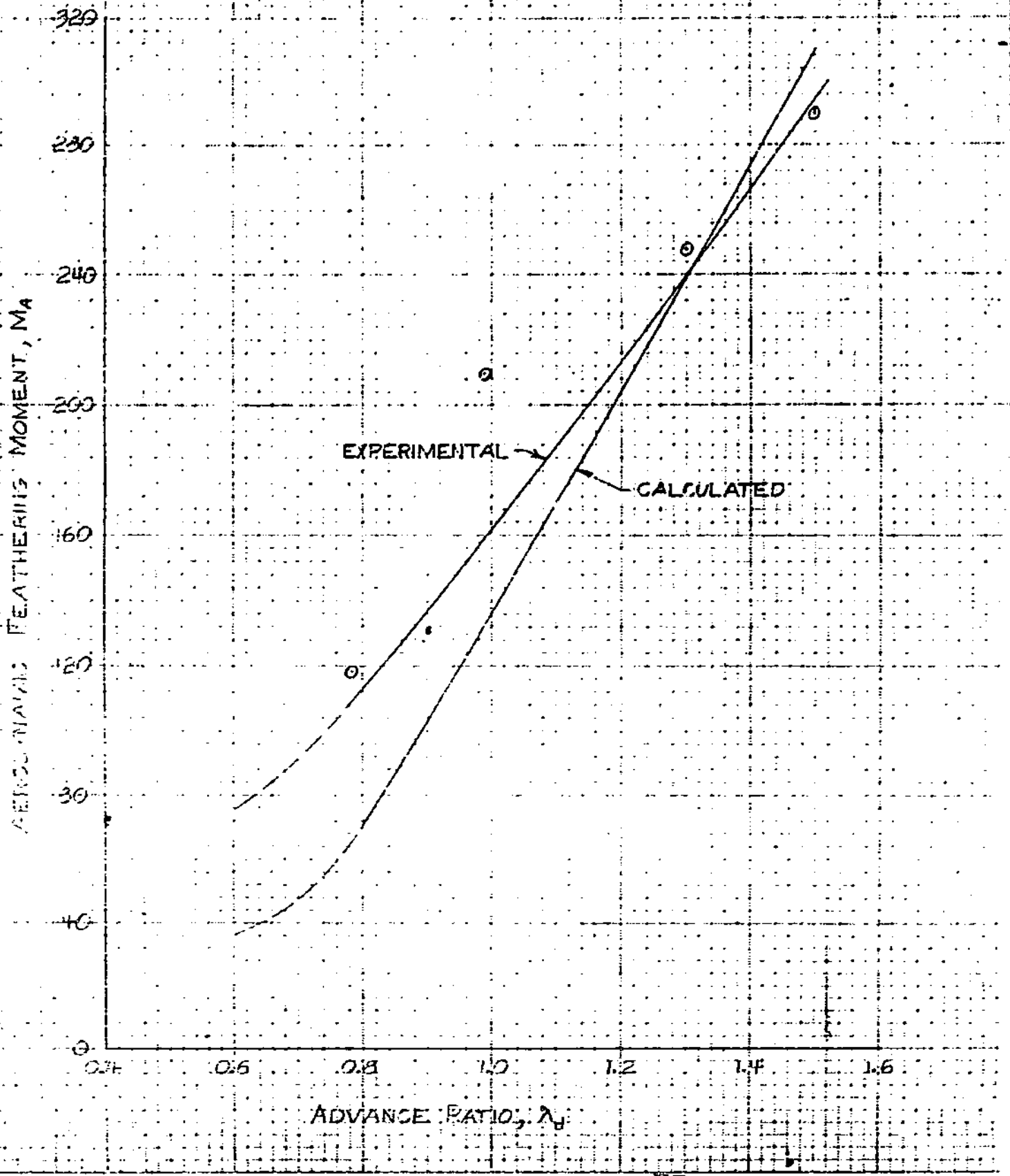

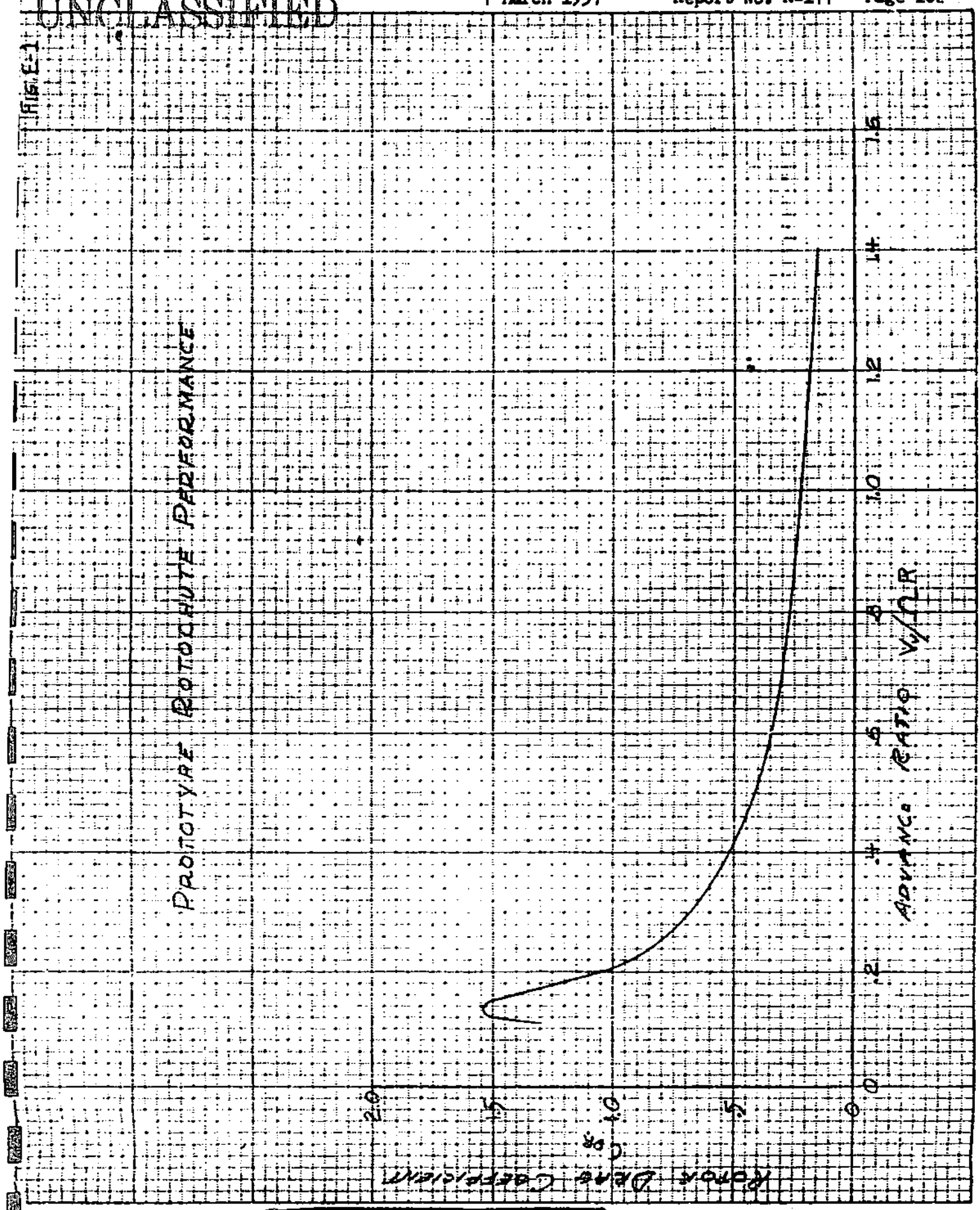
FIG. E-1
PROTOTYPE ROTOCHUTE PERFORMANCE
ADVANCE RATIO V/ΩR
0
.2
.4
.6
.8
1.0
1.2
1.4
1.6
DRAG COEFFICIENT
0
.5
1.0
1.5
2.0

UNCLASSIFIED

FIG. E-2

ROTOR TIP SPEED VARIATION WITH VELOCITY

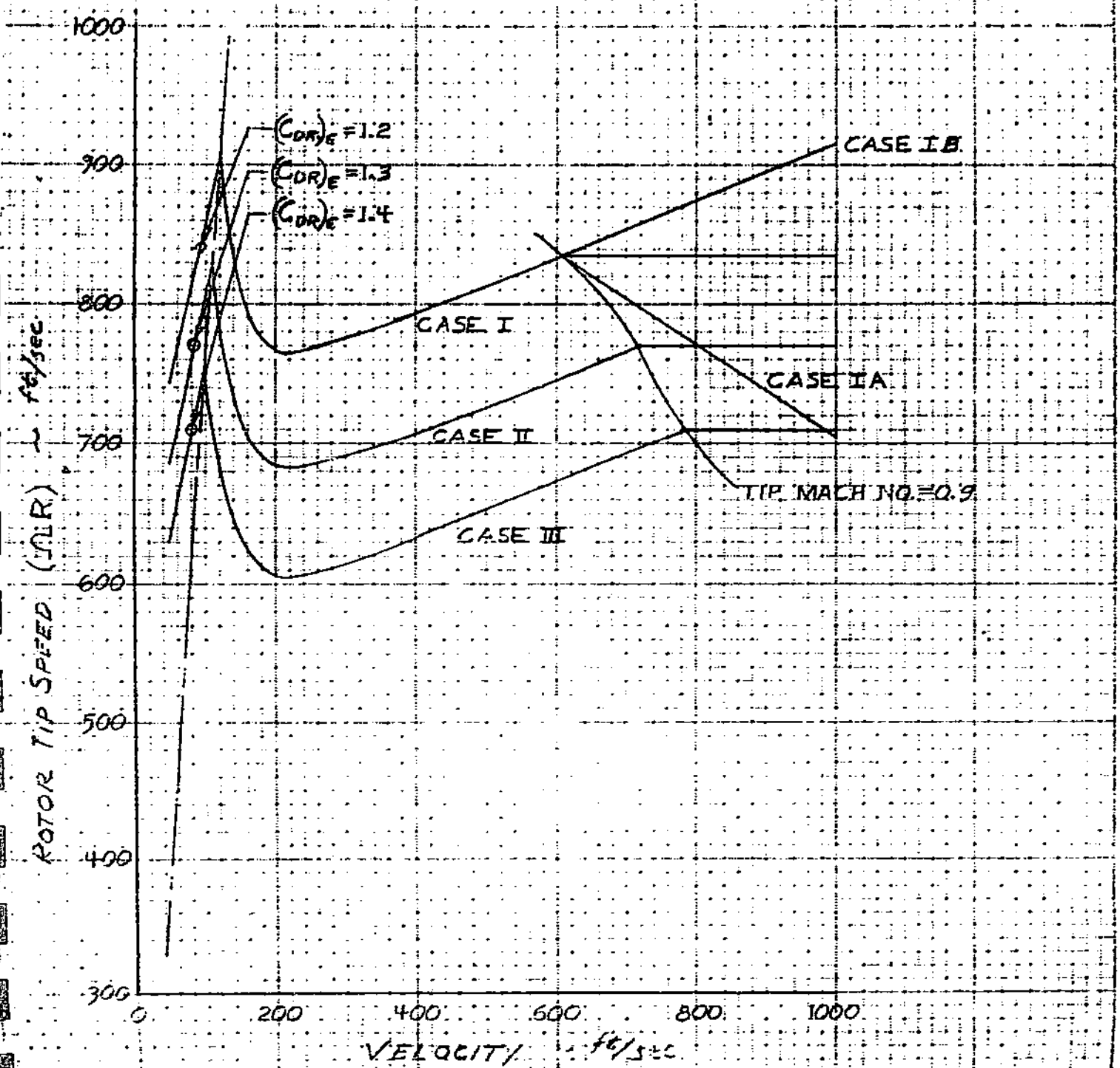


[redacted]

UNCLASSIFIED

FIG. E-3

LIMIT TIP SPEED AND TERMINAL VELOCITY VARIATION WITH ROTOR DRAG COEFFICIENT IN TERMINAL DESCENT

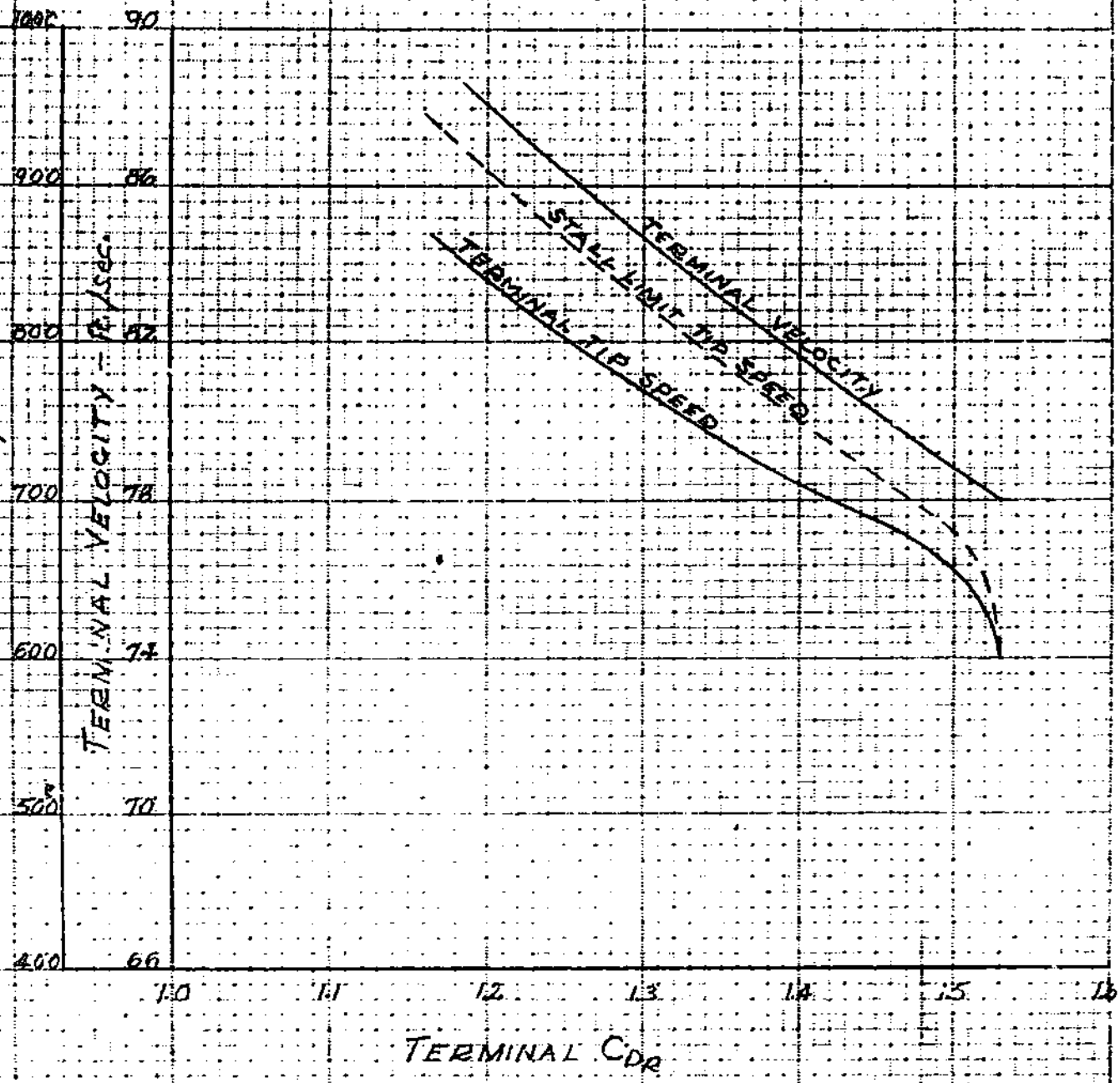

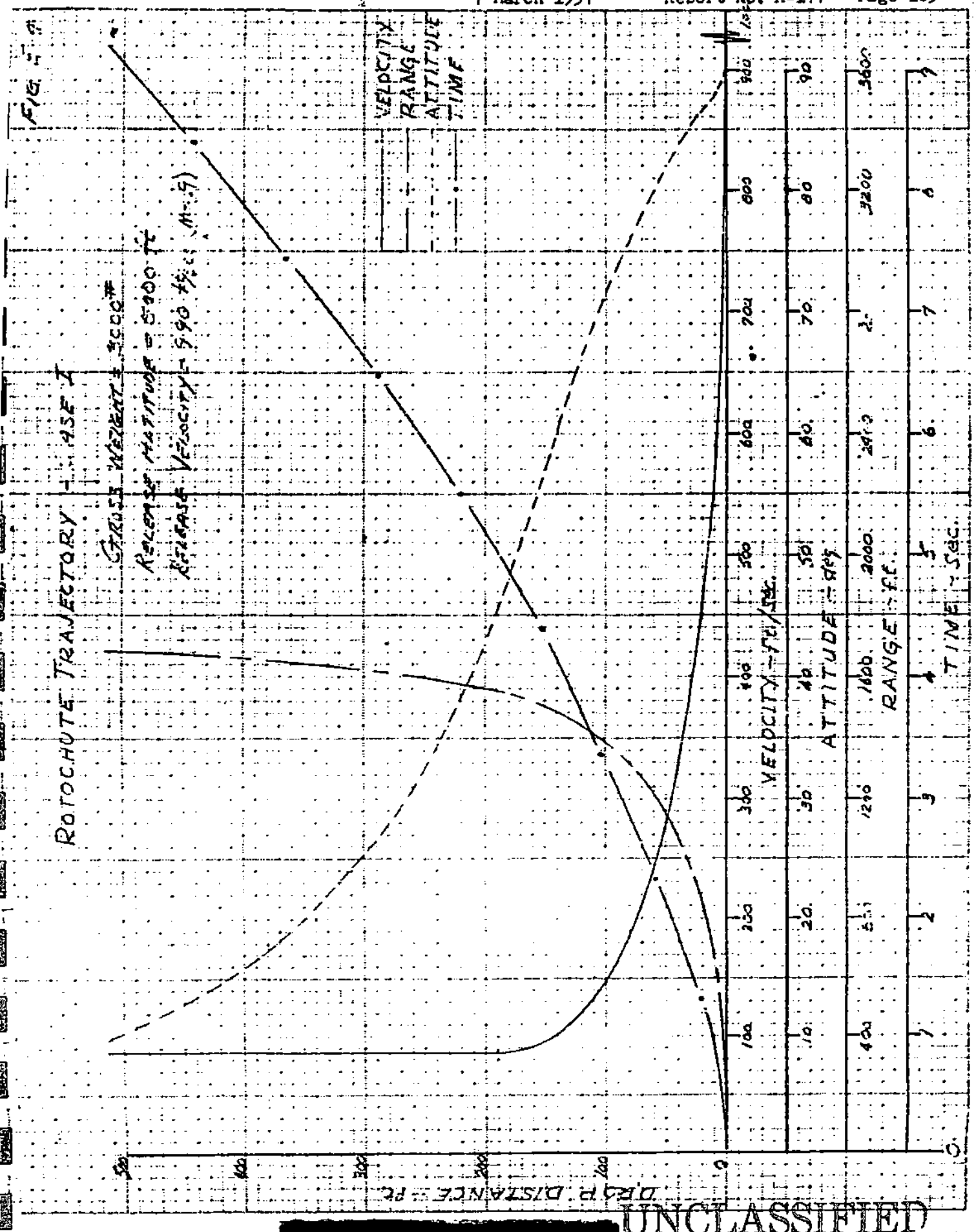
FIG. 7
ROTOCHUTE TRAJECTORY
GROSS WEIGHT = 3000 #
RELEASE ALTITUDE = 5000 ft
RELEASE VELOCITY = 590 ft/sec (M=.9)
VELOCITY
RANGE
ALTITUDE
TIME
VELOCITY ~ ft/sec
ALTITUDE ~ deg
RANGE ~ ft
TIME ~ sec
DRAG DISTANCE ~ ft

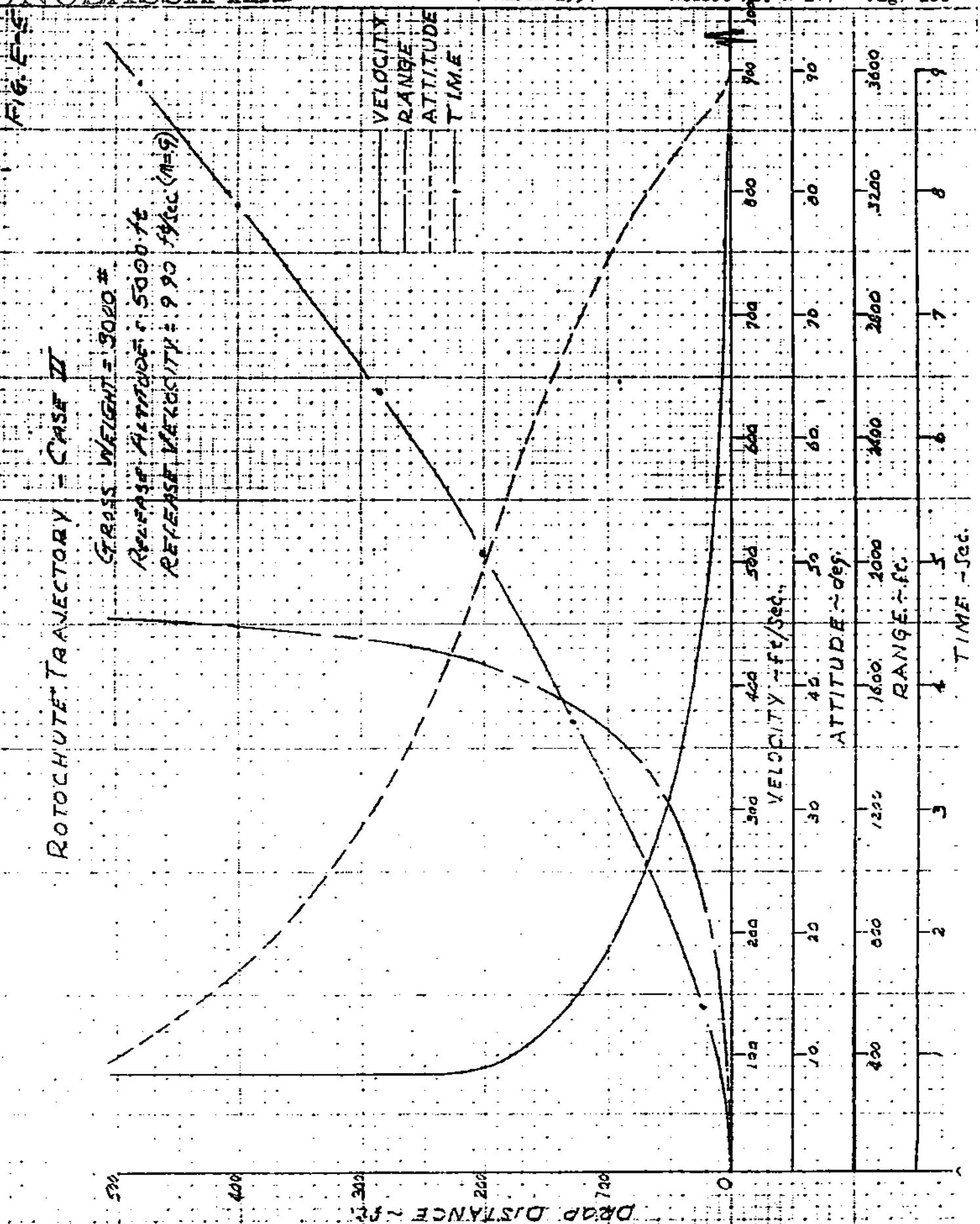
FIG. E-5
ROTOCHUTE TRAJECTORY - CASE III
GROSS WEIGHT = 3000 #
RELEASE ALTITUDE = 5000 ft
RELEASE VELOCITY = 990 ft/sec (M=9)
VELOCITY
RANGE
ATTITUDE
TIME
DRAG DISTANCE ~ ft.
VELOCITY ~ ft/sec.
ATTITUDE ~ deg.
RANGE ~ ft.
TIME ~ sec.

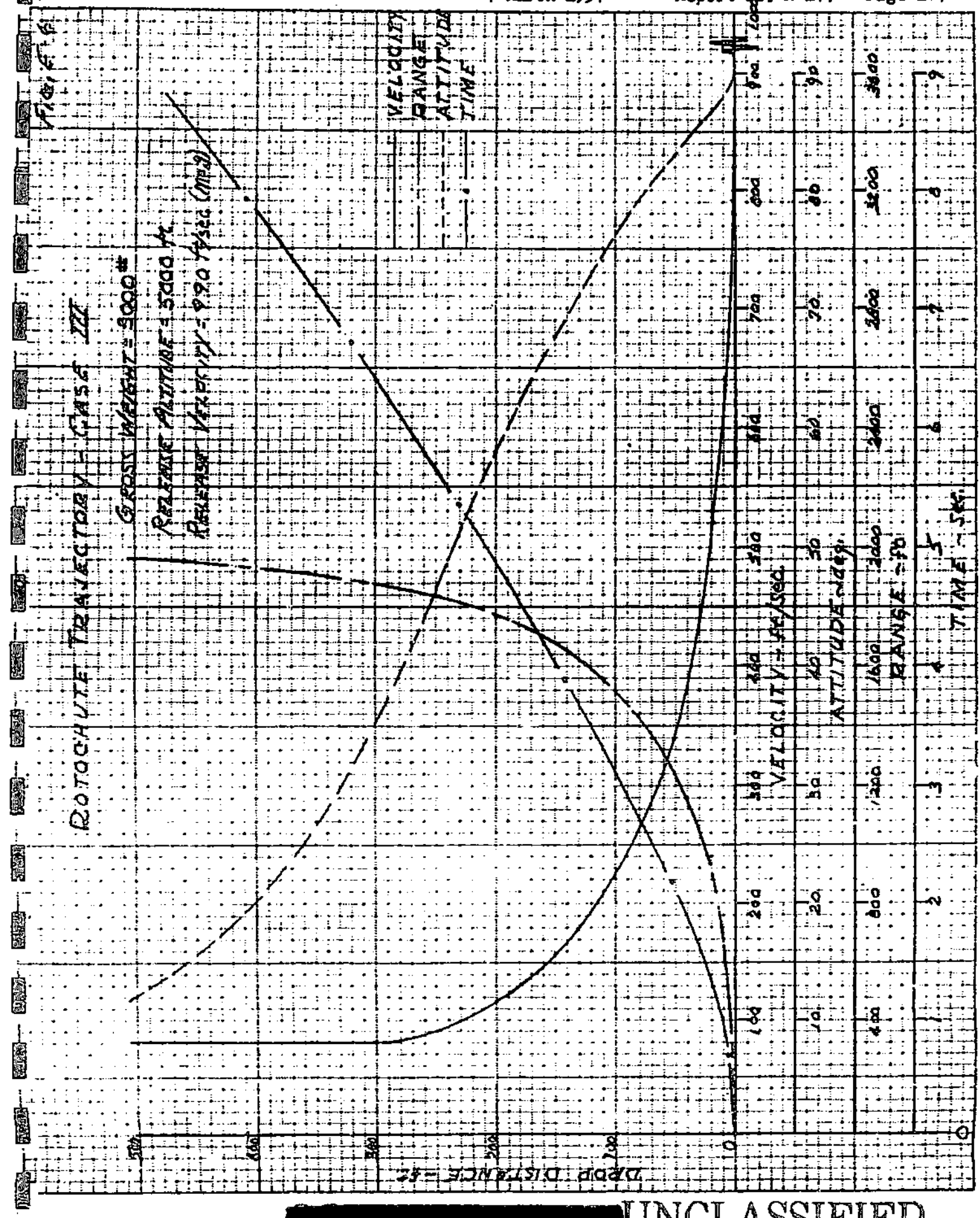
FIG. 61
ROTOCHUTE TRAJECTORY - CASE III
GROSS WEIGHT = 3000 #
RELEASE ALTITUDE = 3000 ft.
RELEASE VELOCITY = 990 ft/sec (MACH .9)
VELOCITY
RANGE
ATTITUDE
TIME
DROP DISTANCE - ft.
VELOCITY - ft/sec
ATTITUDE - deg.
RANGE - ft.
TIME - sec.

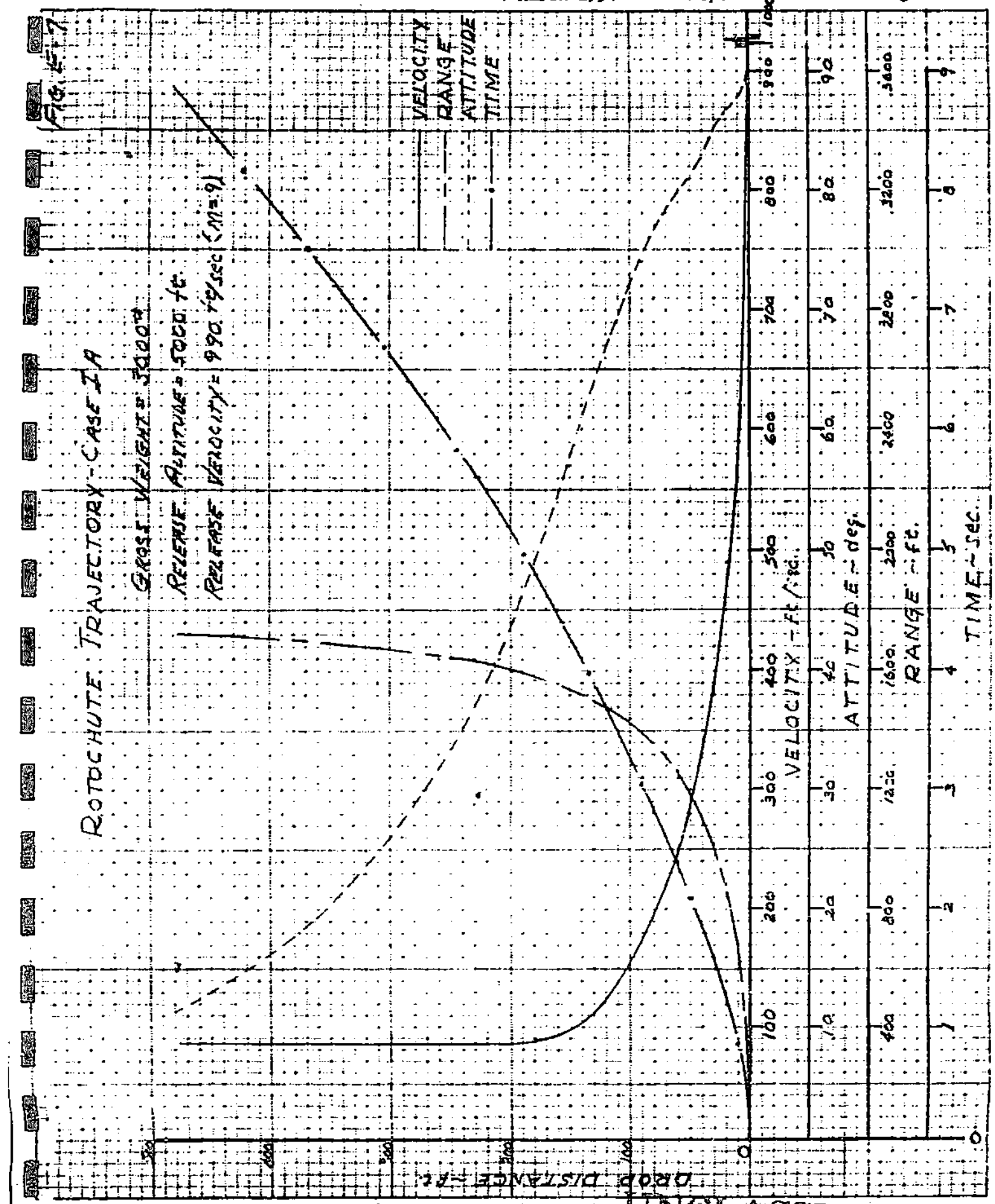
FIG. E-7
ROTOCHUTE TRAJECTORY - CASE IA
GROSS WEIGHT = 3200#
RELEASE ALTITUDE = 5000 ft.
RELEASE VELOCITY = 990 ft/sec (M=.91)
VELOCITY
RANGE
ATTITUDE
TIME
VELOCITY ~ ft/sec.
ATTITUDE ~ deg.
RANGE ~ ft.
TIME ~ sec.
DROP DISTANCE ~ ft.

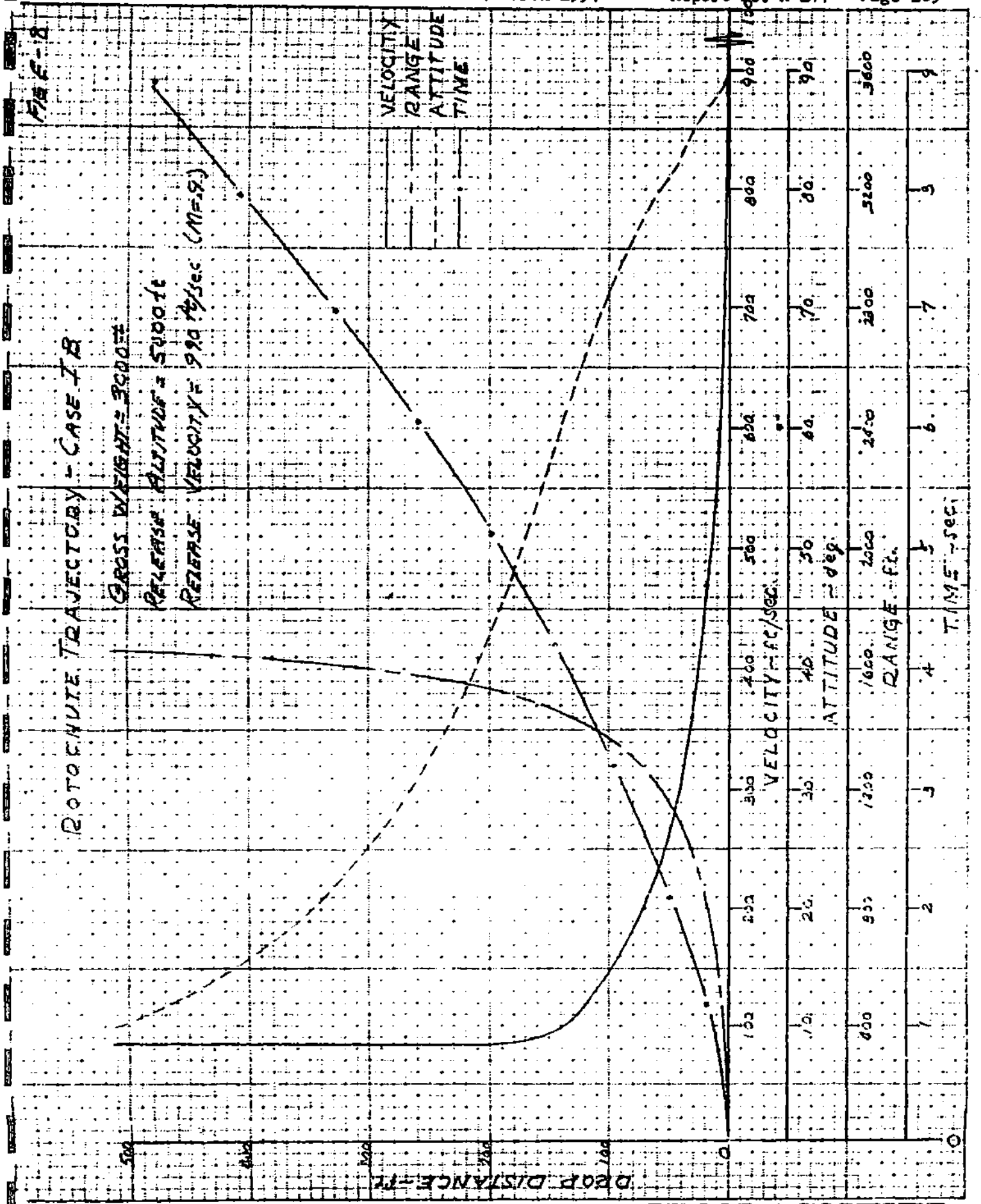
FIG E-18
ROTOBUNTE TRAJECTORY - CASE 7B
GROSS WEIGHT = 3000#
RELEASE ALTITUDE = 5000 ft
RELEASE VELOCITY = 990 ft/sec (M=.9)
VELOCITY
RANGE
ATTITUDE
TIME
VELOCITY - ft/sec
ATTITUDE - deg
RANGE - ft.
TIME - sec
DROP DISTANCE - ft

VARIATION OF ROTOCHUTE ATTITUDE ANGLE AND DROP DISTANCE FROM RELEASE ALTITUDE WITH DESIGN LIMIT TIP SPEED

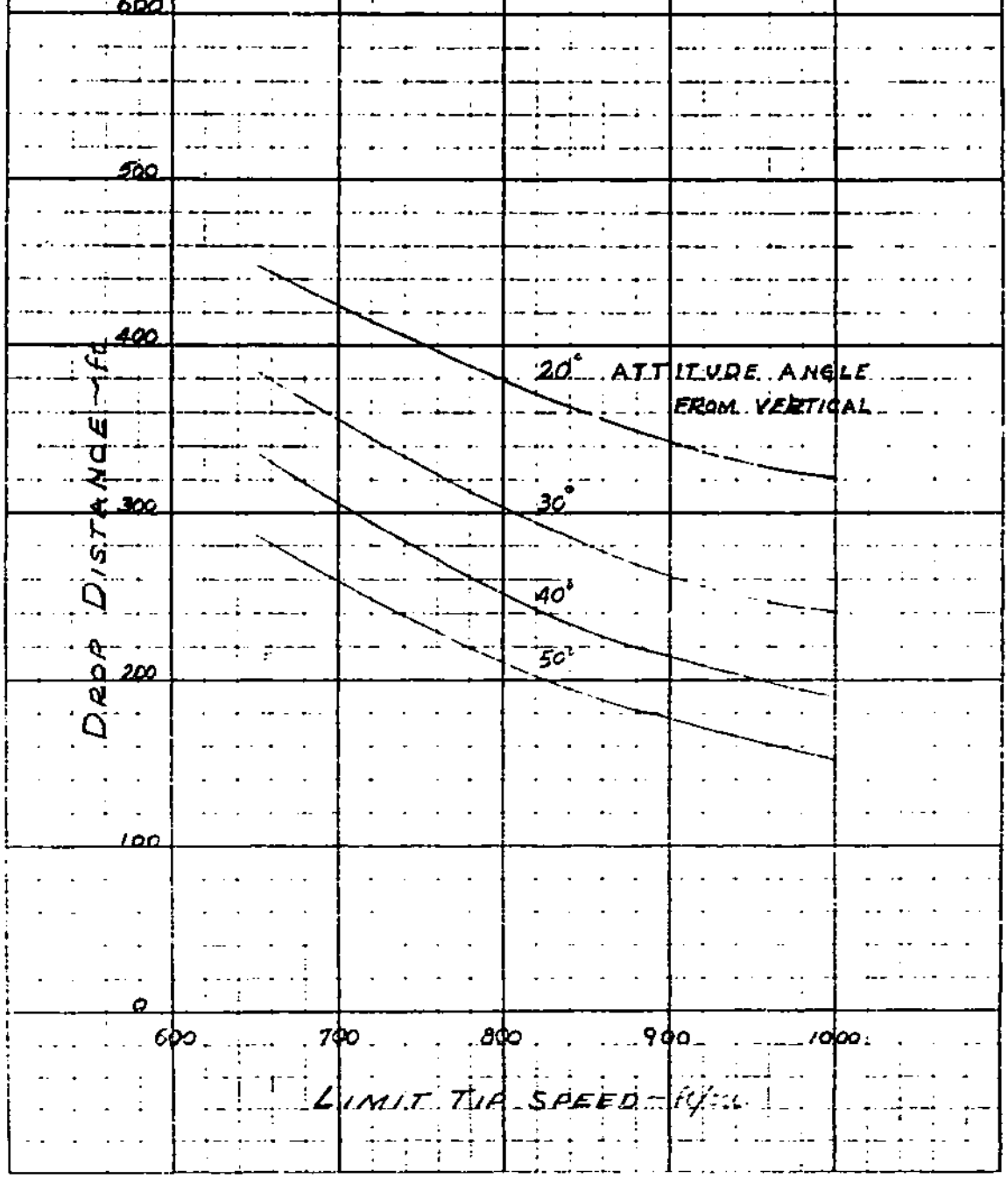

MODEL
REPORT

UNCLASSIFIED

DATE 7 March 1957
PAGE 1/1
FIGURE E-10

PROTOTYPE ROTOCHUTE GROSS WEIGHT VARIATION WITH DESIGN LIMIT TIP SPEED

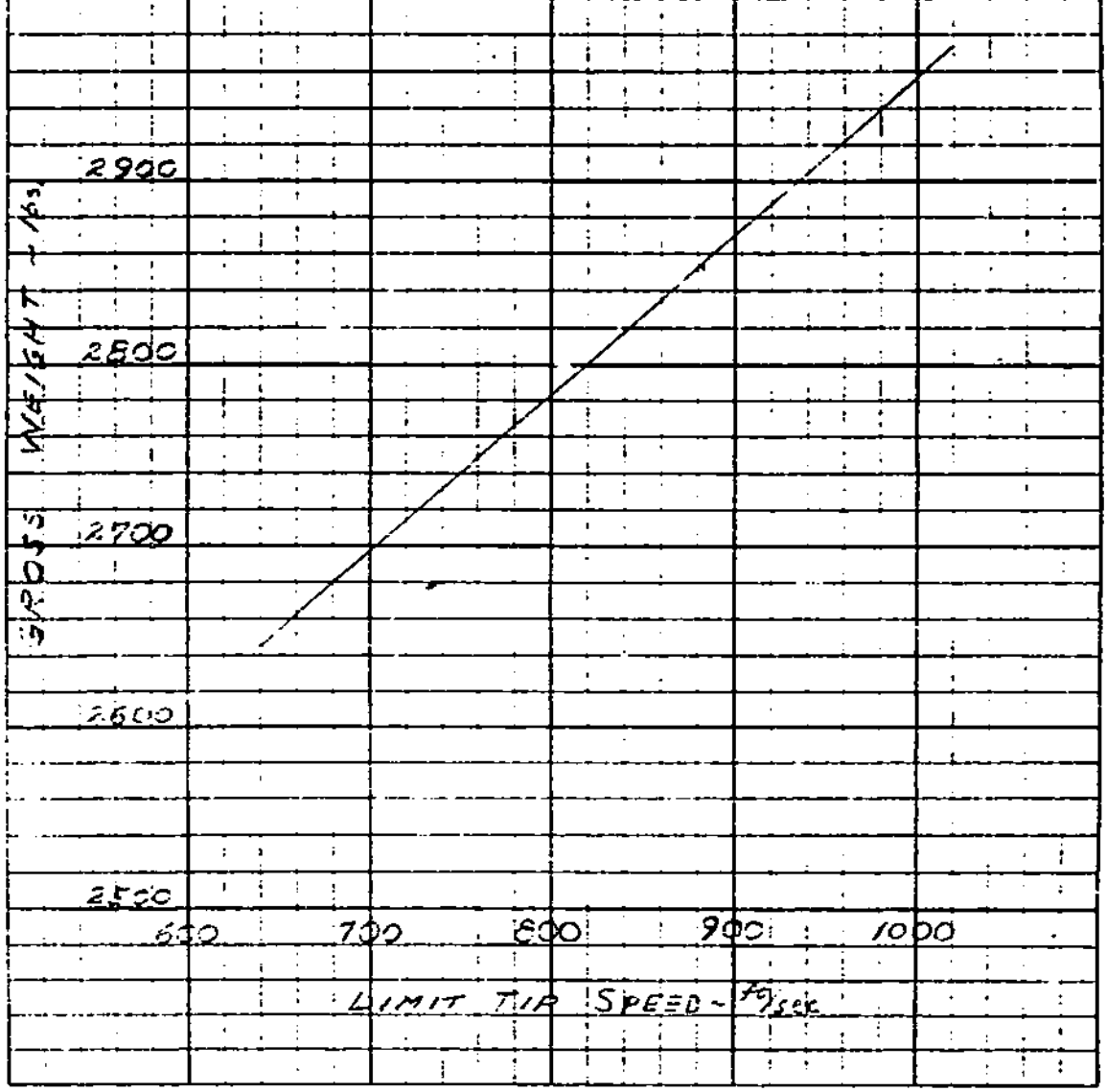


UNCLASSIFIED

[redacted]

EXAMPLE OF STABILITY RESULTS
DETERMINED BY ELECTRICAL ANALOGY



Page 566

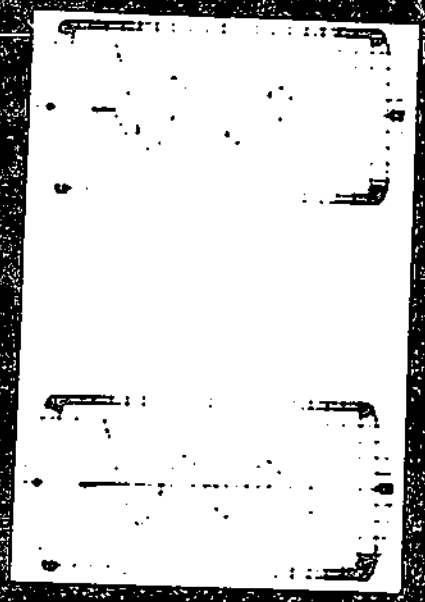

$\alpha_x$ & $\alpha_y$

$\alpha_x$

$k = 2$

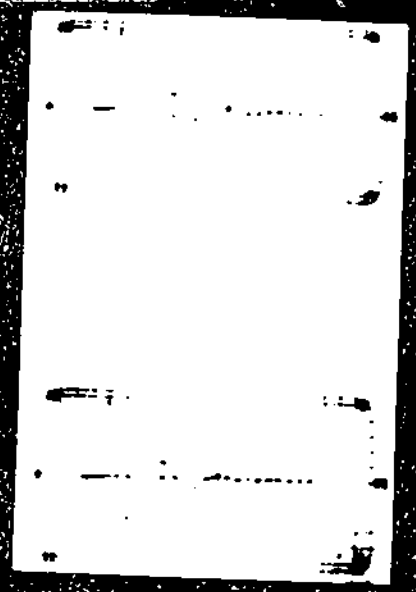

$k = 6$

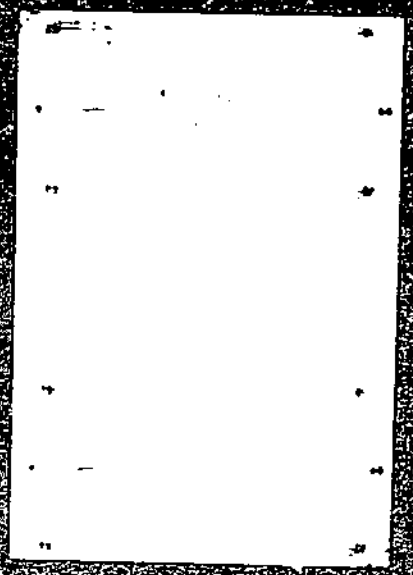

$\alpha_x$ & $\alpha_y$

$\alpha_x$

$k = 4$

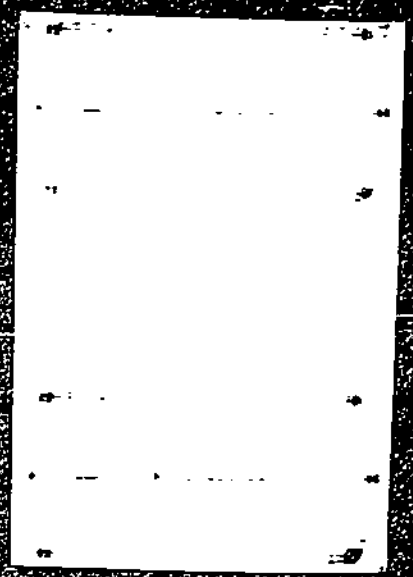

$k = 8$

FIG. F-2

SPIRAL OSCILLATION DAMPING

UNCLASSIFIED

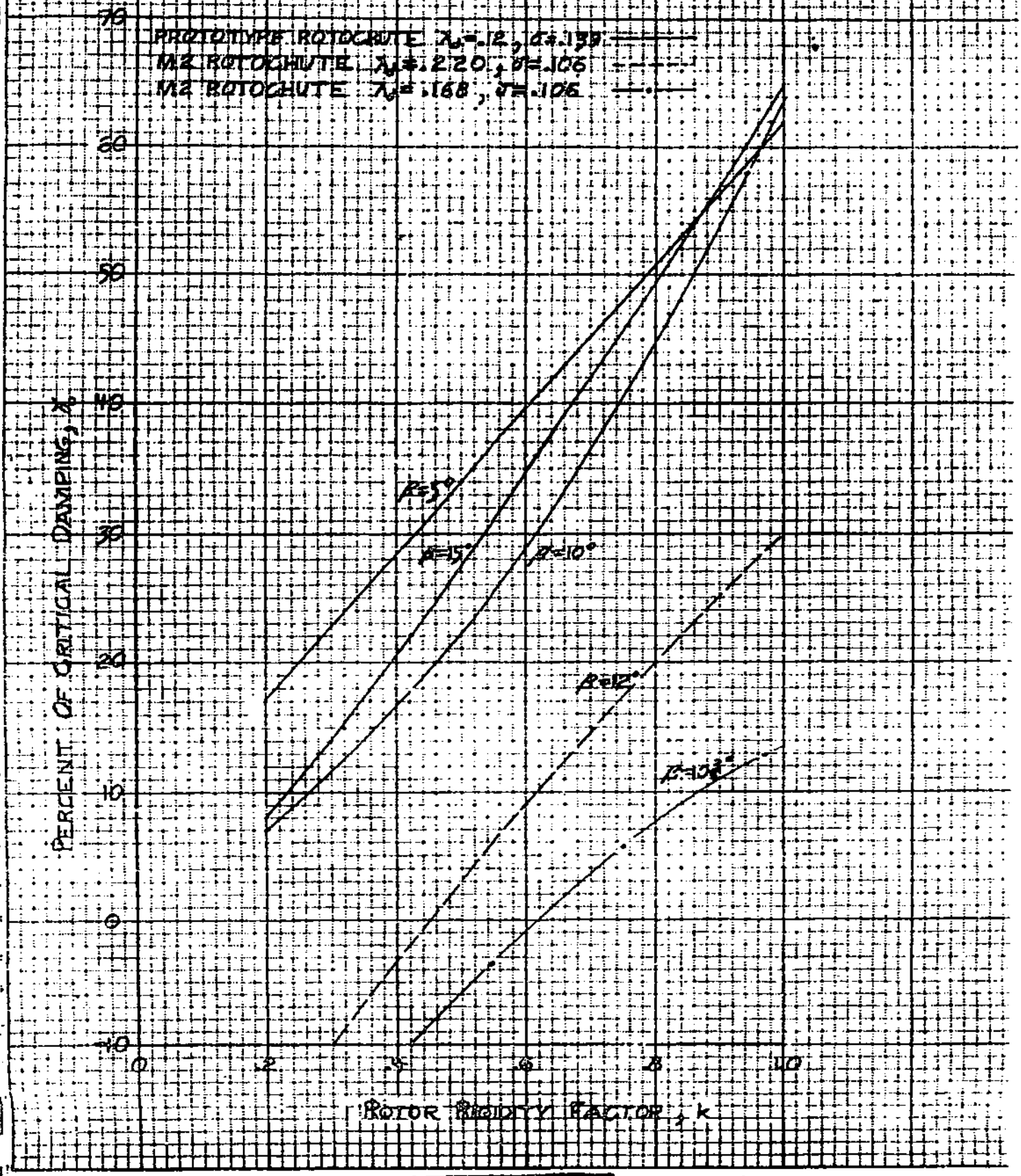


[redacted] UNCLASSIFIED

000568

FIG. F-3

UNCLASSIFIED

INFLUENCE OF ROTOR INERTIA ON SPIRAL OSCILLATION DAMPING

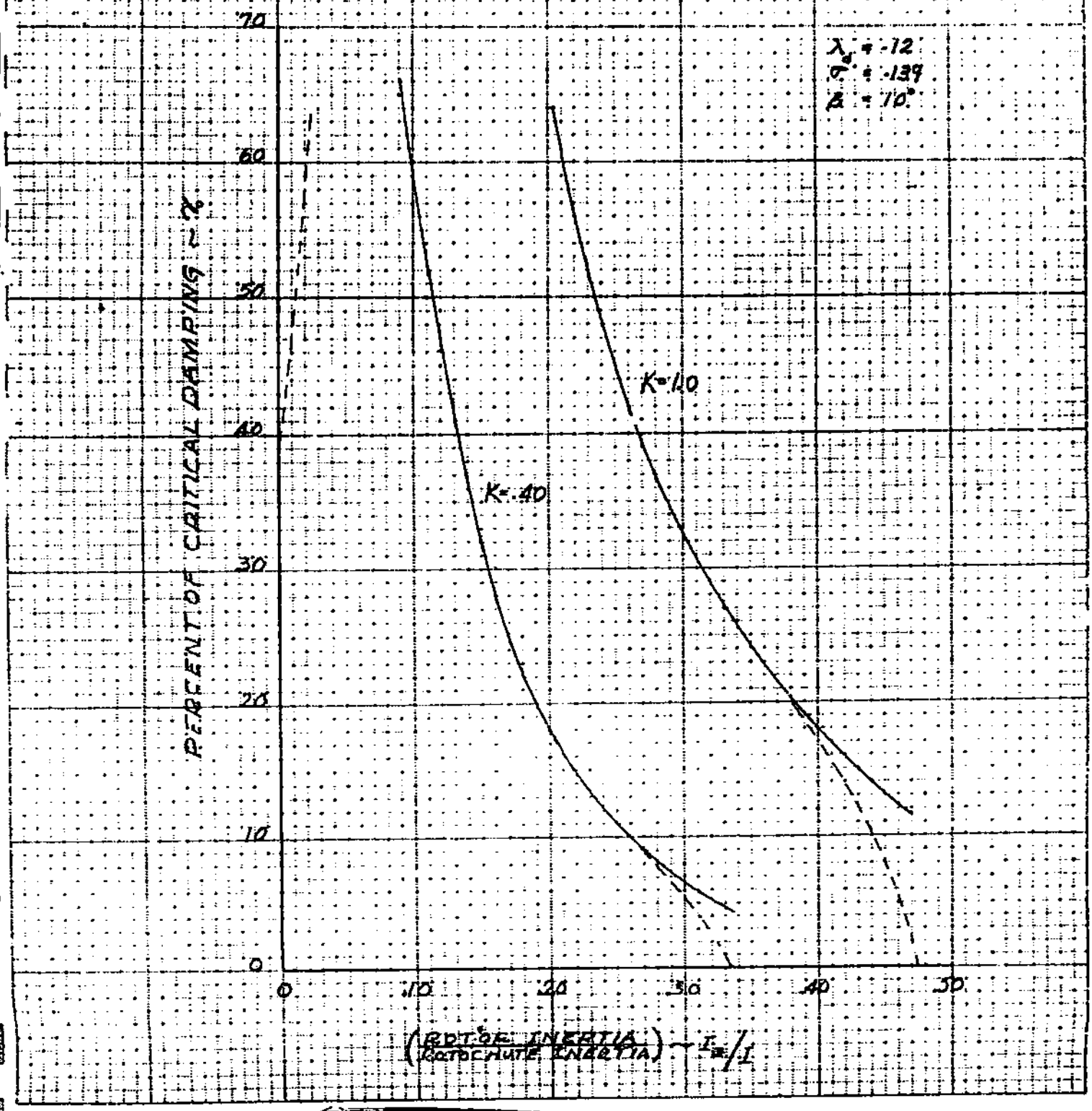


[redacted] UNCLASSIFIED

FIG. F+43

INFLUENCE OF SPECIFIC DERIVATIVES ON SPIRAL OSCILLATION DAMPING

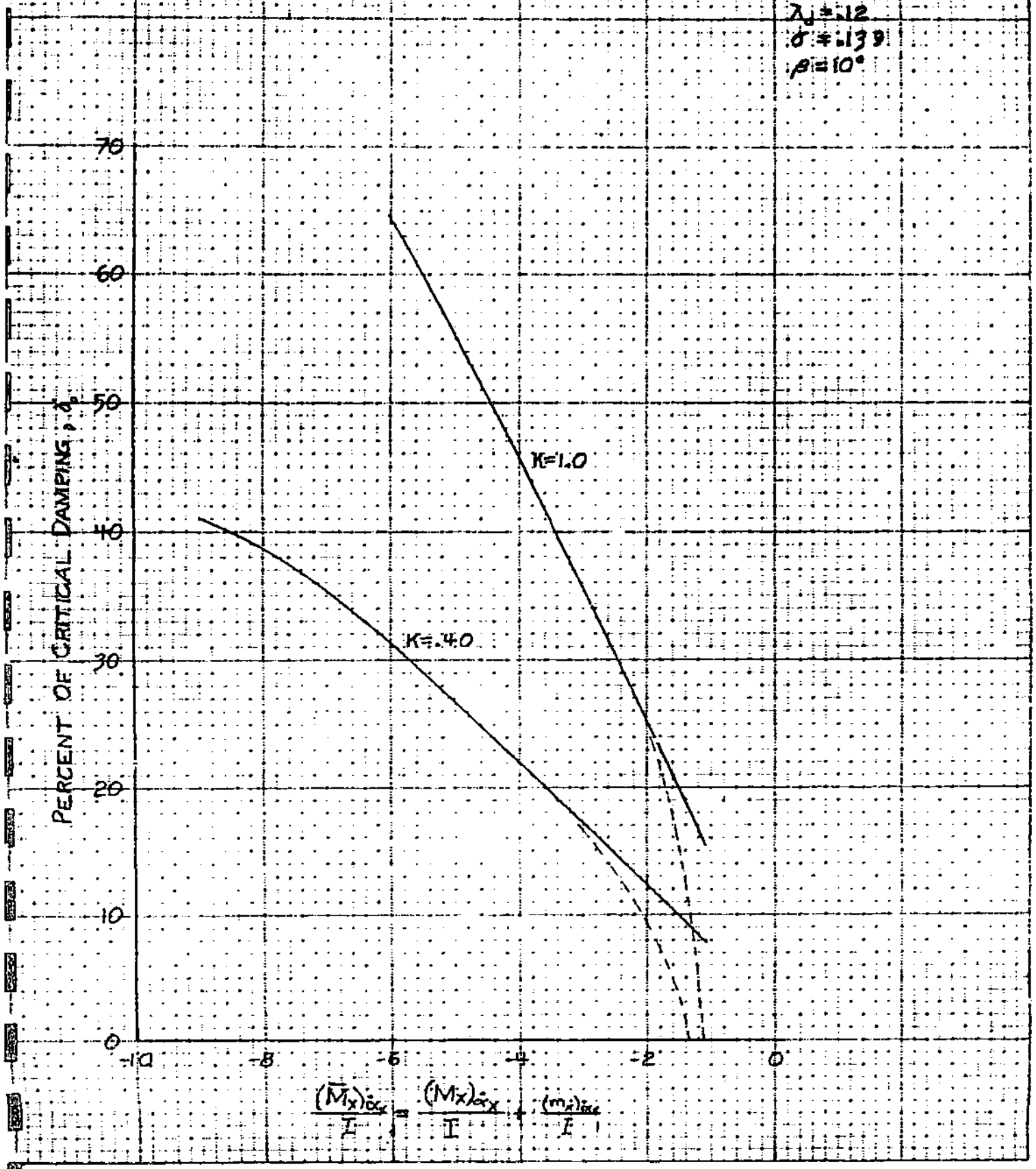

UNCLASSIFIED

Fig. F-46

INFLUENCE OF SPECIFIC DERIVATIVES ON SPIRAL OSCILLATION DAMPING

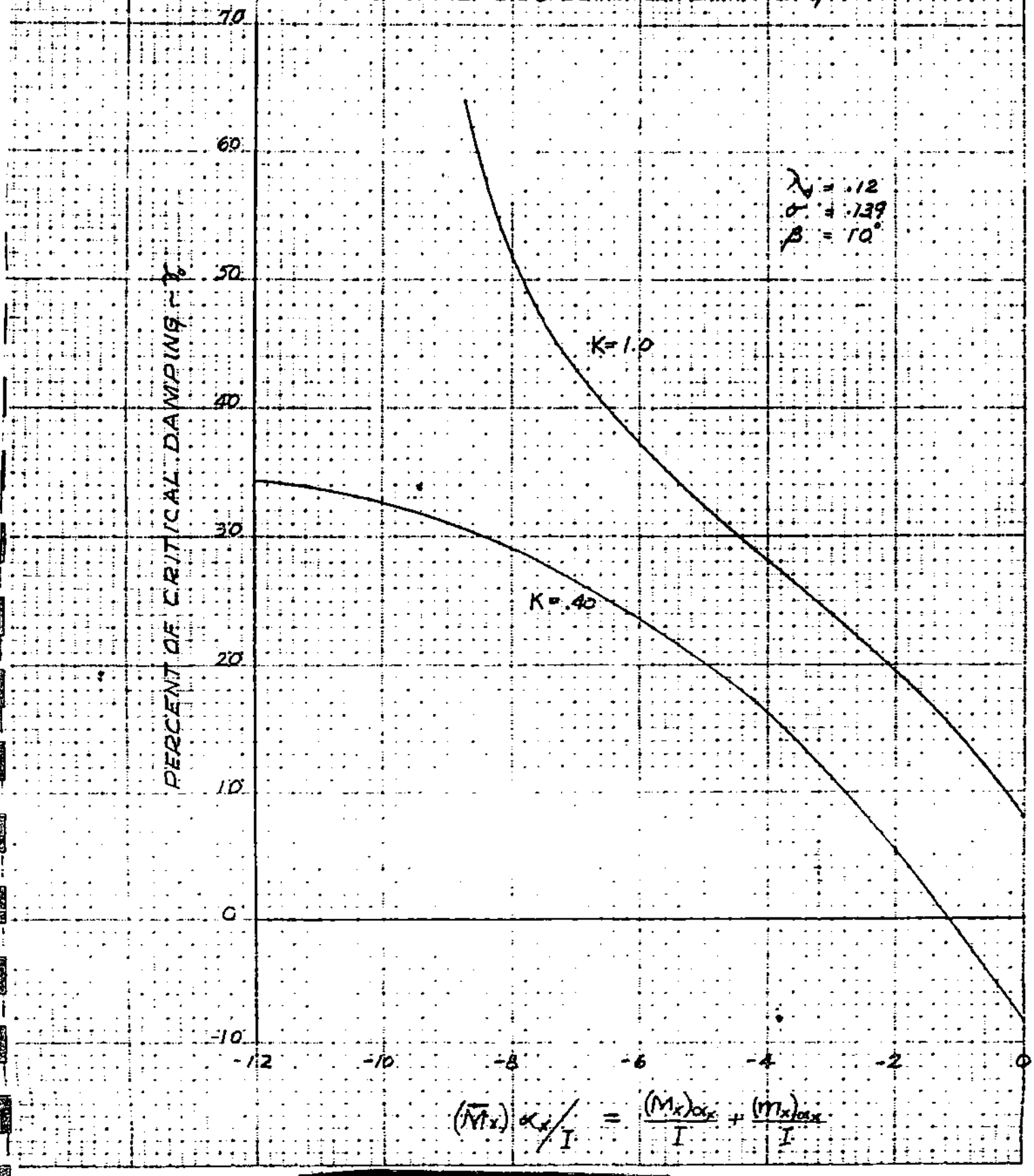


[redacted]

UNCLASSIFIED

Fig. F-4c

INFLUENCE OF SPECIFIC DERIVATIVES ON SPIRAL OSCILLATION DAMPING

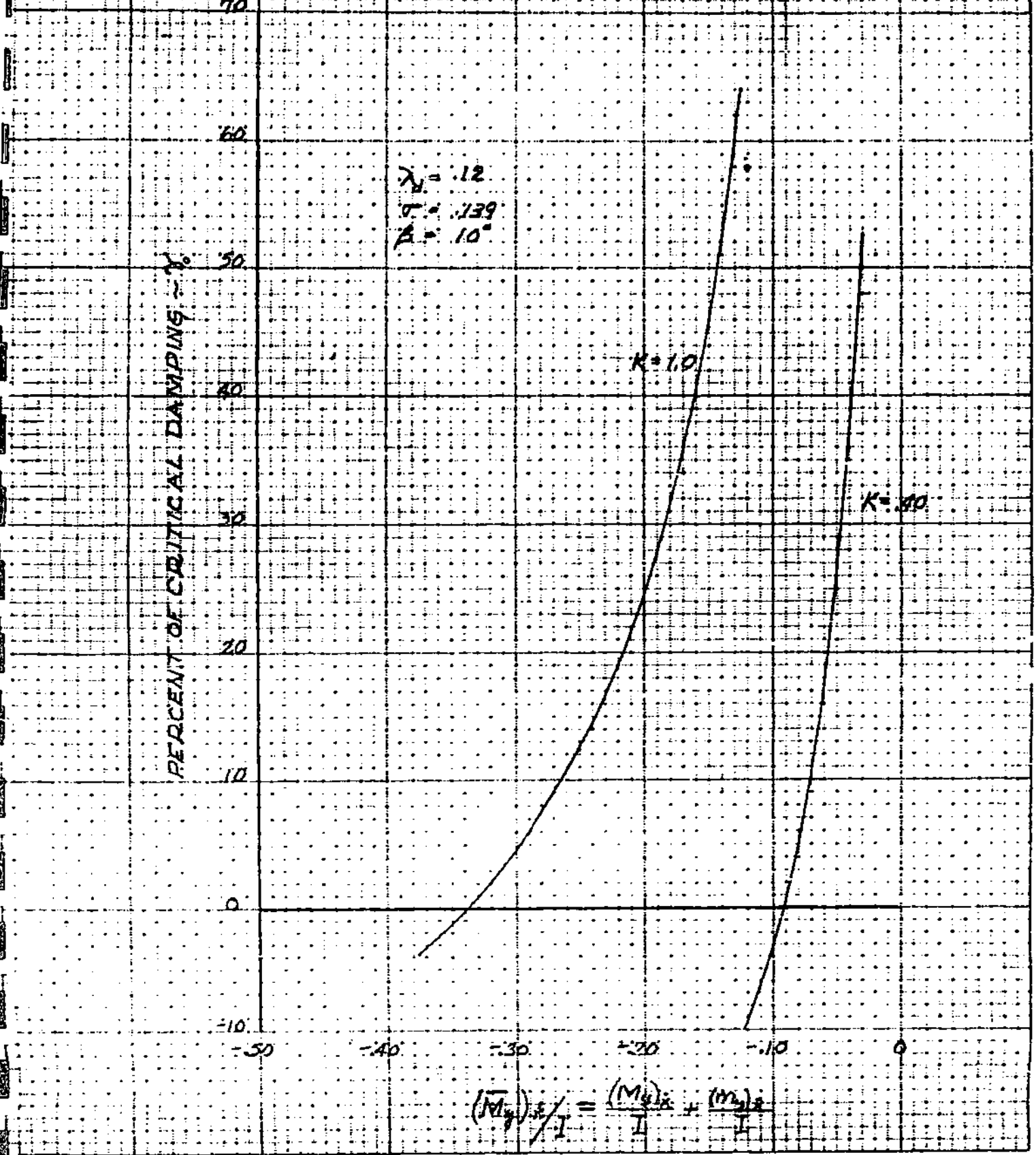

FIG. F-4d

INFLUENCE OF SPECIFIC DERIVATIVES ON SPIRAL OSCILLATION DAMPING

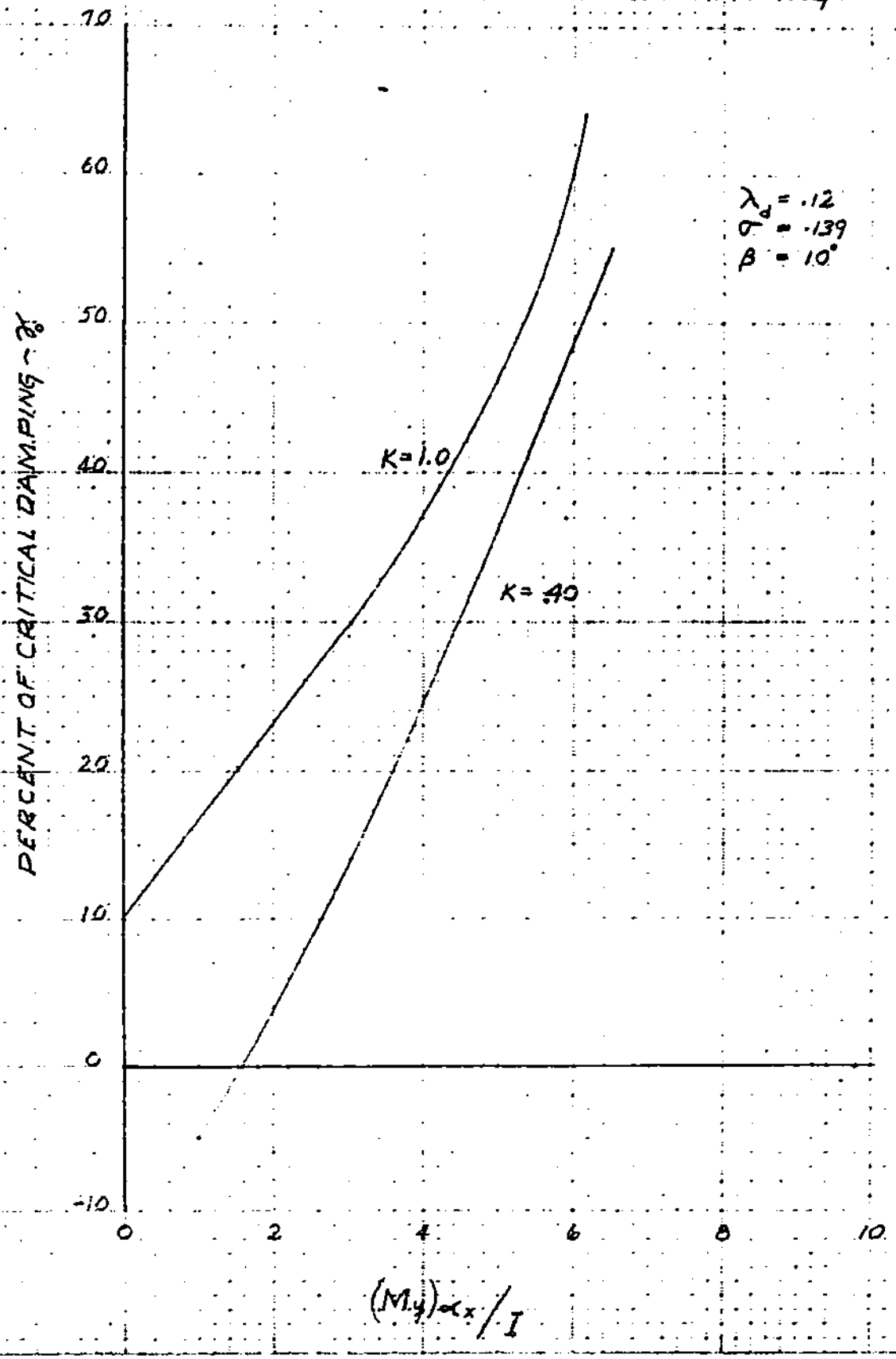

FIG. F-42

INFLUENCE OF SPECIFIC DERIVATIVES ON SPIRAL OSCILLATION DAMPING

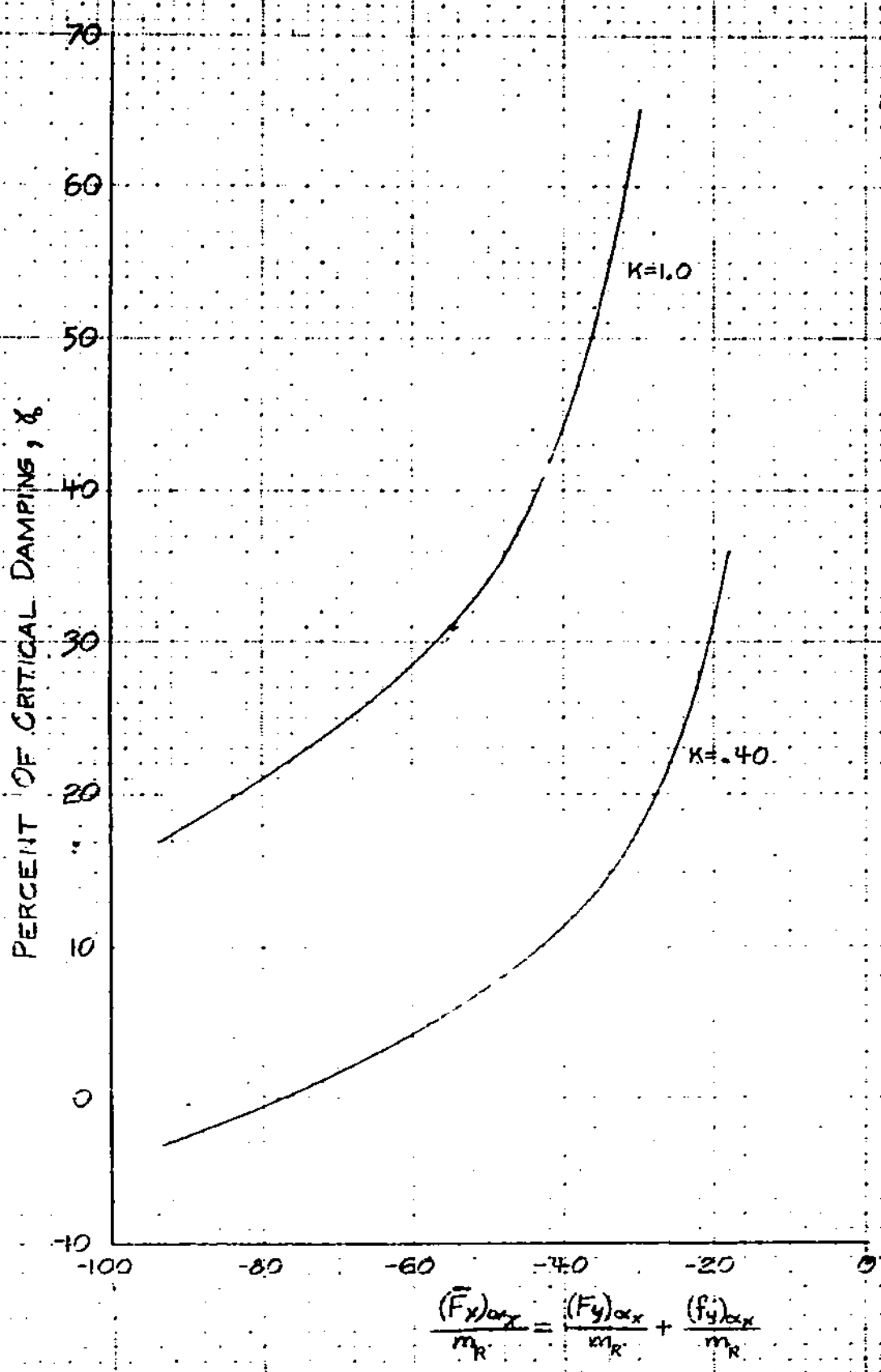

FIG. F-5

SPIRAL OSCILLATION PERIOD

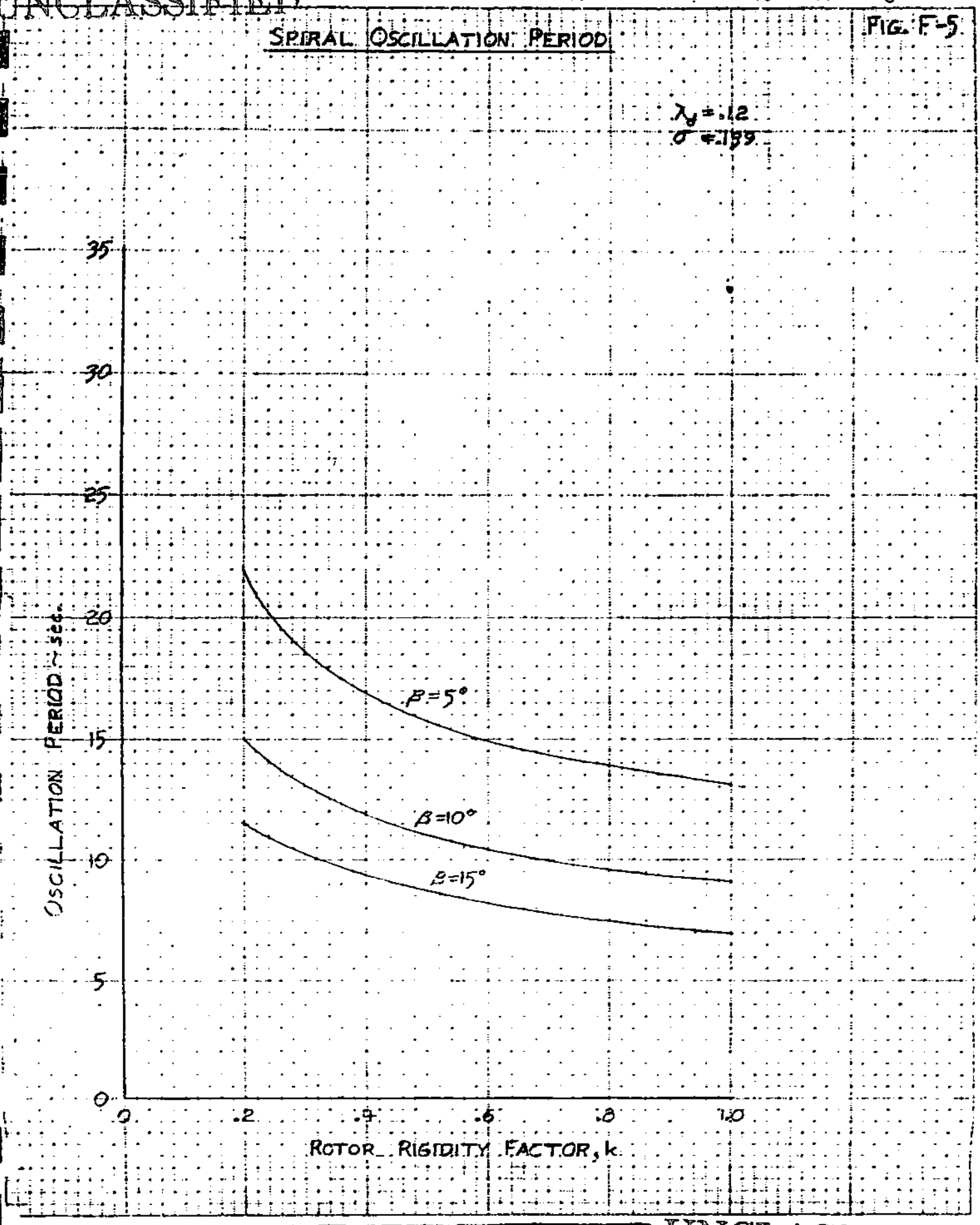

UNCLASSIFIED

FIG. F-6

INFLUENCE OF ROTOR SPEED ON ROTOR RIGIDITY FACTOR

PROTOTYPE ROTOCHUTE; $\gamma = 5.76$, $\beta = 0°$

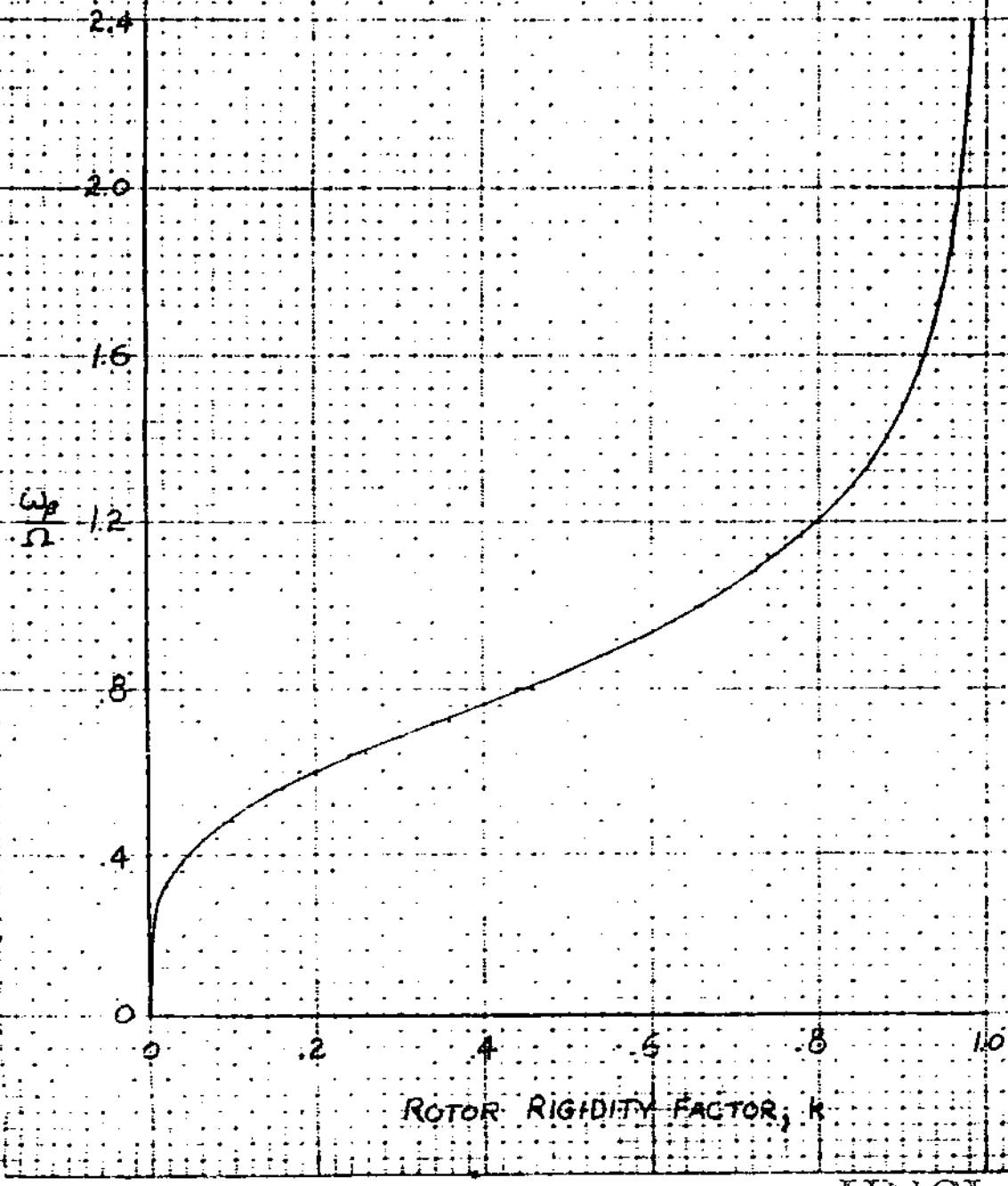


[redacted] UNCLASSIFIED

[redacted]

DATE: 7 March 1957
Report No. R-177
Page No. 182

Figure G-1

SCHEMATIC DIAGRAM OF WIND TUNNEL MODEL INSTALLATION

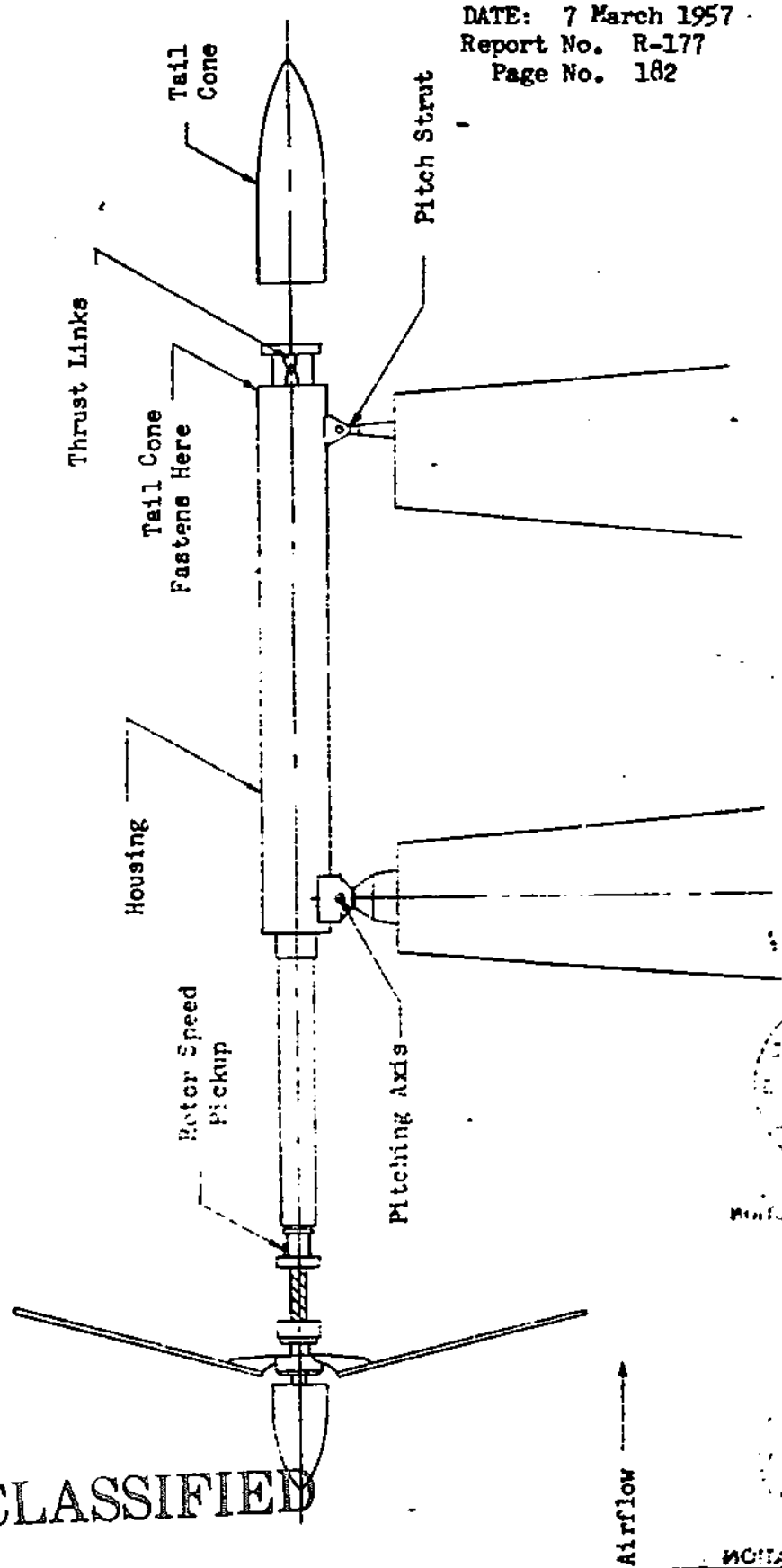


UNCLASSIFIED

[redacted]

SINGER CORPORATION
CENTRAL FILE & RECORDS
RECEIVED